Efficient Algorithms for Light Transmission, Focusing and Scattering Matrix Retrieval in Highly Diffusive 3D Random Media

by

Han Guo

A dissertation submitted in partial fulfillment
of the requirements for the degree of
Doctor of Philosophy
(Electrical Engineering)
in the University of Michigan
2018

Doctoral Committee:

Professor Eric Michielssen, Co-Chair
Associate Professor Raj Rao Nadakuditi, Co-Chair
Professor Anthony Grbic
Professor John Carl Schotland

*The birth place of
this work*

Han Guo

hanguo@umich.edu

ORCID iD: 0000-0002-7206-8528

This Work is Dedicated
To
My Family and All My Friends

TABLE OF CONTENTS

LIST OF FIGURES

ix

LIST OF TABLES

LIST OF ALGORITHMS

ABSTRACT

Wavefront shaping provides an increasingly appealing avenue for imaging and other applications that require controlling electromagnetic waves passing through complex and disordered media. Indeed, these techniques allow researchers and engineers to exploit the properties of high-frequency waves, particularly optical ones, as they interact with these media to obtain nearly perfect transmission and a high degree of focusing. Here, we simulate the process of wave propagation in 3D random media using full-wave, integral equation-based computational electromagnetics schemes. We replicate many experimental observations relating to the existence of so-called open channels in non-absorbing random media and the distribution of their transmission coefficients. In addition, we develop new schemes for manipulating these waves, e.g. by focusing them onto one or multiple spots in the output plane. Furthermore, we leverage the computational methods to develop new schemes for characterizing random media, e.g. by computing their scattering and transmission matrices under a variety of conditions. Finally, we study the transmission properties of absorbing media and find a universal fluctuant pattern of their maximal transmission coefficients.

CHAPTER 1

Introduction

The analysis of wave propagation and scattering in random media is important in many scientific and engineering applications. The stochastic spatial fluctuations of mass densities or dielectric permittivities in such media causes random changes in the propagation direction of an elastic or electromagnetic wave. From a macroscopic viewpoint, these changes result in a diffusive scattering phenomena. Scholars from disciplines ranging from theoretical physics and microphysics to applied electromagnetics, applied mathematics, statistics, telecommunication, optics, acoustics, and bioengineering, all have attempted to discover and characterize the mechanisms that govern diffusive scattering phenomena. These efforts have targeted various engineering applications, including remote sensing, ultrasound, microwave imaging, non-invasive inspection, electromagnetic hyperthermia treatment, and ultrasonic lithotripsy. From a theoretical perspective, these studies have sought to describe the scattering problem using multiple scattering, radiative transfer, and mesoscopic transport theories, using methods and algorithms such as wavefront shaping, time-reversal, and phase-conjugation.

In this chapter, we first present a brief overview of studies addressing the problem of wave propagation and scattering in random media before reviewing the relevant work serving as the research foundation for this dissertation. We then state the research questions underlying this dissertation, intending to address and elucidate the novelty of this work.

1.1 Background

The propagation of waves is described by the wave equation, a hyperbolic partial differential equation given by

$$\nabla^2 \Psi(\boldsymbol{r}, t) - \frac{n^2(\boldsymbol{r})}{c^2} \frac{\partial^2 \Psi(\boldsymbol{r}, t)}{\partial t^2} = 0, \tag{1.1}$$

In this equation, t is the time variable, $\boldsymbol{r}$ is the spatial variable, and $\Psi(\boldsymbol{r}, t)$ denotes a wave varying in space and time. The wave can represent, for instance, a component of the electric field or light in electromagnetics or optics or, the longitudinal pressure of a sound wave in acoustics. c is a constant, representing the speed of the wave propagating. $n(\boldsymbol{r})$ is the refraction index which may vary as a function of space. Scattering is caused by the local variation of $n(\boldsymbol{r})$, which results from the presence of localized non-uniformities or scatterers that have a different mass density or permittivity than the background medium. In the current research, we focus on light propagation and scattering.

1.1.1 Single and Multiple Scattering Theory

The formal and systematic study of scattering in random media began at least fifty years ago. Initial studies tackled the problem based on the well-studied characteristics of scattering from a single object. This early research was based on two assumptions: scatterers are very dispersed in space, and scattering processes can be decomposed into many single scattering events, with each resulting from one of the scatterers [3–6]. This model was used for weather radar and ocean acoustic applications, but lacked precision. If the distribution of the scatterers favors a greater probability of multiple scattering events, it becomes necessary to include additional first- or second-order multiple scattering mechanics in the model [7]. A more rigorous model called multiple scattering theory (MST) therefore was proposed further developed as the underpinning of many engineering applications. This

model is rooted in the fundamental differential equations that govern the scattering phenomena, such as scalar wave equations or vector Maxwell's equations. It governs wavefield quantities, introduces the interaction of many scatterers, and then extracts statistical descriptor of the scattering phenomenon under [7, 8]. Prior to the 1950s, MST originated in the work of Ryde [9, 10], Foldy [11], Lax [12, 13], and Snyder [14]. Later, researchers including Twersky [15–17], Waterman [18], Ishimaru [7, 8, 19] and Beard [20] extended thid work. In this line of work, the diagram method has emerged as particularly helpful for representing multiple scattering processes [21–23]. The mathematical representation of scattering phenomena in MST is precise and complete; nonetheless, to obtain useful results, it is often necessary to use approximations, such as that proposed by Born [24].

1.1.2 Radiative Transport Theory

Radiative transport (RT) theory [25–27] provides a competing approach to describ scattering in random media. Unlike MST, RT does not focus on the underlying physical processes governed by the wave equation or Maxwell's equation, but directly describes the transport of energy passing through a medium with randomly distributed scatterers. Although RT is a heuristic theory and lacks the mathematical rigor of MST, it is more efficient for practical usage. The fundamental differential equation of RT is the radiative transfer equation, which is equivalent to the Boltzmann equation. Schuster [28] initially proposed RT to describe light propagation in a foggy atmosphere; later, RT was used extensively in astrophysics [25] as well as in microwave and millimeter-wave remote sensing applications [29–32].

1.1.3 Mesoscopic Transport Theory

To describe random scattering phenomena, the optics community received inspiration from the field of mesoscopic physics [33]. Mesoscopic physics study the interaction of many microscopic particles with a background medium characterized by an intermedi-

ate scale. This scale is much larger than the microscopic scale involving a few atoms or molecules, but smaller than the macroscopic scale where the principles of statistical mechanics apply. Within this context, a system (medium) has a countable and finite number of degrees of freedom for incoming and outgoing light modes, which are plane waves or linear combinations thereof. The number of degrees of freedom is limited by the maximum numerical aperture and the diffraction limit [34]. For example, an optics system with surface area A allows $N_s = 2A/\lambda^2$ independent incident modes for light of wavelength λ [35]. In terms of light transmission, an important concept developed by the mesoscopic transport theory [33] is the notion of open and closed transport channels, or transport modes. These channels (modes) represent a linear combination of the independent incident modes, as specified by a particular medium's configuration. For a non-absorbing system, the open channels allow for transmitted diffusive waves with almost no back reflection; closed channels, in contrast, do not allow for transmission. In fact, there are finite independent transport modes, and any transport mode is a linear combination of the independent ones. The transmission characteristics of a medium can be described by the transmission matrix T with entries T_{ij} representing the transmission from incoming channel j to an outgoing channel i. Random matrix theory [33, 36, 37] provides a fundamental observation regarding the singular values of transmission matrices representing random meida: the singular values of eigen-channels of the transmission matrix are not uniformly distributed, but consist of many closed channels with almost zero transmission as well as a few open channels with full transmission. Dorokhov [38], Pendry [39, 40], Mello [41] and Beenakker [33] have pointed out that the transmission wave through a random medium results from a few open transmission channels [35].

Using a wavefront shaping technique, Vellekoop [42,43] directly validated the existence of these open channels in several physical experiments. This pioneering work sparked studies to overcome the limitation of light transmission through opaque media by taking advantage of the open channels via the wavefront shaping technique. Popoff [44], Kohlgraf [45],

Shi [46] and Kim [47] compared the theoretical prediction with the transmission coefficient distribution of the transmission matrix. Then, van Putten [48], Aulbach [49], Cui [50, 51], and Stockbridge [52] developed rapid experimental methods for wavefront-shaping-based focusing. More recently, Choi [53] and Jin [54, 55] investigated the properties of the eigen-wavefronts through numerical simulations. These investigations paved the way for optical imaging and related applications through highly diffusive random media.

1.2   Recent Advances in Wavefront Shaping Technology

In principle, most optical engineering applications (e.g., imaging and focusing) exploit the inference of EM waves propagating in different directions with particular amplitudes and phases. Therefore, one must control the amplitudes and phases of these waves as the primary method for making optical devices function as desired. Wavefront modulators specifically are used to modulate EM waves by manupulating the wave's amplitude and phase. One representative type of wavefront modulator is the spatial light modulators (SLMs). Astronomers early on used SLMs developed to compensate for the optical aberration caused by light passing through the atmosphere. These SLMs were cumbersome, expensive, and low-resolution, which limited their application in other domains. Today's state-of-the-art SLMs use liquid crystals on silicon to modulate the amplitude and phase of EM waves through controlling the alignment of the liquid crystal molecules, thus achieving high-pixel resolution on a small scale while remaining relatively cheap [56]. Other modern wavefront modulators include digital micro-mirror devices (DMDs) and deformable mirrors (DMs). Using such SLMs, Vellekoop and Mosks [42, 43] pioneering experiments in 2007 opened the door for new approaches to control the light passing through thick opaque scattering materials beyond the depth reachable by ballistic light. Later, Conkey et al. used a DMD to precisely control the optical phase for focusing in a temporally dynamic scattering medium [57]. For their part, Van Putten et al. [58] and Park et al. [59] utilized

commercial twisted nematic liquid-crystal displays (LCDs) to modulate both the amplitude and phase of the optical field. The rapid development of fast and accurate lights / EM waves modulating technology is the major driving force for many wavefront-shaping-related applications.

1.3 Advances Proposed by This Work

Many researchers have sought to reveal the characteristics of eigen-wavefronts and to develop efficient methods for controlling waves in random media. That said, mumerous phenomena remain poorly understood, including the following:

- The possibility of multi-foci focusing propagation through random media. A variety of studies have demonstrated the ability to focus on a single spot after propagating through random media, indicating that highly-transmitted wavefronts carried by open channels can constructively interference upon exiting the media. To what extent can constructive interference lead to multiple well-separated foci?

- Measuring the transmission matrix via backscatter analysis. Most applications, such as focusing, require knowledge of the transmission matrix. Current techniques for characherizing the transmission matrix often necessitate the use of a probe in the medium, the use of a second external detector (e.g., ultrasound transducer), or the embedding of active sources (e.g., fluorescent microspheres) to provide the necessary feedback. These approaches are invasive and/or inconvenient for many applications, such as *in vivo* biological experiments or medical diagnostics tests. Is it possible to measure the transmission matrix by examining only the backscattered wavefront from any particular incident wavefront? If so, this would be a tremendous advantage over existing techniques, allowing greater versatility in use of the wavefront shaping technique.

- Eigen-wavefronts in absorbing media. Most previous studies have investigated the open channels and eigen-wavefronts of non-absorbing media, particularly because in such media these channels always exist irrespective their depth. However, in absorbing media, light will inevitably decay due to dissipation by lossy scatterers and/or the background medium. Consequently, in such media there exist completely open channel leading to full transmission. The transmission coefficients therefore have an upper limit, which is less than 1.0, and the maximum possible transmission coefficient negatively correlates with the absorptivity and depth of the medium. It is of great importance to understand the distribution of transmission coefficients of the absorbing medium, and to investigate the effectiveness of the wavefront optimization methods, originally designed for non-absorbing media, in absorbing ones.

This work makes the following primary contributions:

- A 3D method of moments technique is deployed to model EM wave propagation in random media composed of multi-layered periodic slabs containing metallic particles ranging from dipoles to crosses and beyond. Rigorous numerical simulations demonstrate that the distribution of the transmission coefficients of this model align with the theoretical prediction and physical experiments (Chapter 2 and Chapter 3).

- A new family of highly-efficient focusing schemes is proposed. These schemes can create multiple foci under a variety of conditions of practical interest. Our schemes apply to scenarios that allow for phase-only as well as full phase-amplitude modulation of the incident wavefront. In addition, they can be used to address problems requiring contrast and non-contrast as well as maximal-total-intensity and even-intensity (fair) focusing (Chapter 4).

- Novel approaches are proposed to retrieve the measurement matrix or the transmission matrix for a given random medium. These approaches rely on intensity-only measurements, or the assistance of passive "guide stars" (Chapter 5).

- A Fourier-transform and inverse-Fourier-transform-based scheme is proposed to focus temporal pulses passing through random media. (Chapter 6).

- An investigation was conducted into the characteristics of eigen-modes and the efficacy of backscattering-minimizing optimization methods for absorbing media. We found that the statistics for the maximum transmission coefficient for the absorbing medium follow a Tracy-Widom distribution (Chapter 7).

<div align="center">

CHAPTER 2

Numerical Modeling of 3D Random Media

</div>

2.1 Introduction

The computational study of light interaction with 3D random media requires so-called forward-modeling, viz., computational methods for simulating light propagation and diffusion or EM scattering within or through a known/deterministic realization of a random medium. Here, we extend the matrix methods developed for 2D random media in [54,55,60–62] to 3D. Our ultimate goal is to model the scattering properties of a medium by slicing it up into many layers and cascading scattering matrix of each layer. Unlike in 2D, each scattering matrix here is generated by using a full-wave numerical Maxwell's equation to analyze a periodic medium. Note that the use of the periodic boundary condition, somewhat unrealistic in the real world, is sufficient as far as our research is concerned: the numerical results of our modeling qualitatvely match the theoretical predictions of Dorokhov [38], Pendry [39, 40], Mello [41] and Beenakker [63], as well as the experimental validation from Vellekoop [42, 43] of eigen-wavefronts distributions in aperiodic random media.

The rest of this chapter is organized as follows. Section 2.2 introduces the representation of modes in 3D periodic media. Section 2.3 defines the scattering matrix, elucidates its important properties, and describes a scheme for cascading them. Section 2.4 summarizes our integral equation method for generating the scattering matrix. With this knowledge in

<div align="center">

9

</div>

hand, Section 2.5 presents our approach to constructing a random medium and its associated scattering matrix. Section 2.6 summarizes the contributions of the chapter.

2.2 Modes

2.2.1 Modes in 3D Periodic Media

Electromagnetic waves in 3D periodic media can be described in terms of a countable and finite set of wave solutions to Maxwells equations, called modes. We start with a plane wave solution to Maxwells equations

$$\boldsymbol{E}_l^{\pm}(\boldsymbol{r}, t) = \hat{\boldsymbol{p}}_l E_l^{\pm p} e^{j(\omega t - \boldsymbol{k}_l^{\pm} \cdot \boldsymbol{r})}, \tag{2.1}$$

Here $\boldsymbol{r}$ is the spatial coordinate in 3D, t is the time, and ω is the angular frequency. $\boldsymbol{k}_l^{\pm}$ is the l-th wavevector, the superscript $\pm$ denotes the relative propagating direction of the wave w.r.t. the normal to the random medium being considered, $+$ stands for forward traveling direction, and $-$ indicates backward traveling ones. $\hat{\boldsymbol{p}}$ denotes a unit vector indicating the polarization direction of the plane wave, and E_l^p represents the l-th modal coefficient of the $\hat{\boldsymbol{p}}$ polarized field component; it is a phasor specifying the plane wave's amplitude and phase. Using the above definition, the total electric field on $\boldsymbol{r}_0$ at t_0 in our system can be expressed as the superposition of plane waves as

$$\boldsymbol{E}(\boldsymbol{r}_0, t_0) = \sum_{l=1}^{N} \left(\boldsymbol{E}_l^+(\boldsymbol{r}_0, t_0) + (\boldsymbol{E}_l^-(\boldsymbol{r}_0, t_0) \right). \tag{2.2}$$

Here N is the dimension of the countable basis of plane waves in our system. Since we are dealing with time-harmonics excitations, i.e. monochromatic light, we drop the e^{jwt} factor

and recast Eq. (2.2) as

$$\boldsymbol{E}(\boldsymbol{r}_0) = \sum_{l=1}^{N} \left(\boldsymbol{E}_l^+(\boldsymbol{r}_0) + (\boldsymbol{E}_l^-(\boldsymbol{r}_0)) \right), \tag{2.3}$$

where

$$\boldsymbol{E}_l^{\pm}(\boldsymbol{r}) = \hat{\boldsymbol{p}}_l E_l^{\pm p} e^{-j\boldsymbol{k}_l^{\pm} \cdot \boldsymbol{r}}, \tag{2.4}$$

and $\|\boldsymbol{k}_l^{\pm}\|_2 = k = 2\pi/\lambda$ is the wavenumber of the single harmonic with wavelength λ.
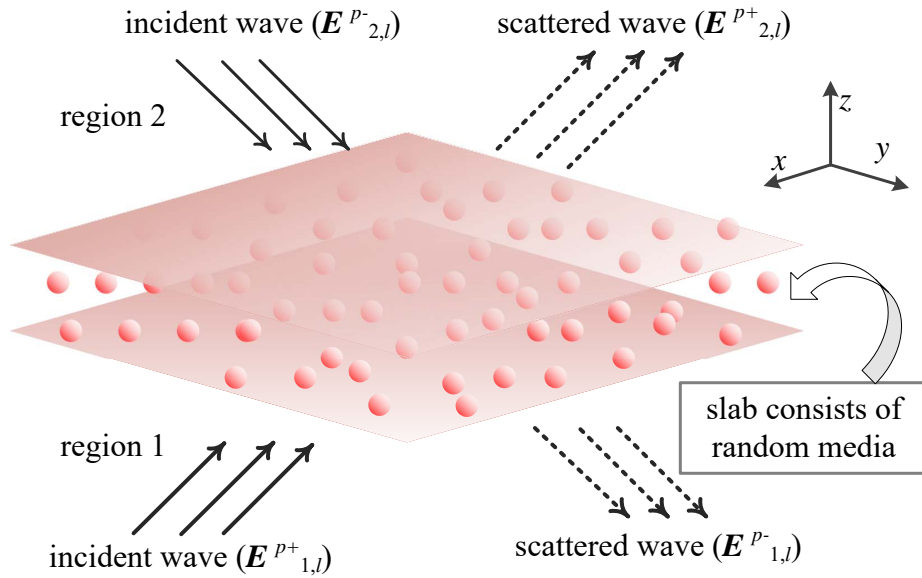
Figure 2.1: Typical scattering system involving 3D random media.

Figure 2.1 illustrates a typical scattering system of interest to us. In the Cartesian coordinate system, a slab of a random medium extends in the xy plane and divides the space into a lower region (Region 1) with z coordinate tending toward $-\infty$ and an upper region (Region 2) with the z coordinate tending toward $+\infty$. The incident waves can be presented in Region 1 as

$$\boldsymbol{E}_1^{inc}(\boldsymbol{r}) = \sum_{l=1}^{N} \boldsymbol{E}_{1,l}^+(\boldsymbol{r}), \tag{2.5}$$

and in Region 2 as

$$\boldsymbol{E}_2^{inc}(\boldsymbol{r}) = \sum_{l=1}^{N} \boldsymbol{E}_{2,l}^{-}(\boldsymbol{r}). \tag{2.6}$$

As before, the superscript $\pm$ denotes the specific wave propagating direction, towards to $+z$ or $-z$. The interation of the incident field with the slab generates scattered waves expressed as

$$\boldsymbol{E}_1^{scat}(\boldsymbol{r}) = \sum_{l=1}^{N} \boldsymbol{E}_{1,l}^{-}(\boldsymbol{r}), \tag{2.7}$$

and

$$\boldsymbol{E}_2^{scat}(\boldsymbol{r}) = \sum_{l=1}^{N} \boldsymbol{E}_{2,l}^{+}(\boldsymbol{r}). \tag{2.8}$$

Each field component $\boldsymbol{E}_{i,l}^{\pm}(\boldsymbol{r}), i = 1$ or $2, l = 1, \ldots, N$ is characterized by its wavevector $\boldsymbol{k}_l^{\pm} = (k_x^{(l)}, k_y^{(l)}, \pm k_z^{(l)})$, its complex amplitude $E_{i,l}^{\pm}$, and its polarization $\hat{\boldsymbol{p}}_l$. A plane wave's polarization direction is perpendicular to its propagating direction and the direction of its wavevector; generally speaking, it can be decomposed into two orthogonal components $\hat{\boldsymbol{v}}_l$ and $\hat{\boldsymbol{h}}_l$:

$$\hat{\boldsymbol{h}}_l = \hat{\boldsymbol{z}} \times \hat{\boldsymbol{k}}_l^{+}, \tag{2.9}$$

as

$$\hat{\boldsymbol{v}}_l = \hat{\boldsymbol{h}}_l \times \hat{\boldsymbol{k}}_l^{+}. \tag{2.10}$$

Thus, the l-th plane wave with arbitrary polarization can be expressed as

$$\boldsymbol{E}_l^{\pm}(\boldsymbol{r}) = \left(E_l^{\pm v}\hat{\boldsymbol{v}}_l + E_l^{\pm h}\hat{\boldsymbol{h}}_l\right)e^{-j\boldsymbol{k}_l^{\pm}\cdot\boldsymbol{r}}. \tag{2.11}$$

The $\hat{\boldsymbol{h}}$ polarization (h-pol) is usually called the horizontal polarization because $\hat{\boldsymbol{h}}$ does not contain a z-directional component, and the $\hat{\boldsymbol{v}}$-polarization (v-pol) is usually called the vertical polarization because it does not contain a ϕ-directional component in the cylindrical coordinate system.

12

2.2.2 Modes Under Periodic Boundary Conditions

The countable and finite planewave solutions $\{ \boldsymbol{E}_l^{\pm} \mid l = 1, \dots, N \}$ imply that the propagating directions of the planewaves are finitely discretized in 3D space. This trait is also the consequence of introducing the periodic boundary condition in our system. Specifically, we assume that random media have are periodic along both the x and y directions with periodicities D_x and D_y, respectively. Hence, the discretized propagating direction of the l-th planewave can be specified by its wavevector as

$$\boldsymbol{k}_l^{\pm} \leftrightarrow \boldsymbol{k}_{mn}^{\pm} = (k_{m,x}, \ k_{n,y}, \ \pm k_{mn,z}), \tag{2.12}$$

where

$$k_{m,x} = k_x^{(1)} + 2\pi m/D_x, \ \ k_{n,y} = k_y^{(1)} + 2\pi n/D_y, \tag{2.13}$$

in which m and n are integers and

$$k_{mn,z} = \sqrt{k^2 - k_{m,x}^2 - k_{n,y}^2}. \tag{2.14}$$

$k = 2\pi/\lambda$ is a constant if we stick to the single harmonic with wavelength λ. Conventionally , $(k_x^{(1)}, \ k_y^{(1)}, \ k_{00,z})$ defines the $(0,0)$-th mode of the wavevector in $_{mn}$ notation or the 1-st mode of that occurring in the $_l$ notation.

A propagating wave requires the $k_{mn,z}$ to be a real value. Therefore, the number of propagating modes is finite, and all the propagating modes can be represented by the unique (m, n) pairs in the set

$$U = \left\{ (m, n) \mid k_{m,x}^2 + k_{n,y}^2 < k^2 \right\}. \tag{2.15}$$

Apparently $N = |U|$. Algorithm 2.1 describes one possible mapping between $\boldsymbol{k}_l$ and $\boldsymbol{k}_{mn}$. Now, we can express each propagating mode as follows:

Algorithm 2.1 Mapping the pairwise indices (m, n) of propagating modes to the single indices l

1: $m_{\min} = \lfloor -D_x(k + k_x^{inc})/(2\pi) \rfloor, m_{\max} = \lceil D_x(k - k_x^{inc})/(2\pi) \rceil$
2: $n_{\min} = \lfloor -D_y(k + k_y^{inc})/(2\pi) \rfloor, n_{\max} = \lceil D_y(k - k_y^{inc})/(2\pi) \rceil$
3: $l = 0$
4: **for** $n = n_{\min} : n_{\max}$ **do**
5:     **for** $m = m_{\min} : m_{\max}$ **do**
6:         **if** $k_{m,x}^2 + k_{n,y}^2 < k^2$ **then**
7:             $l = l + 1$
8:             mapping l to (m, n)
9:         **end if**
10:    **end for**
11: **end for**

$$\boldsymbol{E}_{mn}^{\pm}(\boldsymbol{r}) = (E_{mn}^{\pm v}\hat{\boldsymbol{v}}_{mn} + E_{mn}^{\pm h}\hat{\boldsymbol{h}}_{mn})e^{-j\boldsymbol{k}_{mn}^{\pm}\cdot\boldsymbol{r}}. \tag{2.16}$$

The modal coefficients $E_{mn}^{\pm v}$ and $E_{mn}^{\pm h}$ can further be decomposed as

$$E_{mn}^{\pm p} = a_{mn}^{\pm p}\sqrt{\frac{\|\boldsymbol{k}_{mn}^{\pm}\|_2}{k_{mn,z}}} = a_{mn}^{\pm p}b_{mn}, \tag{2.17}$$

where p stands for v or h, $a_{mn}^{\pm p}$ is the normalized modal coefficient and b_{mn} is the normalizing coefficient. This decomposition allows us to arrive at the parameter $|a_{mn}^{\pm p}|^2$, which is proportional to the energy density of the p-pol propagating wave flowing in or out of the slab (in $\pm z$ direction). Converting the (m, n) paired indices back to the single l index using Algorithm 2.1, we can express the propagating modes concisely as follows:

$$\boldsymbol{E}_{i,l}^{p\pm}(\boldsymbol{r}) = a_{i,l}^{\pm p}\, b_l\, \hat{\boldsymbol{p}}_l\, e^{-j\boldsymbol{k}_l^{\pm}\cdot\boldsymbol{r}}$$
$$(p = v \text{ or } h, \ \ i = 1 \text{ or } 2, \ \ l = 1, \ldots, K_0), \tag{2.18}$$

in which p stands for the polarization, $i = 1, 2$ indicates the wave in either Region 1 or Region 2, and $K_0 = N$. In the following discussion, we use the specific notation K_0 to denote the number of unique (m, n) pairs for propagating modes rather than the general notation N.

14

It follows from the above discussion that the complete wavefield in either Region 1 or Region 2 can be uniquely represented by a vector of the normalized modal coefficients,

$$\underline{a}_i = \left[\, (\underline{a}_i^+)^T \ \ (\underline{a}_i^-)^T \, \right]^T = \left[\, (\underline{a}_i^{+v})^T \ \ (\underline{a}_i^{+h})^T \ \ (\underline{a}_i^{-v})^T \ \ (\underline{a}_i^{-h})^T \, \right]^T, \qquad (2.19)$$

in which

$$\underline{a}_i^{p\pm} = \left[\, a_{i,1}^{p\pm} \ \ \ldots \ \ a_{i,K_p}^{p\pm} \, \right]^T \tag{2.20}$$

$$(p = v \text{ or } h, \ \ i = 1 \text{ or } 2, \ \ l = 1, \ldots, K_0).$$

Alternatively, we can express the wavefield as incident waves vs. scattered waves with respect to the slab. By doing so, we arrive at the following:

$$\underline{a}^{inc} = \left[\, (\underline{a}_1^+)^T \ \ (\underline{a}_2^-)^T \, \right]^T = \left[\, (\underline{a}_1^{+v})^T \ \ (\underline{a}_1^{+h})^T \ \ (\underline{a}_2^{-v})^T \ \ (\underline{a}_2^{-h})^T \, \right]^T, \qquad (2.21)$$

and

$$\underline{a}^{scat} = \left[\, (\underline{a}_1^-)^T \ \ (\underline{a}_2^+)^T \, \right]^T = \left[\, (\underline{a}_1^{-v})^T \ \ (\underline{a}_1^{-h})^T \ \ (\underline{a}_2^{+v})^T \ \ (\underline{a}_2^{+h})^T \, \right]^T. \qquad (2.22)$$

2.3 Scattering Matrix

With the above prerequisite notation and knowledge, we now introduce the scattering matrix. The scattering matrix linearly relates incident waves and scattered waves. More specifically, using the vectorized wavefield representation $\underline{a}^{inc}$ and $\underline{a}^{scat}$, respectively, the scattering matrix S satisfies

$$\underline{a}^{scat} = S \cdot \underline{a}^{inc}. \tag{2.23}$$

Closely linked to the notion of a scattering matrix is the transfer matrix T, which satisfies:

$$\underline{a}_2 = T \cdot \underline{a}_1. \tag{2.24}$$

There exist equations for transforming S to T and vice versa. However, because the transfer matrix is not numerically stable when used in the cascading process introduced shortly, we only use and analyze the scattering matrix going forward. Indeed, Eq. (2.23) can be expanded as follows:

$$
\begin{bmatrix} \underline{a}_1^- \\ \underline{a}_2^+ \end{bmatrix} = \underbrace{\begin{bmatrix} S_{11} & S_{12} \\ S_{21} & S_{22} \end{bmatrix}}_{=S} \begin{bmatrix} \underline{a}_1^+ \\ \underline{a}_2^- \end{bmatrix},
\tag{2.25}
$$

which explicitly represents the incidence-scattering relationship between Region 1 and Region 2. More completely, we can expand Eq. (2.25) as follows:

$$
\begin{bmatrix} \underline{a}_1^{-v} \\ \underline{a}_1^{-h} \\ \underline{a}_2^{+v} \\ \underline{a}_2^{+h} \end{bmatrix} = \begin{bmatrix} \underbrace{\begin{pmatrix} S_{11}^{vv} & S_{11}^{vh} \\ S_{11}^{hv} & S_{11}^{hh} \end{pmatrix}}_{=S_{11}} & \underbrace{\begin{pmatrix} S_{12}^{vv} & S_{12}^{vh} \\ S_{12}^{hv} & S_{12}^{hh} \end{pmatrix}}_{=S_{12}} \\ \underbrace{\begin{pmatrix} S_{21}^{vv} & S_{21}^{vh} \\ S_{21}^{hv} & S_{21}^{hh} \end{pmatrix}}_{=S_{21}} & \underbrace{\begin{pmatrix} S_{22}^{vv} & S_{22}^{vh} \\ S_{22}^{hv} & S_{22}^{hh} \end{pmatrix}}_{=S_{22}} \end{bmatrix} \begin{bmatrix} \underline{a}_1^{+v} \\ \underline{a}_1^{+h} \\ \underline{a}_2^{-v} \\ \underline{a}_2^{-h} \end{bmatrix},
\tag{2.26}
$$

which explicitly separates the horizontal and vertical polarized field components. Apparently, $S_{ij}^{pq} \in \mathbb{C}^{K_0 \times K_0}, (i, j = 1, 2, \ p, q = v \text{ or } h)$, $S_{ij} \in \mathbb{C}^{2K_0 \times 2K_0} (i, j = 1, 2)$ and $S \in \mathbb{C}^{4K_0 \times 4K_0}$. In the following, we use $K_1 = 2K_0$ and $K_2 = 2K_1$.

2.3.1 Unitarity of the Scattering Matrix

Because the entries of $\underline{a}^{inc}$ and $\underline{a}^{inc}$ are normalized modal coefficients of plane waves, the total energy density flow into the system is $\sum_{l=1}^{K_2} |a_l^{inc}|^2 = \|\underline{a}^{inc}\|_2^2$, and the total energy density flow out of the system is $\sum_{l=1}^{K_2} |a_l^{scat}|^2 = \|\underline{a}^{scat}\|_2^2$. If the system is non-dissipative

(i.e. it does not absorb energy), the physical law of power conservation holds:

$$(\underline{a}^{inc})^H \cdot \underline{a}^{inc} = \|\underline{a}^{inc}\|_2^2 = \|\underline{a}^{scat}\|_2^2$$

$$= \|S \cdot \underline{a}^{inc}\|_2^2 \qquad (2.27)$$

$$= (\underline{a}^{inc})^H \cdot S^H \cdot S \cdot \underline{a}^{inc}$$

Thus,

$$(\underline{a}^{inc})^H \cdot (I - S^H \cdot S) \cdot \underline{a}^{inc} = 0. \qquad (2.28)$$

Because $\underline{a}^{inc} \not\equiv 0$, we have

$$S^H \cdot S = I. \qquad (2.29)$$

Namely, the scattering matrix S is always unitary if the system is lossless.

In the 2D scenario, the scattering matrix has other universal properties, such as time-reversal symmetry and reciprocity [54, 55]. In the 3D scenario, the modes' arrangement is not 1D sortable as that in the 2D scenario; therefore, their indices in a matrix coordinate somehow lose their uniqueness. In other words, there is no universally agreeable way to map the single l index to the paired (m, n) indices as put forth in Algorithm 2.1. In addition, in the 3D for each propagating direction of the modes, there are two different polarization branches (v-pol and h-pol). As a consequence, the properties of time-reversal symmetry and reciprocity for the 3D scattering matrix manifest themselves differently from the 2D scattering matrix.

2.3.2 Cascade Scattering Matrices

A large scatterer may be subdivided into many smaller ones and the scattering matrix of the composite scatterer can be computed from those of its constituent components. The output field of one system becomes the input field of its neighboring systems, and vice versa. This process is illustrated in Figure 2.2. The figure shows two scattering systems characterized by scattering matrices $S^{(1)}$ and $S^{(2)}$ are cascaded. S^{cas} represents the scat-
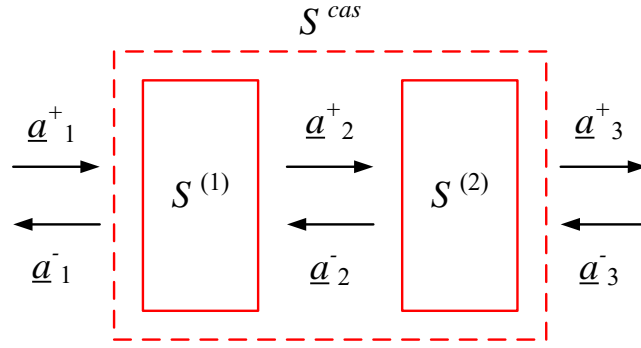
Figure 2.2: Cascaded scattering systems.

tering matrix of the whole system. The fields on the left and right sides are represented by vectors of normalized modal coefficient vectors $\underline{a}_1^{\pm}$ and $\underline{a}_3^{\pm}$, respectively. The intermediate field is represented by the vectors $\underline{a}_2^{\pm}$. Obviously, we have the relationship

$$
\begin{bmatrix} \underline{a}_1^- \\ \underline{a}_2^+ \end{bmatrix} = S^{(1)} \begin{bmatrix} \underline{a}_1^+ \\ \underline{a}_2^- \end{bmatrix}, \begin{bmatrix} \underline{a}_2^- \\ \underline{a}_3^+ \end{bmatrix} = S^{(2)} \begin{bmatrix} \underline{a}_2^+ \\ \underline{a}_3^- \end{bmatrix}, \tag{2.30}
$$

and

$$
\begin{bmatrix} \underline{a}_1^- \\ \underline{a}_3^+ \end{bmatrix} = S^{cas} \begin{bmatrix} \underline{a}_1^+ \\ \underline{a}_3^- \end{bmatrix}. \tag{2.31}
$$

Let

$$
S^{(1)} = \begin{bmatrix} S_{11}^{(1)} & S_{12}^{(1)} \\ S_{21}^{(1)} & S_{22}^{(1)} \end{bmatrix}, S^{(2)} = \begin{bmatrix} S_{11}^{(2)} & S_{12}^{(2)} \\ S_{21}^{(2)} & S_{22}^{(2)} \end{bmatrix}, \tag{2.32}
$$

and

$$
S^{cas} = \begin{bmatrix} S_{11}^{cas} & S_{12}^{cas} \\ S_{21}^{cas} & S_{22}^{cas} \end{bmatrix}. \tag{2.33}
$$

18

Then, S^{cas} can be obtained from $S^{(1)}$ and $S^{(2)}$ [54] as

$$\begin{aligned}
S_{11}^{cas} &= S_{11}^{(1)} + S_{12}^{(1)} \cdot (I - S_{11}^{(2)} \cdot S_{22}^{(1)})^{-1} \cdot S_{11}^{(2)} \cdot S_{21}^{(1)}, \\
S_{12}^{cas} &= S_{12}^{(1)} \cdot (I - S_{11}^{(2)} \cdot S_{22}^{(1)})^{-1} \cdot S_{12}^{(2)}, \\
S_{21}^{cas} &= S_{21}^{(2)} \cdot (I - S_{22}^{(1)} \cdot S_{11}^{(2)})^{-1} \cdot S_{21}^{(1)}, \\
S_{22}^{cas} &= S_{22}^{(2)} + S_{21}^{(2)} \cdot (I - S_{22}^{(1)} \cdot S_{11}^{(2)})^{-1} \cdot S_{22}^{(1)} \cdot S_{12}^{(2)}.
\end{aligned} \tag{2.34}$$

The above cascading scheme is very useful in our study of random media, as will become clear in the following sections.

2.3.3 Assembling the Scattering Matrix

As discussed above, the scattering matrix provides a useful characterization of a scatterer. It serves as a black box characterization of the input-output relationship between fields, and greatly, facilitates our investigation of scattering in random media. We have not yet mentioned how to generate the scattering matrix (beyond how it can be assembled from scattering matrices of subscatterers). There exist many approaches for calculating values of entries of the scattering matrix, the majority of which adhere to the *action and reaction* principle that underlies the definition of the matrix in the first place. Algebraically, if we want to extract the l-th column of the scattering matrix S, we simply multiply S with a unit vector $\underline{e}_l$ with all zero entries except the l-th entry at 1.0. This can be expressed as follows:

$$S_{k=1:K_2,l} = S \cdot \underline{e}_l. \tag{2.35}$$

Physically, this corresponds to the scatterer being illuminated by a plane wave, as

$$\boldsymbol{E}_l^{inc}(\boldsymbol{r}) = a_l \, b_l \, \hat{\boldsymbol{p}}_l \, e^{-j\boldsymbol{k}_l \cdot \boldsymbol{r}}$$

$$(\hat{\boldsymbol{p}} = \text{ either } \hat{\boldsymbol{v}} \text{ or } \hat{\boldsymbol{h}} \text{ depends on } l, \ \ 1 \leq l \leq K_2), \tag{2.36}$$

with $a_l = 1.0$. The scattered waves are generated on both sizes of the system (slab), and can be represented as the collection of propagating modes

$$\boldsymbol{E}_m^{scat}(\boldsymbol{r}) = a_m \, b_m \, \hat{\boldsymbol{p}}_m \, e^{-j\boldsymbol{k}_m \cdot \boldsymbol{r}}$$

$$(\hat{\boldsymbol{p}} = \text{ either } \hat{\boldsymbol{v}} \text{ or } \hat{\boldsymbol{h}} \text{ depends on } m, \quad m = 1, \ldots, K_2),$$

(2.37)

where

$$a_m = \begin{cases} S_{m,l} & \text{if } \boldsymbol{k}_m \neq \boldsymbol{k}_l, \\ S_{m,l} - a_l e^{-jk_z^{(l)}d} & \text{otherwise.} \end{cases}$$

(2.38)

The relationship between a_m and $S_{m,l}$ in Eq. (2.38) is due to the fact that the scattering system's output contains not only the induced scattering waves but also the incident wave, which passes through the system and exits on the other side. Thus, if the propagating direction of the scattered mode is the same as the incident mode, the modal coefficient of the output mode is the superposition of both the scattered mode and the incident mode. As a result, we have $S_{m,l} = a_m + a_l e^{-jk_z^{(l)}d}$ for $\boldsymbol{k}_m = \boldsymbol{k}_l$, where d is the distance along the z direction between the observation points of the incident and scattered modes, respectively.

The index m and l ($1 \leq m, l \leq K_2$) in Eq. (2.36) and (2.37) can be mapped to the indices l, i ($1 \leq l \leq K_0, i = 1, 2$) in Eq. (2.18) with the additional "$\pm$" indicator for specifying the origin of the incident/scattered waves (from Region 1 or Region 2) and their incident/scattered directions with respect to $\pm z$.

The underlying physical process mentioned above involves a classical scattering problem (with the periodic boundary condition) in electromagnetics, and there exists a variety of ways to solve it. Specifically, by giving the obstacle and specifying the incident wave, through solving the Maxwell's equations we can find the complex amplitude E_m ($m = 1, \ldots, K_2$) of the scattered propagating modes. After the normalization, we then can obtain each entry $S_{m,l}$ ($m = 1, \ldots, K_2$) for the l-th column of S. The procedure for assembling the scattering matrix is illustrated briefly in Algorithm 2.2.

Algorithm 2.2 Procedure for assembling the scattering matrix

 1: **for** $l = 1 : K_2$ **do**
 2:     Excite the system with planewave $\boldsymbol{E}_l^{inc}(\boldsymbol{r}) = b_l\ \hat{\boldsymbol{p}}_l\ e^{-j\boldsymbol{k}_l \cdot \boldsymbol{r}}$
 3:     Solve the Maxwell's equations of the underlying scattering problem
 4:     Find the complex amplitudes E_m of $\boldsymbol{E}_m^{scat}(\boldsymbol{r}) = E_m\ \hat{\boldsymbol{p}}_m\ e^{-j\boldsymbol{k}_m \cdot \boldsymbol{r}}$ for $m = 1, \ldots, K_2$
 5:     **for** $m = 1 : K_2$ **do**
 6:        **if** $\boldsymbol{k}_m = \boldsymbol{k}_l$ **then**
 7:            $S_{m,l} = E_m/b_m + a_l e^{-jk_z^{(l)}d}$
 8:        **else**
 9:            $S_{m,l} = E_m/b_m$
10:        **end if**
11:     **end for**
12: **end for**

2.4 Integral Equation Method for Solving the Scattering Problem

Key to generating the scattering matrix is solving the electromagnetic scattering problem for each incident mode. In practice, both the accuracy of the solution and the efficiency of the solution method are important parameters to consider when selecting a specific solver technique. Previous research into the 2D scenario [54, 55] modeled the unit scatterer in the random media as a small cylinder, solving Maxwell's equation via an analysis-based, T-matrix (not transfer matrix) inspired method. Specifically, in 2D, the waves scattered by a cylindrical scatterer are cylindrical waves, and their scattering coefficients can be obtained analytically. Use of the interaction matrix approach (T-matrix) allow one to capture the electromagnetic interaction of multiple cylindrical scatterers. By applying periodic boundary condition and converting outgoing cylindical waves into plane waves, one obtains the final solution. The advantage of this method is that it is rooted into the analytical Mie series, thereby exhibiting spectral accuracy. Although a similar technique for dealing with 3D spherical scatterers that uses spherical wave expansion and corresponding T-matrix techniques exists [64], we decided to solve Maxwell's equation using the integral equation (IE) method, viz. the Method of Moments (MoM). This choice reflects our desire to popu-

late the scattering medium with a diversity of dipole-like or cross-dipole-like objects rather than spherical objects. We expect this approach can generate more randomness in our 3D random media model. Based on this consideration, IE methods constitute a natural choice as they easily allow dealing with scatterers of arbitrary shapes. Although the IE method is not spectrally accurate, our numerical simulations demonstrate that the IE's solution is sufficiently accurate for our purposes.

2.4.1 Electric Field Integral Equation with Periodic Boundary Condition

Non-absorbing (lossless) scatterers may either be perfect electrically conducting (PEC) or dielectric in nature. PEC objects usually exhibit stronger scattering than dielectric ones of the same size and shape; they also tend to be simpler model using IE techniques. For the above reasons, we assume all scatterers are PEC in nature. Let Γ denote an arbitrarily-shaped, PEC surface residing in free space and repeating itself in a periodic lattice. The time harmonic electric field $\boldsymbol{E}^{inc}(\boldsymbol{r})$ impinges on Γ and induces a surface current, in turn generating a scattered electromagnetic field. Enforcing electromagnetic boundary conditions on Γ yields the following electric field integral equation (EFIE):

$$\hat{\boldsymbol{n}} \times \hat{\boldsymbol{n}} \times ik\eta \int_{\Gamma} d\boldsymbol{r}' \boldsymbol{J}(\boldsymbol{r}') \cdot \left(\boldsymbol{I} - \frac{\nabla\nabla'}{k^2} \right) g_p(\boldsymbol{r}, \boldsymbol{r}') = -\hat{\boldsymbol{n}} \times \hat{\boldsymbol{n}} \times \boldsymbol{E}^{inc}. \tag{2.39}$$

Here, $\boldsymbol{r} \in \Gamma$, k and η denote the wavenumber and wave impedance in free space, $\hat{\boldsymbol{n}}$ denotes the outward unit normal to S, $\boldsymbol{I}$ is the identity dyad, and $g_p(\boldsymbol{r}, \boldsymbol{r}')$ is the 3D periodic free space Green's function. To numerically solve the EFIE, the current $\boldsymbol{J}(\boldsymbol{r})$ is discretized with N local basis functions as

$$\boldsymbol{J}(\boldsymbol{r}) = \sum_{j=1}^{N} I_j \boldsymbol{f}_j(\boldsymbol{r}). \tag{2.40}$$

Here, I_j is the current expansion coefficient associated with the j-th basis function $\boldsymbol{f}_j(\boldsymbol{r}')$. If S is discretized using a triangular mesh, the Rao-Wilton-Glisson (RWG) basis [65] function are most often used. Using Galerkin testing, a $N \times N$ linear system of equations is obtained

$$\boldsymbol{Z} \cdot \boldsymbol{I} = \boldsymbol{V}. \tag{2.41}$$

Here, the entries of the impedance matrix $\boldsymbol{Z}$ are

$$\begin{aligned}
\boldsymbol{Z}_{ij} = -ik\eta \int_\Gamma d\boldsymbol{r} \int_\Gamma d\boldsymbol{r}' g_p(\boldsymbol{r}, \boldsymbol{r}')[\boldsymbol{f}_i(\boldsymbol{r}) \cdot \boldsymbol{f}_j(\boldsymbol{r}')] \\
+ \frac{i\eta}{k} \int_\Gamma d\boldsymbol{r} \int_\Gamma d\boldsymbol{r}' g_p(\boldsymbol{r}, \boldsymbol{r}')[\nabla \cdot \boldsymbol{f}_j(\boldsymbol{r}) \nabla' \cdot \boldsymbol{f}_j(\boldsymbol{r}')].
\end{aligned} \tag{2.42}$$

The j-th entry of the solution vector $\boldsymbol{I}$ is $I_j, j = 1, \ldots, N$, and the i-th entry of the excitation vector $\boldsymbol{V}_i, i = 1, \ldots, N$ is

$$\boldsymbol{V}_i = \int_\Gamma d\boldsymbol{r} \boldsymbol{f}_i(\boldsymbol{r}) \cdot \boldsymbol{E}_l^{inc}(\boldsymbol{r}). \tag{2.43}$$

Here, $\boldsymbol{E}_l^{inc}(\boldsymbol{r}), l = 1, \ldots, K_2$ is the l-th incident electric field expressed in Eq. (2.36). Because the scatterers analyzed herein are usualy small, so is N, the linear system in Eq. (2.41) can be easily inverted via LU decomposition. The MoM solution provides the surface current $\boldsymbol{J}_l(\boldsymbol{r}'), \boldsymbol{r}' \in \Gamma, l = 1, \ldots, K_2$ due to the incident field of each mode. Due to the l-th incident mode, the corresponding scattered field of the m-th mode (including both v-pol and h-pol components, thus $m = 1, \ldots, K_1$) at $\boldsymbol{r}$ can be obtained as

$$\boldsymbol{E}_{m,l}^{scat}(\boldsymbol{r}) = \boldsymbol{E}_{m,l}^v(\boldsymbol{r}) + \boldsymbol{E}_{m,l}^h(\boldsymbol{r}) = -\frac{j\eta k}{2 D_x D_y |k_{m,z}|} \int_\Gamma d\boldsymbol{r}' \boldsymbol{J}_l(\boldsymbol{r}') e^{-j\boldsymbol{k}_m \cdot (\boldsymbol{r} - \boldsymbol{r}')}, \tag{2.44}$$

Here, $\boldsymbol{k}_m$ $(m = 1, \ldots, K_1)$ is a wavevector of a certain propagating mode with a specified $\pm$ sign for $k_{m,z}$. By further separating the v-pol and h-pol components from $\boldsymbol{E}_{m,l}^{scat}(\boldsymbol{r})$, we can obtain the complete K_2 modal coefficients E_m $(m = 1, \ldots, K_2)$ of the K_2 scattered modes. Finally, after proper normalization of $a_m = E_m/b_m$ and including the incident

23

mode, we obtain the l-th column of the scattering matrix.

2.4.2 Periodic Green's Function in 3D

The accurate computation of the periodic Green's function $g_p(\boldsymbol{r}, \boldsymbol{r}')$ is critical ensuring the accuracy of the IE solutions. In the spatial domain, the 3D periodic Green's function can be expressed as

$$g_p(\boldsymbol{r}, \boldsymbol{r}') = \sum_{m=-\infty}^{+\infty} \sum_{n=-\infty}^{+\infty} g(\boldsymbol{r}, \boldsymbol{r}'_{mn}), \tag{2.45}$$

where

$$\boldsymbol{r}'_{mn} = \boldsymbol{r}' + (mD_x, nD_y, 0), \tag{2.46}$$

and

$$g(\boldsymbol{r}, \boldsymbol{r}') = \frac{e^{-jk|\boldsymbol{r}-\boldsymbol{r}'|}}{4\pi|\boldsymbol{r} - \boldsymbol{r}'|}, \tag{2.47}$$

represents the non-periodic Green's function in free space. In practice we often truncate the series by only summing up the terms of $\{(m,n) \mid M_{\min}^{spat} \leq m \leq M_{\max}^{spat}, \ N_{\min}^{spat} \leq n \leq N_{\max}^{spat}\}$ for certain $\left(M_{\min(\max)}^{spat}, N_{\min(\max)}^{spat}\right)$ that satisfy our accuracy requirement. However, the convergence of Eq. (2.45) is often slow; therefore, we usually expand $g_p(\boldsymbol{r}, \boldsymbol{r}')$ in the spectral domain as well as

$$g_p(\boldsymbol{r}, \boldsymbol{r}') = \sum_{m=-\infty}^{+\infty} \sum_{n=-\infty}^{+\infty} \frac{e^{-j[k_{m,x}(x-x')+k_{n,y}(y-y')+k_{mn,z}|z-z'|]}}{2jD_xD_yk_{mn,z}}, \tag{2.48}$$

where

$$k_{m,x} = k_x^{(1)} + \frac{2m\pi}{D_x}, \quad k_{n,y} = k_y^{(1)} + \frac{2n\pi}{D_y}, \tag{2.49}$$

and

$$k_{mn,z} = \begin{cases} \sqrt{k^2 - k_{m,x}^2 - k_{n,y}^2}, & k^2 > k_{m,x}^2 + k_{n,y}^2, \\ -j\sqrt{k_{m,x}^2 + k_{n,y}^2 - k^2}, & k^2 < k_{m,x}^2 + k_{n,y}^2. \end{cases} \tag{2.50}$$

In the above expressions, $\boldsymbol{r} = (x, y, z), \boldsymbol{r}' = (x', y', z')$. $\boldsymbol{k}^{(1)} = (k_x^{(1)}, k_y^{(1)}, k_{00,z})$ defines the first modes, and in our application we initialize it with $k_x^{(1)} = k_y^{(1)} = 0$. Similar to the spatial series, the infinite summation of Eq. (2.48) converges and can be approximated by a finite summation for some $M_{\min(\max)}^{spec}$ and $N_{\min(\max)}^{spec}$ that $M_{\min}^{spec} \leq m \leq M_{\max}^{spec}$ and $N_{\min}^{spec} \leq n \leq N_{\max}^{spec}$. The convergence of the spectral summation can be accelerated further with the Shanks transformation [66–68].

2.4.3 Shanks Transformation

The Shanks transformation operates on a convergent series

$$C = \sum_{i=1}^{\infty} c_i. \tag{2.51}$$

To determine C, we define the partial sum C_l as

$$C_l = \sum_{i=1}^{l} c_i. \tag{2.52}$$

Of course, $\lim_{l \to \infty} C_l = C$. The Shanks transformation defines a new sequence $S(C_l)$ based on the non-linear transformation of C_l as

$$S(C_l) = C_{l+1} - \frac{(C_{l+1} - C_l)^2}{C_{l+1} - 2C_l + C_{l-1}}. \tag{2.53}$$

It is easy to show that that $S(C_l)$ also converge to C, and usually, it converges more rapidly than C_l. Further speedup may be obtained by repeating the use of the Shanks transformation, as $S^2(C_l) = S(S(C_l)), S^3(C_l) = S(S(S(C_l)))$ and so on.

To use the Shanks transformation to calculate $g_p(\boldsymbol{r}, \boldsymbol{r}')$, we rearrange the spectral sum

of $g_p(\boldsymbol{r}, \boldsymbol{r}')$ as

$$g_p(\boldsymbol{r}, \boldsymbol{r}') = c_{0,0} + \sum_{i=1}^{\infty} \left(\sum_{m=-i}^{i} (c_{m,i} + c_{m,-i}) + \sum_{n=-i+1}^{i-1} (c_{i,n} + c_{-i,n}) \right)$$

$$= c_{0,0} + \sum_{i=1}^{\infty} B_i, \tag{2.54}$$

where

$$c_{m,n} = \frac{e^{-j[k_{m,x}(x-x')+k_{n,y}(y-y')+k_{mn,z}|z-z'|]}}{2j D_x D_y k_{mn,z}}. \tag{2.55}$$

Next, we can extract the partial summation $g_p^l(\boldsymbol{r}, \boldsymbol{r}')$ as follows:

$$g_p^l = c_{0,0} + \sum_{i=1}^{l} B_i, \tag{2.56}$$

and accordingly apply the Shanks transformation $S(g_p^l)$. Essentially, the partial summation g_p^l consists of elements $c_{m,n}$ with their indices (m, n) forming a rectangular region $[m = -l : l, n = -l : l]$, and B_i is the collection of $c_{m,n}$ on the boundary of the rectangular region $[m = -i : i, n = -i : i], i = 1, \ldots, l$. Although the number of elements $c_{m,n}$ increases in B_i along with the increase of the index i, their summation, viz. B_i decreases accordingly.

2.5 Generating Random Media

2.5.1 Single-Layer Slab

Consider a single-layer slab with lattice vectors $D_x \hat{\boldsymbol{x}}$ and $D_y \hat{\boldsymbol{y}}$ that contains a single particle, e.g. a small PEC dipole, cross dipole, and so on. The dimension of the particle are smaller than $\min(D_x, D_y)$ typically not an order of magnitude smaller. Figure (2.3) illustrates a sample single layer slab consisting of cross dipole scatterers. The particle is discretized with surface mesh its scattering matrix is computed using the above outlined

26
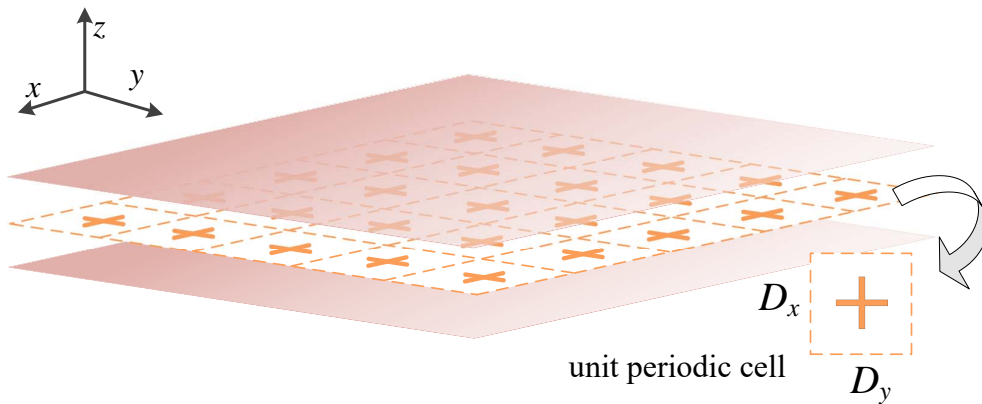
Figure 2.3: Illustration of a single-layer slab consisting of PEC cross dipole scatterers.

procedures.

2.5.2 Multi-layer Slab

A multi-layer slab is obtained by cascading many single layer slabs. Each slab has the same lattice vectors $D_x \hat{x}$ and $D_y \hat{y}$ but contains a different scatterers. Scatterers in different layers vary in shape, size and position in the plane of periodicity. Assuming the slab contains many layers and scatterers in all layers are randomly chosen, the slab can be regarded as a random medium. It is worth mentioning that even if we only have a small number of distinct scatterers in terms of shapes and sizes, repeatedly arranging them only in terms of variation in horizontal location (position shifting) can provide adequate randomness. In addition, there is a computationally efficient way to generate a new scattering system based on an existing scattering system if the scatterers in the new system only differs from those of an existing system with a position shifting. A sample multi-layer slab is shown in Figure 2.4. Rather than creating this multi-layer slab all at once, we assemble it by cascading many single-layer slabs; more precisely, by cascading their scattering matrices $S^{(i)}$. The cascading procedure is illustrated in Algorithm 2.3, and it is easy to parallelize. In Algorithm 2.3,
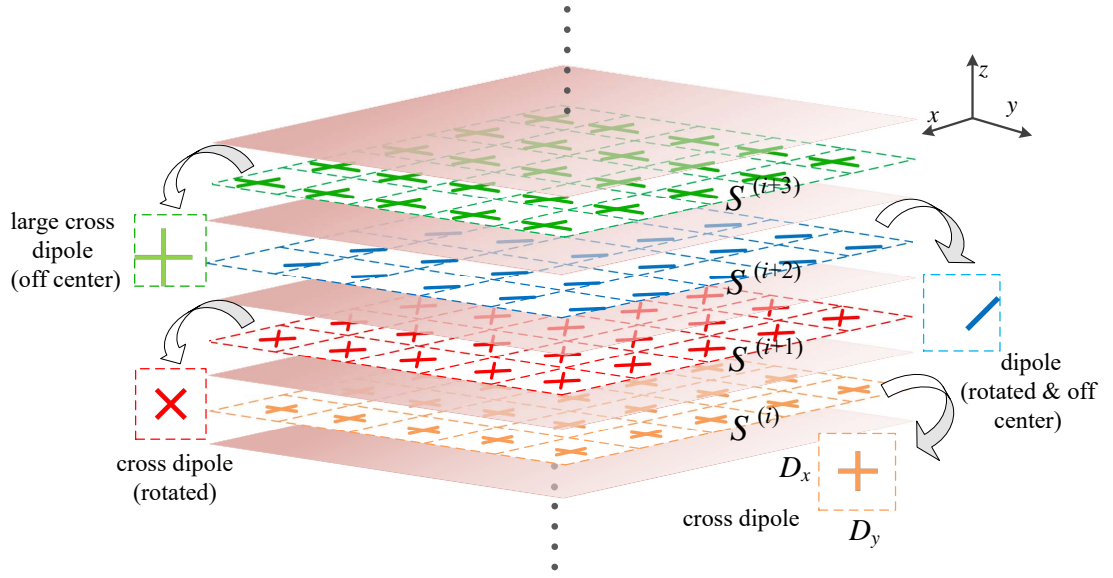
Figure 2.4: Illustration of a multi-layer slab consisting of a variety of PEC scatterers.

Algorithm 2.3 Procedure of cascading many scattering matrices

---

1: $S := S^{(0)}$
2: **for** $i = 1 : L_c$ **do**
3:     Cascade S and $S^{(i)}$ using the formulas in Eq. (2.34), resulted in S'
4:     $S := S'$
5: **end for**

---

the initial scattering matrix $S^{(0)}$ is set as

$$
S^{(0)} = \begin{bmatrix} 0 & I^{K_1 \times K_1} \\ I^{K_1 \times K_1} & 0 \end{bmatrix},
\tag{2.57}
$$

which represents a scattering system of free space, with the property of complete light transmission (no reflection). Ultimately, the final cascaded S can represent a scattering matrix for a random medium.

2.6   Conclusion

This chapter presented a systematic strategy for constructing a random medium model. The EM scattering properties of this model are characterized by a set of countable and finite solutions and that satisfy periodic boundary conditions. Using an IE method and a cascading scheme allows us to generate an instance of this model accurately and efficiently.

CHAPTER 3

Validation of 3D Random Media Model

3.1   Introduction

Random media composed of particles embedded in a uniform background hinder the passage of EM waves. For thick slabs of such media, the backscattered wave usually dominates the transmitted one, even if the medium and scatterers are lossless. The discovery of so-called "perfectly transmitting wavefronts", viz. carefully crafted wavefronts that pass through such slabs unobstructed, may pave the way for new EM imaging and radar detection techniques that require deep wave penetration into media [42–46, 63]. Several studies have provided numerical evidence for the existence of such wavefronts, even in strongly backscattering random media. For example, work by Jin [54, 55] demonstrates the existence of such wavefronts in a 2D random media consisting of PEC or dielectric cylinders embedded in a lossless host.

Here, we extend the research of Jin into perfectly transmitting wavefronts to 3D. As briefly mentioned in Section 2.5.2, our 3D random media consists of a multi-layer slab consisting of PEC particles randomly distributed in a homogeneous background. The geometries of the particles range from dipoles to crosses and so forth. These dipole-like particles provide strong EM scattering. Rather than using an analysis-based simulation model as Jin did for 2D random media [54, 55], the 3D MoM method is used here to capture the EM scattering mechanism. Numerical simulation demonstrated that even when the

number of layers and particle density is high, there remain a few perfectly/highly transmitting wavefronts with transmission coefficients near unity. The transmission coefficients of the eigen-wavefronts manifest themselves as the singular values of the forward scattering matrix S_{21} and their distribution matches theoretical predictions accurately. Moreover, the phase and magnitude of the highly transmitted (or highly backscattered) eigen-wavefronts are readily presented as the right singular vectors of S_{21}. Similar to the case in the 2D random media study [55], we show that the modes can be constructed efficiently using a simple steepest descent or conjugate gradient algorithm that only requires knowledge of the reflection matrix S_{11}. we show that the modes can be constructed efficiently using a simple steepest descent or conjugate gradient algorithm that only requires knowledge of the reflection matrix S11. Furthermore, we show that with the additional measurements of field intensity at desired points, a simple and efficient Lanczos-like algorithm can be applied to focus energy with approximately 90% efficiency relative to the optimal intensity using only a few measurements. Each step in the above algorithms has a clear physical interpretation, opening up avenues for the algorithms' physical implementation in future radar and imaging systems.

3.2 Problem Definition

The scattering problem considered here involves the 3D random media model described in the previous chapter. We consider a 3D slab of thickness L along the z direction ($L \leq z < 0$) and periodicities D_x and D_y in the x and y directions, respectively. N_c perfect electrically conducting (PEC) particles are placed inside each periodic cell; the particles are separated along the z direction by a distance distance l and occupy random positions in the xy plane. The particles can take on many shapes, from dipoles to crossed dipoles, and vary in size, shape, and orientation. The particles sizes are usually smaller than the wavelength λ but may be resonant in nature and hence scatter strongly. Upon illumination

by EM wavefronts from Region 1, scattered wavefronts are produced in both Regions 1 and Region 2 (Figure 3.1). Let S denote the scattering matrix of this system. Vectors
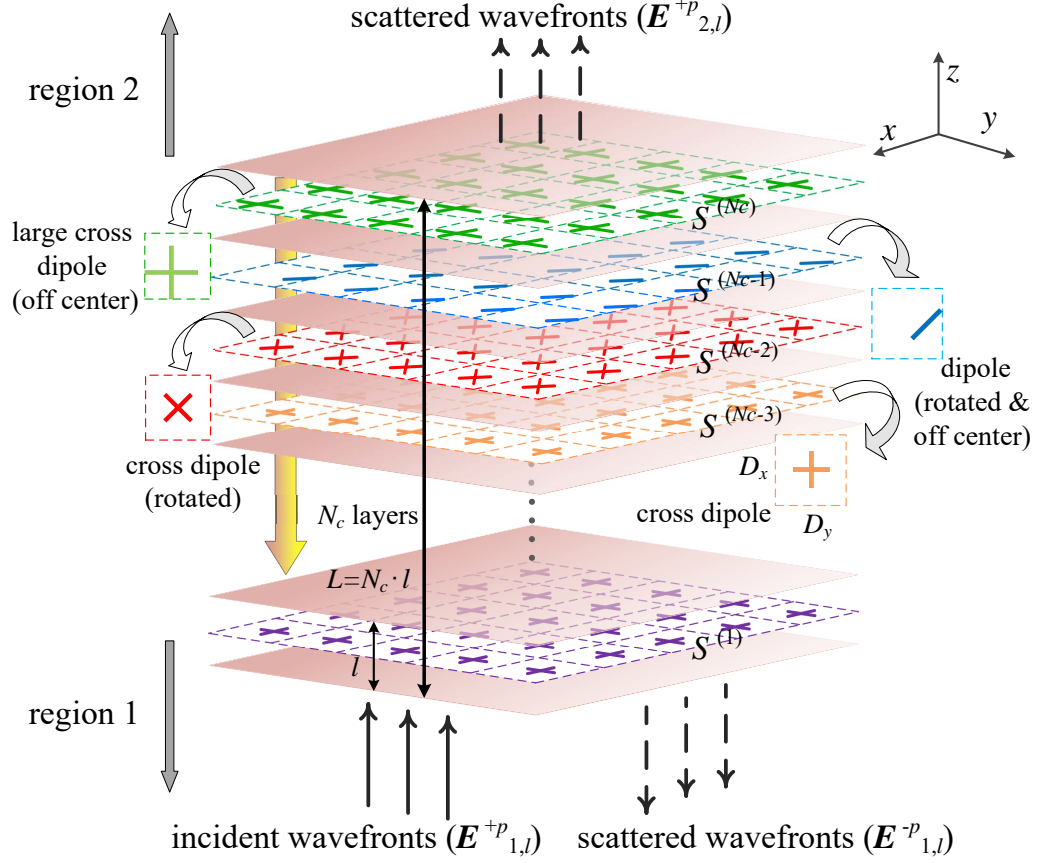
Figure 3.1: The scattering problem involving the 3D random media model.

of normalized modal coefficients are denoted by $\underline{a}_i^{\pm}$, where $i = 1, 2$ indicates the space occupied by the mode (Region 1 or Region 2), and $\pm$ indicates the direction the mode propagates in ($+z$ or $-z$). Because the incident wavefronts only come from $z = -\infty$, we have $\underline{a}_2^- = 0$. The transmission and reflection coefficients are defined as

$$\tau(\underline{a}_1^+) := \frac{\|S_{21} \cdot \underline{a}_1^+\|_2^2}{\|\underline{a}_1^+\|_2^2}, \tag{3.1}$$

and

$$\Gamma(\underline{a}_1^+) := \frac{\|S_{11} \cdot \underline{a}_1^+\|_2^2}{\|\underline{a}_1^+\|_2^2}, \tag{3.2}$$

respectively. $\underline{a}_{\text{norm}}$ is used to denote the normally incident wavefront, which has $K_2 - 1$ zero entries except $a_{1,l}^{+v} = 1.0$, for which $\boldsymbol{k}_l = (0, 0, k)$. The transmission coefficient of the normally incident wavefront is denoted by

$$\tau_{\text{norm}} = \tau(\underline{a}_{\text{norm}}). \tag{3.3}$$

3.3 Wave Transmission in Random Media

3.3.1 Transmission Coefficients

In the lossless setting, the scattering matrix S in Eq. (2.23) is unitary, as proved in Section 2.3.1. As a result, we have

$$S_{11}^H \cdot S_{11} + S_{21}^H \cdot S_{21} = (S^H \cdot S)_{1:K_1, 1:K_1} = I^{K_1 \times K_1}, \tag{3.4}$$

and therefore

$$S_{21}^H \cdot S_{21} = I - S_{11}^H \cdot S_{11}. \tag{3.5}$$

Because $S_{21}^H \cdot S_{21}$ is a Hermitian matrix, there exists an eigen-decomposition

$$S_{21}^H \cdot S_{21} = V \cdot \Lambda \cdot V^H = I - S_{11}^H \cdot S_{11}, \tag{3.6}$$

where V is a unitary matrix, and Λ is a diagonal matrix with all its diagonal elements $\{\lambda_1, \ldots, \lambda_{K_1}\}$ being real and positive. λ_i, $i = 1, \ldots, K_1$ is called the i-th eigenvalue of $S_{21}^H \cdot S_{21}$; we assume these eigenvalues are sorted in descending order, i.e. $\lambda_1 \geq \lambda_2 \geq \cdots \geq$

$\lambda_{K_1} \geq 0$. Column $\underline{v}_i$, $i = 1, \ldots, K_1$ of V is called the i-th eigenvector. It is easily shown that

$$\lambda_i \, \underline{v}_i = (S_{21}^H \cdot S_{21}) \cdot \underline{v}_i. \tag{3.7}$$

From Eq. (3.6) we can also obtain the eigen-decomposition of $S_{11}^H \cdot S_{11}$ as

$$S_{11}^H \cdot S_{11} = V \cdot (I - \Lambda) \cdot V^H, \tag{3.8}$$

which implies that $S_{11}^H \cdot S_{11}$ and $S_{21}^H \cdot S_{21}$ have the same eigenvectors. In addition, we arrive at

$$\widetilde{\lambda}_{K_1-i} = 1 - \lambda_i, \; i = 1, \ldots, K_1, \tag{3.9}$$

in which $\widetilde{\lambda}_i$, $i = 1, \ldots, K_1$ are the eigenvalues of $S_{11}^H \cdot S_{11}$, with the arrangement $\widetilde{\lambda}_1 \geq \widetilde{\lambda}_2 \geq \cdots \geq \widetilde{\lambda}_{K_1} \geq 0$. Let $\widetilde{\underline{v}}_i$ denotes the eigenvector of $S_{11}^H \cdot S_{11}$ corresponding to $\widetilde{\lambda}_i$. It follows that,

$$\begin{cases} 0 \leq \lambda_i \leq 1, \; 0 \leq \widetilde{\lambda}_i \leq 1 \\ \lambda_i + \widetilde{\lambda}_{K_1-i+1} = 1 \\ \underline{v}_i = \widetilde{\underline{v}}_{K_1-i+1} \end{cases} , \; i = 1, \ldots, K_1. \tag{3.10}$$

In addition, let $S_{21} = \sum_{i=1}^{K_1} \sigma_i \, \underline{u}_i \cdot \underline{v}_i^H$ and $S_{11} = \sum_{i=1}^{K_1} \widetilde{\sigma}_i \widetilde{\underline{u}}_i \cdot \widetilde{\underline{v}}_i^H$ denote the singular value decompositions (SVD) of S_{21} and S_{11}, respectively. Here σ_i (resp. $\widetilde{\sigma}_i$) is the singular value corresponding to the left and right singular vectors $\underline{u}_i$ and $\underline{v}_i$ (resp. $\widetilde{\underline{u}}_i$ and $\widetilde{\underline{v}}_i$), respectively. By convention, the singular values are arranged in the order of $\sigma_1 \geq \ldots \geq \sigma_{K_1}$ and $\widetilde{\sigma}_1 \geq \ldots \geq \widetilde{\sigma}_{K_1}$. It follows from basic linear algebra theory [69] that the eigenvalue λ_i of matrix $A^H \cdot A$ is the squared singular value σ_i of matrix A, and the eigenvector of $A^H \cdot A$ is the right singular vector of A. Therefore, from Eq. (3.10) we have

$$\begin{cases} \sigma_i^2 + \widetilde{\sigma}_{K_1-i+1}^2 = 1 \\ \underline{v}_i = \widetilde{\underline{v}}_{K_1-i+1} \end{cases} , \; i = 1, \ldots, K_1. \tag{3.11}$$

The $\sigma_i (i = 1, \ldots, K_1)$ are called the characteristic transmission coefficients of the scattering system. Correspondingly, the complementary $\widetilde{\sigma}_{K_1-i+1}(i = 1, \ldots, K_1)$ are called the characteristic reflection coefficients of the scattering system.

An arbitrary incident wavefront coming from Region 1 can be represented by a normalized modal coefficient vector $\underline{a}_1^+$; $\underline{a}_1^+$ can be uniquely expressed as the linear combination of the right singular vectors of S21 (or S11 equivalently) because the singular vectors are orthonormal, as

$$\underline{a}_1^+ = \sum_{i=1}^{K_1} c_i \, \underline{v}_i, \tag{3.12}$$

where c_i is the complex amplitude of the base $\underline{v}_i$. Physically, each $\underline{v}_i$ also represents the normalized modal coefficients a vector representing an incident wavefront coming from Region 1, called the i-th eigen-wavefront. Thus, $|c_i|$ is the amplitude of the i-th eigen-wavefront and

$$\left\| \underline{a}_1^+ \right\|_2^2 = \sum_{i=1}^{K_1} |c_i|^2. \tag{3.13}$$

The energy density passing through the random medium due to an incident wavefront $\underline{a}_1^+$ can be calculated as

$$\begin{aligned} \left\| S_{21} \cdot \underline{a}_1^+ \right\|_2^2 &= (\underline{a}_1^+)^H \cdot S_{21}^H \cdot S_{21} \cdot \underline{a}_1^+ \\ &= (\underline{a}_1^+)^H \cdot V \cdot \Lambda \cdot V^H \cdot \underline{a}_1^+. \end{aligned} \tag{3.14}$$

From Eq. (3.12), we have

$$V^H \cdot \underline{a}_1^+ = \begin{bmatrix} c_1 & c_2 & \ldots & c_{K_1} \end{bmatrix}^T, \tag{3.15}$$

and

$$\left\| S_{21} \cdot \underline{a}_1^+ \right\|_2^2 = \sum_{i=1}^{K_1} |c_i|^2 \sigma_i^2. \tag{3.16}$$

Similarly, we have

$$\left\| S_{11} \cdot \underline{a}_1^+ \right\|_2^2 = \sum_{i=1}^{K_1} |c_i|^2 \widetilde{\sigma}_{K_1-i+1}^2. \tag{3.17}$$

Consequently, the relationship between the transmitted and the reflected power arises from

$$\left\| S_{21} \cdot \underline{a}_1^+ \right\|_2^2 + \left\| S_{11} \cdot \underline{a}_1^+ \right\|_2^2 = \left\| \underline{a}_1^+ \right\|_2^2. \tag{3.18}$$

If both sides of Eq. (3.18) are divided by the energy density of the incident wavefront $\|\underline{a}_1^+\|_2^2$, then we arrive at

$$\tau(\underline{a}_1^+) + \Gamma(\underline{a}_1^+) = 1, \tag{3.19}$$

which essentially states the law of conservation of energy.

3.3.2 Transmission Coefficient Distribution

Several studies [38–41, 63] have revealed that the theoretical distribution of the transmission coefficients for non-absorbing random media has the bimodal shape given by

$$f(\tau) = \lim_{M \to \infty} \frac{1}{M} \sum_{i=1}^{M} \delta\left(\tau - \tau(\underline{v}_i)\right) = \frac{\ell}{2L} \frac{1}{\tau\sqrt{1-\tau}},$$

$$\text{for } 4e^{-L/2\ell} \lessapprox \tau \leq 1, \tag{3.20}$$

In which ℓ is the mean-free path through the media. Figure (3.2) shows the theoretical density when $L/\ell = 3$. Eq. (3.20) is known as the Dorokhov-Mello-Pereyra-Kumar (DMPK) equation, named after the researchers who first proposed it. Numerically, the transmission coefficients manifest themselves as the squared singular values $\sigma_i(i = 1, \ldots, K_1)$ of S_{21} as mentioned above. To investigate the empirical distribution of the transmission coefficient of 3D non-absorbing random media, we undertake a simulation of 10,000 random trials. The accumulated distribution of the transmission coefficients of eigen-wavefronts is shown in Figure 3.3. All the stochastic slabs have $D_x = D_y = 9.85\lambda$, $l = 4.0\lambda$, $K_1 = 690$ and the
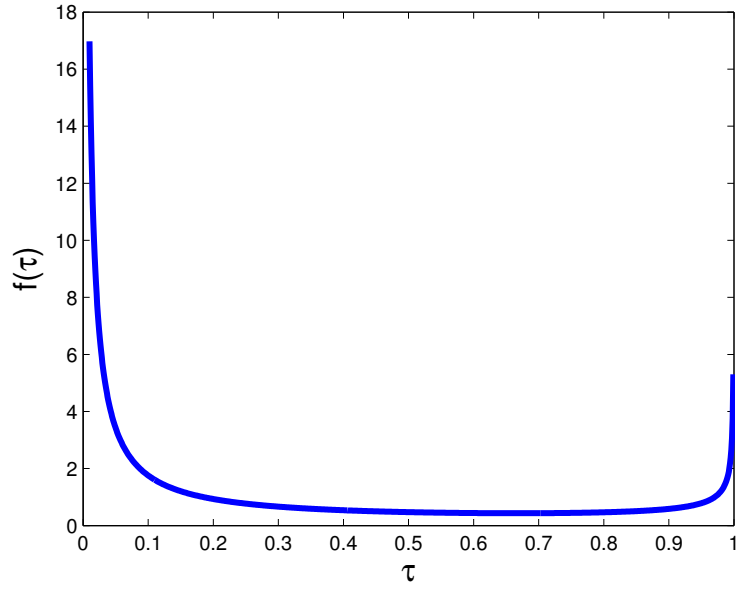
Figure 3.2: Theoretical distribution of the transmission coefficients in Eq. (3.20) for $L/l = 3$.

number of layers is $N_c = 4150$. The results conform to and confirm the bimodal shape of the theoretical distribution in Figure 3.2. Taking a closer look at the "perfect transmission" end, we find that the experiment histogram fits the trend of Eq. (3.20) for $\sigma \to 1.0$ very well.
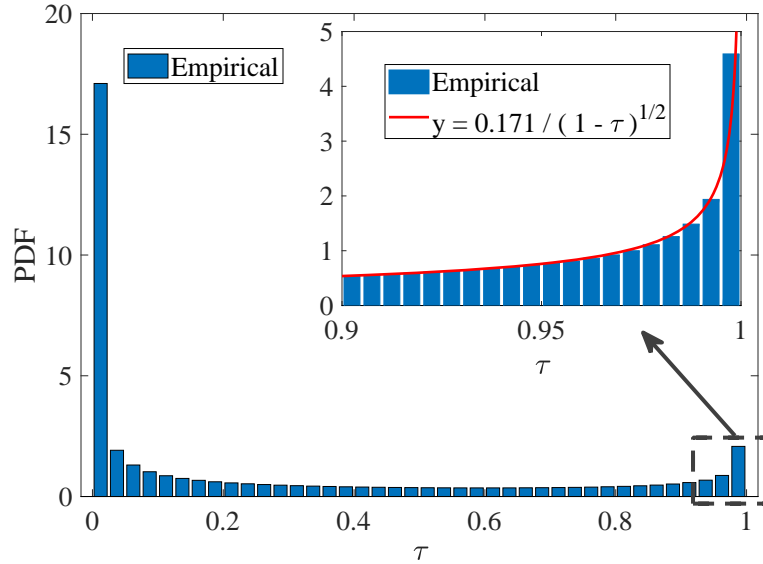
Figure 3.3: The accumulated distribution of the transmission coefficient over 10,000 random trials for $D_x = D_y = 9.85\lambda$, $l = 4.0\lambda$, $K_1 = 690$ and $N_c = 4150$.

3.3.3 Transmission Maximization

Transmission maximization refers to an optimization problem that seeks the incident wavefront $\underline{a}_1^+$ that maximizes the objective function

$$
\begin{aligned}
\underline{a}_{\text{opt}} &= \arg\max_{\underline{a}_1^+} \tau(\underline{a}_1^+) = \arg\max_{\underline{a}_1^+} \frac{\|S_{21} \cdot \underline{a}_1^+\|_2^2}{\|\underline{a}_1^+\|_2^2} \\
&= \arg\max_{\|\underline{a}_1^+\|_2=1} \|S_{21} \cdot \underline{a}_1^+\|_2^2,
\end{aligned}
\tag{3.21}
$$

Here, $\| \underline{a}_1^+ \|_2 = 1$ is a power constraint for the incident wavefront. In the lossless setting, this problem has a closed form solution

$$
\underline{a}_{\text{opt}} = \underline{v}_1,
\tag{3.22}
$$

where $\underline{v}_1$ is the first right singular vector of S_{21} and consequently $\tau_{\max} = \tau(\underline{v}_1) = \sigma_1^2$. In other words, we can directly obtain $\underline{a}_{\text{opt}}$ when S_{21} is available. If S_{21} is not available, Jin et al. provided two iterative methods steepest descent and conjugate gradient to find an approximation of $\underline{a}_{\text{opt}}$ assuming a 2D setup [55]. These methods are backscatter-analysis-based and physically realizable; we will briefly review them in Section 3.4.2.

3.3.4 Focusing

By expressing the scattered wavefront $\underline{a}_2^+$ in Region 2 due to an incident wavefront $\underline{a}_1^+$ from Region 1 as

$$
\underline{a}_2^+ = S_{21} \cdot \underline{a}_1^+ = \begin{bmatrix} a_{2,1}^+ & a_{2,2}^+ & \dots & a_{2,K_1}^+ \end{bmatrix}^T,
\tag{3.23}
$$

the electric field at an arbitrary location $\boldsymbol{r}_0$ in Region 2 is a vector field $\boldsymbol{E}_2^+(\boldsymbol{r}_0)$

$$
\begin{aligned}
\boldsymbol{E}_2^+(\boldsymbol{r}_0) &= \begin{bmatrix} E_{2,x}^+(\boldsymbol{r}_0) & E_{2,y}^+(\boldsymbol{r}_0) & E_{2,z}^+(\boldsymbol{r}_0) \end{bmatrix}^T \\
&= \hat{\boldsymbol{p}}_1 a_{2,1}^+ b_1\, e^{-j\boldsymbol{k}_1^+\cdot\boldsymbol{r}_0} + \hat{\boldsymbol{p}}_2 a_{2,2}^+ b_2\, e^{-j\boldsymbol{k}_2^+\cdot\boldsymbol{r}_0} + \dots \\
&\quad \dots + \hat{\boldsymbol{p}}_{K_1} a_{2,K_1}^+ b_{K_1}\, e^{-j\boldsymbol{k}_{K_1}^+\cdot\boldsymbol{r}_0},
\end{aligned}
\tag{3.24}
$$

where $\hat{\boldsymbol{p}}_i = [(\hat{\boldsymbol{p}}_i)_x\ (\hat{\boldsymbol{p}}_i)_y\ (\hat{\boldsymbol{p}}_i)_z]^T$ is the unit polarization vector of the i-th outgoing mode. Let

$$
\begin{aligned}
B(\boldsymbol{r}_0) = \Big[\hat{\boldsymbol{p}}_1 b_1\, e^{-j\boldsymbol{k}_1^+\cdot\boldsymbol{r}_0} \quad \hat{\boldsymbol{p}}_2 b_2\, e^{-j\boldsymbol{k}_2^+\cdot\boldsymbol{r}_0} \quad \dots \\
\dots \quad \hat{\boldsymbol{p}}_{K_1} b_{K_1}\, e^{-j\boldsymbol{k}_{K_1}^+\cdot\boldsymbol{r}_0} \Big],
\end{aligned}
\tag{3.25}
$$

where $B(\boldsymbol{r}_0) \in \mathbb{C}^{3\times K_1}$ is only a function of $\boldsymbol{r}_0$. Thus, Eq. (3.24) can be concisely expressed as

$$
\boldsymbol{E}_2^+(\boldsymbol{r}_0) = B(\boldsymbol{r}_0)\cdot \underline{a}_2^+ = \underbrace{B(\boldsymbol{r}_0)\cdot S_{21}}_{:=C(\boldsymbol{r}_0)}\cdot \underline{a}_1^+,
\tag{3.26}
$$

in which $C(\boldsymbol{r}_0) \in \mathbb{C}^{3\times K_1}$ is still a function of $\boldsymbol{r}_0$. Therefore, the problem of constructing an incident wavefront $\underline{a}_1^+$ that maximizes the intensity of the field at $\boldsymbol{r}_0$ in Region 2 can be expressed as

$$
\begin{aligned}
\underline{a}_{\text{foc}} &= \arg\max_{\underline{a}_1^+} \frac{\parallel \boldsymbol{E}_2^+(\boldsymbol{r}_0) \parallel_2^2}{\parallel \underline{a}_1^+ \parallel_2^2} \\
&= \arg\max_{\|\underline{a}_1^+\|_2=1} \parallel C(\boldsymbol{r}_0)\cdot \underline{a}_1^+ \parallel_2^2.
\end{aligned}
\tag{3.27}
$$

This problem has a closed form solution

$$
\underline{a}_{\text{foc}} = \underline{v}_1^C,
\tag{3.28}
$$

in which $\underline{v}_1^C$ is the primary right singular vector of the matrix $C(\boldsymbol{r}_0)$, and the focusing intensity is the squared spectral norm of $C(\boldsymbol{r}_0)$. If we are only interested in maximizing the intensity of the focusing field in a specific polarization, e.g., in the x, y, or z direction, the corresponding solution can be simplified as

$$\underline{a}_{\mathsf{foc}}^i = \frac{C_{(i,:)}^H(\boldsymbol{r}_0)}{\left\|C_{(i,:)}(\boldsymbol{r}_0)\right\|_2}, \quad i = 1, 2, 3. \tag{3.29}$$

Here, $C_{(i,:)}(\boldsymbol{r}_0)$ denotes to the i-th row of $C(\boldsymbol{r}_0)$, and $i = 1, 2, 3$ corresponds to the specific x, y or z polarization.

If S_{21} is not available, for extracting $\underline{a}_{\mathsf{foc}}$ we revert to the backscatter-analysis-based and physically realizable method [55] in Section 3.4.3.

3.4 Physically Realizable Algorithms for Transmission Maximization and Focusing

3.4.1 Physically Realizable Matrix and Vector Operations

A practical procedure to find the input wavefront that maximizes the transmission power or generates foci through a random medium should be implementable on existing experimental hardware. Moreover, the procedure should work without a priori knowledge of the random medium, though it may require an iterative refinement process. Using the algebraic model of our scattering system, the procedure can be cast an algorithm involving matrix-vector operations, with each matrix-vector operation having a counterpart in the experimental setup. Additionally, in many real-world applications one is incapable of physically accessing Region 2 for observation purposes. Such situations usually occur in bio-imaging and non-intrusive detection. Therefore, ideally, a practical procedure should only rely on backscattered wave information for iterative refinement.

The iterative algorithms we have proposed here for transmission maximization and fo-

cusing are built upon three basic matrix-vector operations:

$$S_{11} \cdot \underline{a}_1^+, \quad \text{TR}(\underline{a}_1^-), \quad \text{and} \quad S_{11}^H \cdot \underline{a}_1^-. \tag{3.30}$$

The first operation, $S_{11} \cdot \underline{a}_1^+$, corresponds to sending an incident wavefront with a normalized modal coefficient vector $\underline{a}_1^+$ and measuring the normalized modal coefficient vector of the backscattered wavefront. In an experimental setup, there exist methods [58] for modulating the amplitude and phase of an input wavefront, in essence creating an arbitrary incident wavefront with a certain accuracy. On the other hand, some digital holography techniques [70] enable us to extract the modal coefficient vector of the backscattered wave by measuring its intensity. Here, we assume that the modal coefficients of a wavefront can be modulated by any desirable amplitude and phase. In addition, we assume that the amplitude and phase of any wavefront can be measured accurately, so that there is no technical restriction impeding the performance of our algorithms.

The second operation $\text{TR}(\underline{a}_1^-)$ represents time-reversing the backscattered wavefront $\underline{a}_1^-$. This operation is the mathematically equivalent to taking the complex conjugate of $\underline{a}_1^-$ as $(\underline{a}_1^-)^*$, then rearranging the order of the entries in $(\underline{a}_1^-)^*$. However, the specific rearrangement depends on how we order the incoming modes as opposed to how we order the outgoing modes in the scattering matrix. In our 3D scattering system, the indices of the incoming mode and the outgoing mode with the exact opposite propagating directions are identical. Thus, rearrangement is not needed here, and therefore,

$$\text{TR}(\underline{a}_1^-) = (\underline{a}_1^-)^*. \tag{3.31}$$

By contrast, in our previous work for 2D [54, 55], the indexing of the outgoing modes followed the reverse order of that for the incoming modes. Therefore, in that context, the rearrangement involved flipping $(\underline{a}_1^-)^*$ upside down, viz. $\text{TR}(\underline{a}_1^-) = F \cdot (\underline{a}_1^-)^*$, in which F was the flipping operator. Physically, this time-reversing operation can be realized via

41

phase-conjugate mirroring (PCM) [71].

The third operation, $S_{11}^H \cdot \underline{a}_1^-$, can be realized by leveraging reciprocity. In a scattering medium that exhibits reciprocity,

$$S_{11}^T = S_{11}. \tag{3.32}$$

Consequently, the matrix-vector operation $S_{11}^H \cdot \underline{a}_1^-$ can be calculated as

$$S_{11}^H \cdot \underline{a}_1^- = \left(S_{11} \cdot (\underline{a}_1^-)^* \right)^* = \mathrm{TR}\left(S_{11} \cdot \mathrm{TR}(\underline{a}_1^-) \right). \tag{3.33}$$

It can be realized in two steps by utilizing the physical procedures of the first and second operations:

1. Capture the backscattered wavefront and obtain its modal coefficient vector $\underline{a}_1^-$; then, time-reverse it and send it back to the scattering system;

2. Capture the resulting backscattered wavefront and obtain its modal coefficient vector $S_{11} \cdot (\underline{a}_1^-)^*$; then, time-reverse it.

In the 2D scenario, Jin et al. developed several iterative, physically realizable algorithms for transmission maximization and focusing [55]. These algorithms generally remain valid in the 3D scenario with minor modifications. In the following sections, we briefly outline these procedures.

Algorithm 3.1 Steepest descent algorithm for finding $\underline{a}_{\text{opt}}$

1: Input: $\underline{a}_{1,(0)}^+ = $ Initial random vector with unit norm
2: Input: $\mu > 0 = $ step size
3: Input: $\epsilon = $ Termination condition
4: $k = 0$
5: **while** $\|S_{11} \cdot \underline{a}_{1,(k)}^+\|_2 > \epsilon$ **do**
6: $\quad \underline{b} = S_{11} \cdot \underline{a}_{1,(k)}^+$
7: $\quad \underline{c} = S_{11}^H \cdot \underline{b}$
8: $\quad \widetilde{\underline{a}}_{1,(k)}^+ = \underline{a}_{1,(k)}^+ - 2\mu \underline{c}$
9: $\quad \underline{a}_{1,(k+1)}^+ = \widetilde{\underline{a}}_{1,(k)}^+ / \|\widetilde{\underline{a}}_{1,(k)}^+\|_2$
10: $\quad k = k + 1$
11: **end while**

3.4.2 Iterative Methods for Transmission Maximization

3.4.2.1 Steepest Descent Method

To minimize the objective function $\|S_{11} \cdot \underline{a}_1^+\|_2^2$, where $\|\underline{a}_1^+\|_2 = 1$, we use the negative gradient of the object function as the search direction to update the candidate solution as

$$
\begin{aligned}
\underline{a}_{1,(k+1)}^+ &= \underline{a}_{1,(k)}^+ - \mu \left. \frac{\partial \|S_{11} \cdot \underline{a}_1^+\|_2^2}{\partial \underline{a}_1^+} \right|_{\underline{a}_1^+ = \underline{a}_{1,(k)}^+} \\
&= \underline{a}_{1,(k)}^+ - 2\mu S_{11}^H \cdot S_{11} \cdot \underline{a}_{1,(k)}^+,
\end{aligned}
\tag{3.34}
$$

in which $\underline{a}_{1,(k)}^+$ stands for the wavefront produced at the k-th iteration, and μ is a positive step size. The procedure proceeds iteratively until the backscattered intensity $\|S_{11} \cdot \underline{a}_{1,(k)}^+\|_2^2$ drops below a preset threshold ϵ, as illustrated in Algorithm 3.1. Step 6 and 7 in Algorithm 3.1 can be physically realized, as discussed in Section 3.4.1. Typically, the steepest descent method leads to a monotonic decrease in the backscattered intensity. The convergence rate of this method depends on the choice of μ, $(0 < \mu < \frac{1}{\hat{\sigma}_1^2 + \hat{\sigma}_M^2} \approx 1)$. Line search is usually employed for finding the best step size μ to obtain the fastest possible convergence.

3.4.2.2 Conjugate Gradient Method

In contrast to the steepest descent method, the conjugate gradient method differs in the choice of μ as

$$\mu_{(k+1)} = \|\underline{r}_{(k)}\|_2^2 / \|S_{11} \cdot \underline{d}_{(k)}\|_2^2, \tag{3.35a}$$

and the search direction as

$$\underline{d}_{(k+1)} = \underline{r}_{(k+1)} + \beta_{(k+1)}\underline{d}_{(k)}, \tag{3.35b}$$

where

$$\beta_{(k+1)} = \|\underline{r}_{(k+1)}\|_2^2 / \|\underline{r}_{(k)}\|_2^2. \tag{3.35c}$$

Here, the residual vector is

$$\begin{aligned} \underline{r}_{(k+1)} &= \underline{r}_{(k)} - \mu_{(k+1)} S_{11}^H \cdot S_{11} \cdot \underline{d}_{(k)} \\ &= -S_{11}^H \cdot S_{11} \cdot \underline{a}_{1,(k+1)}^+. \end{aligned} \tag{3.35d}$$

The iteration terminates when $\|\underline{r}_{(k+1)}\|_2$ is less than a preset threshold ϵ. The above procedure yields Algorithm 3.2. Again, steps 3-4 and steps 8-9 are physically realizable. The advantage of the conjugate gradient algorithm is that only vector $\underline{d}_{(k)}$ is transmitted, and its backscattered $\underline{b} = S_{11} \cdot \underline{d}_{(k)}$ is measured. Because the intensity of the backscattered wavefront b is expected to remain relatively high throughout the iteration, this algorithm permits easier estimation of the backscattered modal coefficient vectors and thereby exhibits lower susceptibility to measurement noise than the steepest descent algorithm. $\underline{a}_{1,(k)}^+$ is *never actually transmitted* until the termination condition $\|\underline{r}_{(k)}\|_2 < \epsilon$ is met.

Algorithm 3.2 Conjugate gradient algorithm for finding $\underline{a}_{\text{opt}}$

1: Input: $\underline{a}^+_{1,(0)} = $ Initial random vector with unit norm
2: Input: $\epsilon = $ Termination condition
3: $\underline{b} = S_{11} \cdot \underline{a}^+_{1,(0)}$
4: $\underline{r}_{(0)} = -S^H_{11} \cdot \underline{b}$
5: $\underline{d}_{(0)} = \underline{r}_{(0)}$
6: $k = 0$
7: **while** $\|\underline{r}_{(k)}\|_2 > \epsilon$ **do**
8: $\quad \underline{b} = S_{11} \cdot \underline{d}_{(k)}$
9: $\quad \underline{d} = S^H_{11} \cdot \underline{b}$
10: $\quad \mu_{(k+1)} = \|\underline{r}_{(k)}\|^2_2 / (\underline{d}^H_{(k)} \cdot \underline{d})$
11: $\quad \underline{a}^+_{1,(k+1)} = \underline{a}^+_{1,(k)} + \mu_{(k+1)}\underline{d}_{(k)}$
12: $\quad \underline{a}^+_{1,(k+1)} = \underline{a}^+_{1,(k+1)} / \|\underline{a}^+_{1,(k+1)}\|_2$
13: $\quad \underline{r}_{(k+1)} = \underline{r}_{(k)} - \mu_{(k+1)}\underline{d}$
14: $\quad \beta_{(k+1)} = \|\underline{r}_{(k+1)}\|^2_2 / \|\underline{r}_{(k)}\|^2_2$
15: $\quad \underline{d}_{(k+1)} = \underline{r}_{(k+1)} + \beta_{(k+1)}\underline{d}_{(k)}$
16: $\quad k = k + 1$
17: **end while**

3.4.3 Lanczos-like Method for Focusing

The Lanczos-like method iteratively constructs a small tridiagonal matrix H with eigenvectors and eigenvalues that approximate the eigenvectors and eigenvalues of $S^H_{11} \cdot S_{11}$, and is detailed in Algorithm 3.3. The eigenvectors of H will rapidly converge to the eigenvec-

Algorithm 3.3 Lanczos-like algorithm for constructing a tridiagonal matrix H, whose eigenvectors and eigenvalues are the approximation of those of $S^H_{11} \cdot S_{11}$.

1: Input: $K = $ Number of eigen-wavefronts needed
2: Input: $\underline{q}_{(1)} = $ Initial random vector with unit norm
3: Input: $s_{(0)} = 0$
4: **for** $k = 1 : K - 1$ **do**
5: $\quad \underline{p}^-_1 = S_{11} \cdot \underline{q}_{(k)}$
6: $\quad \underline{p}^+_1 = (\underline{p}^-_1)^*$
7: $\quad \underline{p}^-_1 = S_{11} \cdot \underline{p}^+_1$
8: $\quad \underline{v} = (\underline{q}^-_1)^*$
9: $\quad H_{k,k} = \underline{q}^H_{(k)} \cdot \underline{v}$
10: $\quad \underline{v} = \underline{v} - H_{k,k}\underline{q}_{(k)} - s_{(k-1)}\underline{q}_{(k-1)}$
11: $\quad H_{k+1,k} = H_{k,k+1} = s_{(k)} = \|\underline{v}\|_2$
12: $\quad \underline{q}_{(k+1)} = \underline{v}/s_{(k)}$
13: **end for**

tors of $S_{11}^H \cdot S_{11}$ associated with the smallest eigenvalues, modeling the few eigen-wavefronts with transmission coefficients near unity. Thus, a small number of iterations $K(K \ll K_1)$ is adequate to extract all the highly transmitted eigen-wavefronts. By obtaining the Ritz eigenvectors

$$\underline{b}_i = Q \cdot \underline{u}_i, \ (i = 1, \ldots, K), \tag{3.36}$$

where $Q = [\underline{q}_{(1)}, \ldots, \underline{q}_{(K)}]$ is formed in Algorithm 3.3 and $\underline{u}_i(i = 1, \ldots, K)$ are the eigenvectors of H, the focused wavefront is approximated by

$$\underline{a}_{\text{foc}} \approx \sum_{i=1}^{K} p_i e^{j\phi_i} \underline{b}_i, \tag{3.37}$$

where $p_i \geq 0$ and $\phi_i \in [-\pi, \pi]$ are the modulating amplitudes and phases that need to be determined. Line search and other methods can be used to find the optimal p_i and ϕ_i for each $\underline{b}_i$. This Lanczos-like method for focusing only requires $O(K)$ measurements, and it is also physically realizable. Specifically, in Algorithm 3.3, Step 7 can be physically realized through backscatter sensing; the complex conjugate operation of Step 6 and 8 can be physically realized through PCM.

3.5   Numerical Simulations

We seek to investigate the scattering behavior of our random media model and test the validity of the transmission maximization and focusing algorithms in 3D. Therefore, we simulate the scattering matrix in Eq. (2.26) via the previously described 3D IE solver. By leveraging the 3D periodic Greens functions and a cascading technique, the method accurately captures interactions between thousands of scatterers. Care is taken to ensure 6-th digit accuracy in the calculation of the entries of the scattering matrix.

3.5.1 Transmission Maximization

We consider a scattering slab with $D_x = D_y = 7.58\lambda$, $\ell = 4.0\lambda$, $K_1 = 354$ and $N_c = 6400$ and compare the intensity of the transmitted field due to a normal and an optimized incident wavefronts. Figs. 3.4a and 3.4b show the electric field intensity on the xy plane behind the slab (in Region 2) produced by the normal and the optimized incident wavefronts, respectively. For the normal incident wavefront, $\tau_{\mathsf{norm}} = 0.0312$ and the maximum of $|E|^2$ is about $0.2\ V^2/m^2$. For the optimized incident wavefront, $\tau_{\mathsf{opt}} = 0.996$ and the maximum of $|E|^2$ is about $10.0\ V^2/m^2$, an more than 30-fold increase compared to the normal incident case. Figure 3.5 shows the magnitude and phase of the transmission-optimized wavefront.

Figure 3.6 displays the convergence history of the steepest descent ($\mu = 0.5$) and the conjugate gradient algorithms for transmission maximization, working on the previous scattering system that has $D_x = D_y = 7.58\lambda$, $l = 4.0\lambda$, $M = 354$ and $N_c = 6400$. Both algorithms yield $\tau_{\mathsf{opt}} = 0.994$ after 10 iterations. To investigate the impact of different values of μ on the convergence of the steepest descent algorithm, the transmitted power after the 10-th iteration for different choices of μ is computed and plot in Figure 3.7. This study clearly shows that there is a broad range of μ that yield fast convergence of the steepest descent algorithm; $0.45 \leq \mu \leq 0.8$ yields the fastest convergence rate. Practically, the conjugate gradient algorithm is preferred over the steepest descent algorithm since it requires simpler measurements and no auxiliary parameters need to be set. Next, we consider a setting in which a subset of the propagating modes are controlled. The controlled modes are those with the smallest plane angles to the normal direction (the smallest θ in the spherical coordinate). The setting for the scattering system is the same as previous tests. We consider three different approaches for the measurement: 1) measuring the transmitted field with modes having the same propagating directions as the controlled modes, 2) measuring the backscattered field with modes having the opposite propagating directions

$|E|^2$ at (x,y,2λ) plane behind the slab due to normal incident wavefront
periodic cell = 7.5804$\lambda \times$7.5804λ, 354 modes, 6400 layers
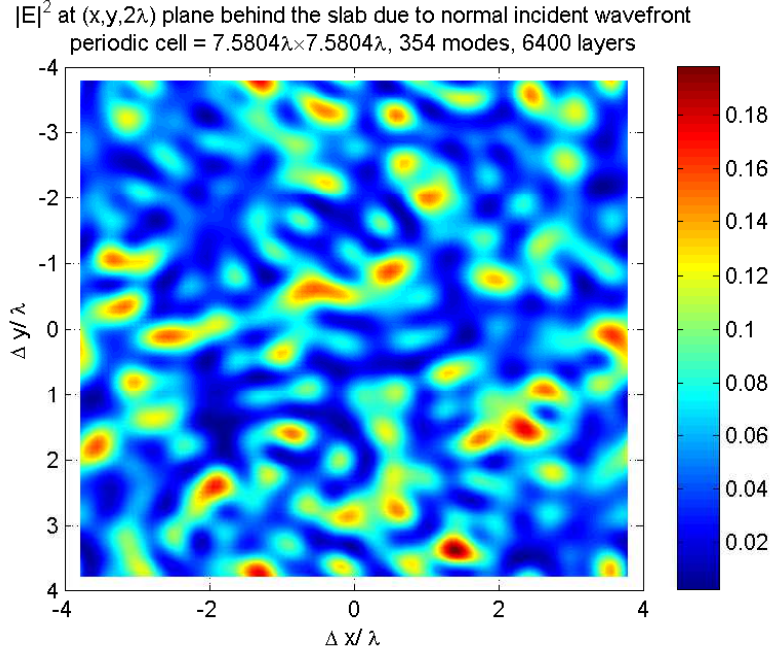
(a) Electric filed produced by the normal incident wavefront.

$|E|^2$ at (x,y,2λ) plane behind the slab due to optimized incident wavefront
periodic cell = 7.5804$\lambda \times$7.5804λ, 354 modes, 6400 layers
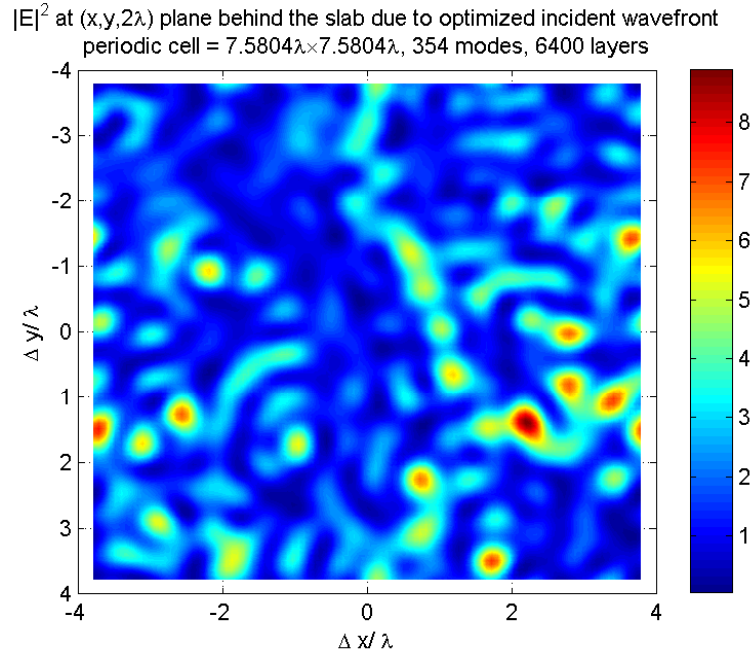
(b) Electric filed produced by the transmission-optimized incident wavefront.

Figure 3.4: E field intensity of the transmitted wave behind the slab (in Region 2) by 2λ due to (a) the normal incident and (b) the transmission-optimized incident wavefront for a slab with $D_x = D_y = 7.58\lambda$, $l = 4.0\lambda$, $K_1 = 354$ and $N_c = 6400$.
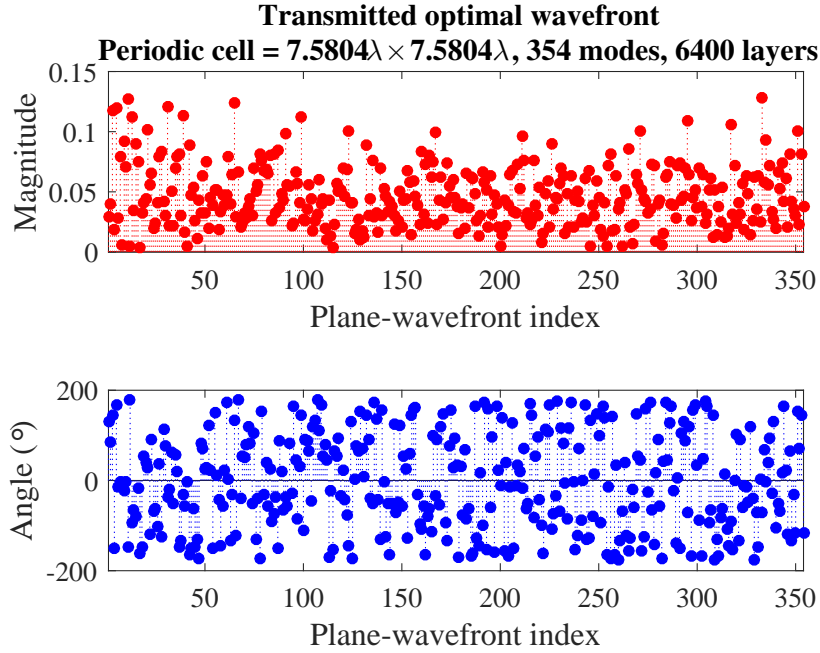
Figure 3.5: The magnitude and phase combinations of the optimal wavefront corresponding to Fig 3.4b.
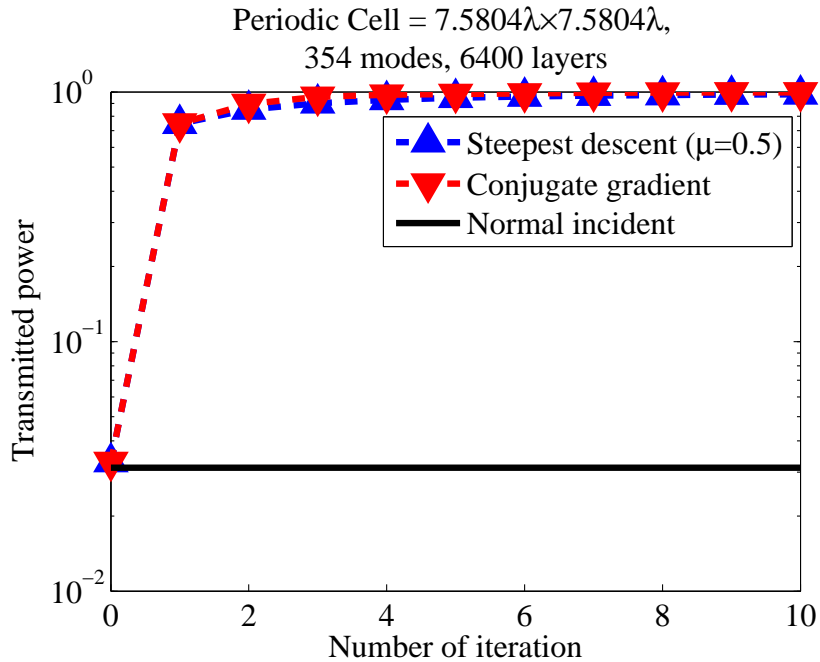
Figure 3.6: The convergence history of the steepest descent ($\mu = 0.5$) and the conjugate gradient algorithms for transmission maximization.

as the controlled modes, and 3) measuring the backscattered field with all modes. Figure 3.8 shows the realized gain ($= \tau_{\text{opt}}/\tau_{\text{norm}}$) (relative to a normal incident wavefront) for the
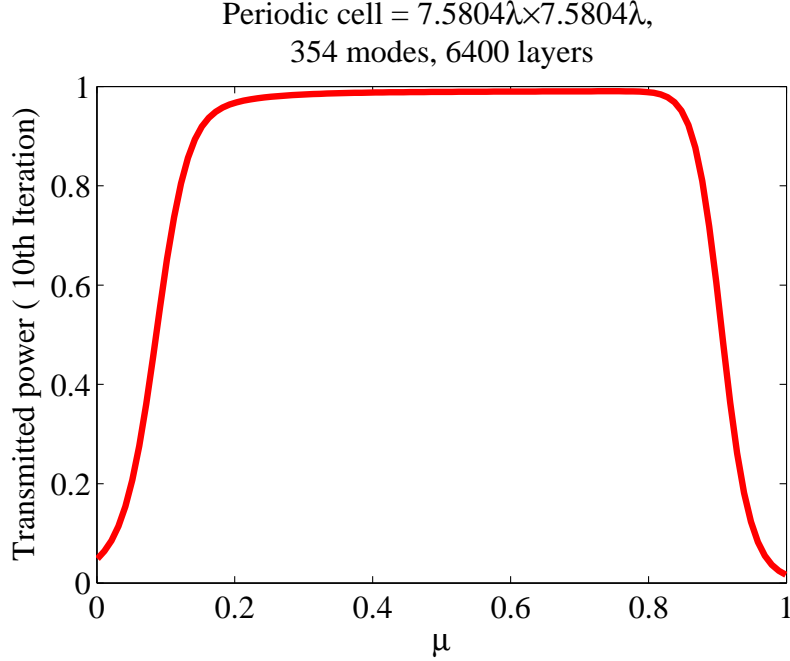
Figure 3.7: The transmitted power after the 10-th iteration versus different choice of μ for the same setting as in Figure 3.4.

three different approaches. The results indicate that if all modes in the backscattered field can be measured, we can significantly increase the transmission rate by controlling only a portion of the modes. By contrast, only attempting to minimize the field intensity due to partial modes in the backscattered directions could actually increase backscattering through modes in the unmeasured backscattered directions, but the forward transmission.

3.5.2 Focusing

For the focusing problem, we consider a focus target at $(0, 0, 2.0\lambda)$ behind the slab (in Region 2). We excite the slab with the naive focusing wavefront, which would focus the field if there were no slab present as well as the optimized focusing wavefront, to maximize the field intensity at the target point described in Eq. (3.29). Figure 3.9a and Figure 3.9b illustrate the intensity due the two incident wavefronts in the $(x, y, 2.0\lambda)$ plane, respectively. The optimized wavefront successfully creates a focus spot at the target, whereas the naive focusing wavefront does not. We decompose the optimized focusing wavefront in terms of
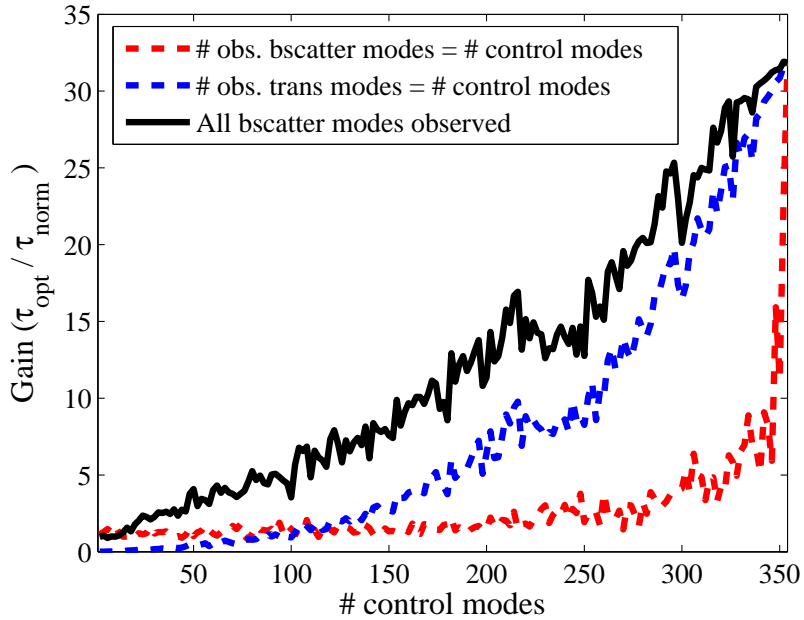
Figure 3.8: Gain ($= \tau_{\mathsf{opt}}/\tau_{\mathsf{norm}}$) achieved by controlled modes for the three different approaches.

plane waves (propagating modes), and Figure 3.10a shows that the magnitudes of the coefficients exhibits no obvious pattern. However, the magnitudes of their coefficients exhibit a clear sparse pattern following the decomposition of the optimized focusing wavefront in terms of eigen-wavefronts, namely the right singular vectors of the S_{11} matrix, as shown in Figure 3.10b. Accordingly, we use the Lanczos-like algorithm described in Section 3.4.3, which utilizes this sparse property of the eigen-wavefronts to construct the optimal focusing wavefront. Figure 3.11 shows the focusing intensity achieved as a function of the number of measurements. These results clearly demonstrate that with only a few measurements ($K \ll K_1$), the Lanczos algorithm can rapidly find a near-optimum focusing wavefront reaching approximately 90% of the optimal intensity.

3.6 Conclusion

We test our 3D random media model by investigating its transmission coefficient distribution over 10,000 random realizations. The transmission coefficient distribution fits the
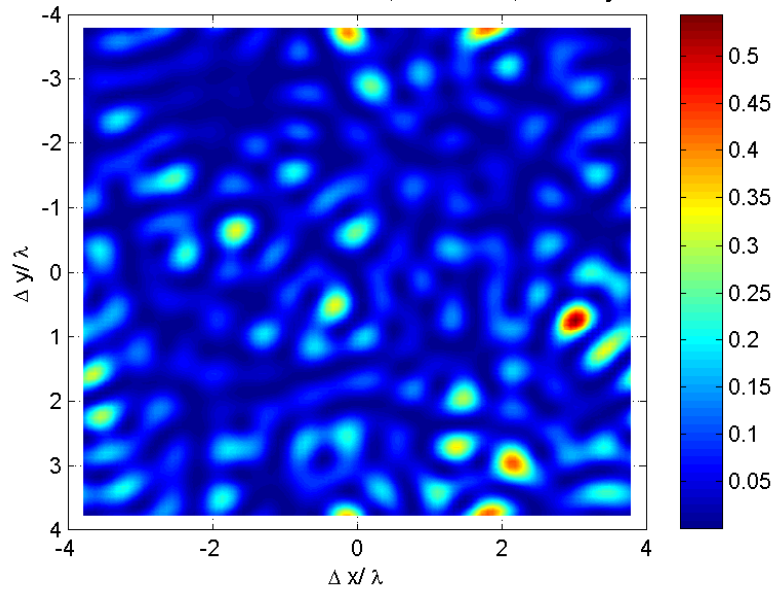
(a) Electric field intensity due to a naive focusing wavefront.
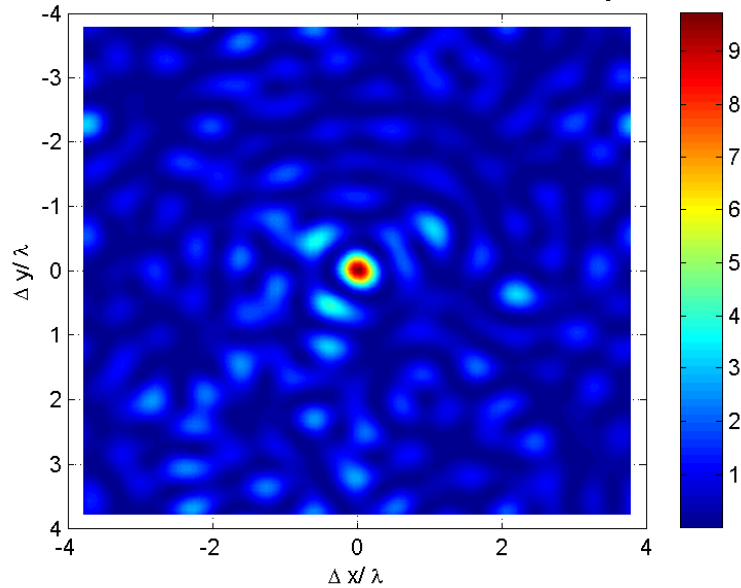
(b) Electric field intensity due to an optimized focusing wavefront.

Figure 3.9: Electric field intensity at $(x, y, 2\lambda)$ plane behind the slab (in region 2) due to (a) a naive focusing wavefront and (b) an optimized focusing wavefront for a target at $(0, 0, 2\lambda)$ behind the slab (in region 2). The scattering system is the same as that in Figure 3.4. The optimized focusing wavefront forms a sharp spot at the target point.

Decomposition of Optmized Wavefront for Focusing at (0,0,2λ)
354 modes, 6400 Layers
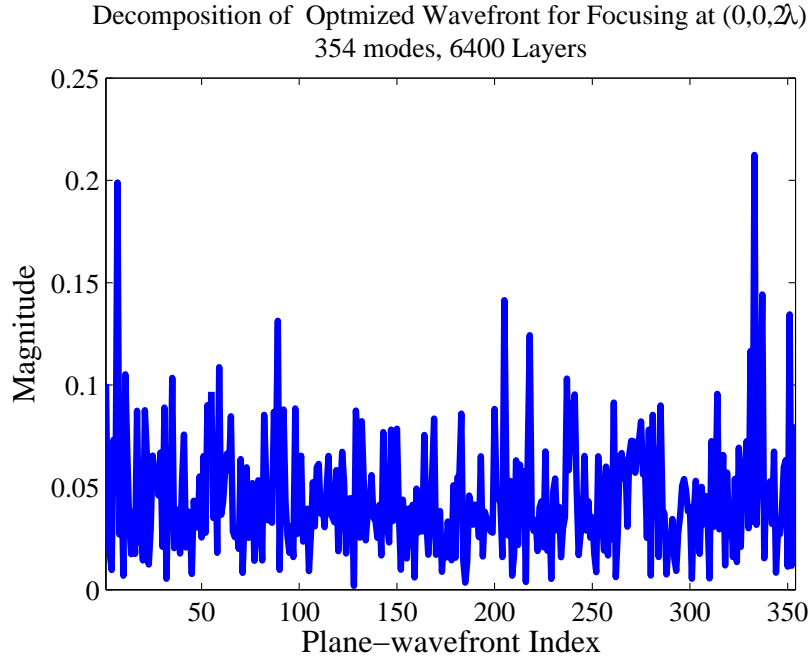
(a) The magnitude of the coefficients for plane-wavefront decomposition.

Decomposition of Optmized Wavefront for Focusing at (0,0,2λ)
354 modes, 6400 Layers
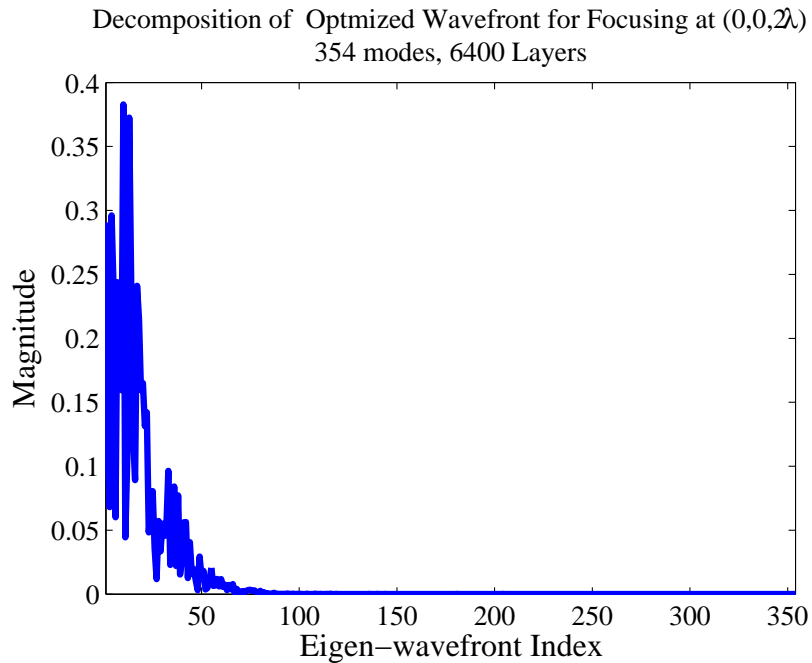
(b) The magnitude of the coefficients for eigen-wavefront decomposition.

Figure 3.10: Two ways to decompose the optimized focusing wavefront, (a) in terms of plane waves (propagating modes) and (b) in terms of eigen-wavefronts. The magnitude of the coefficients in (b) exhibit a clear sparse pattern.
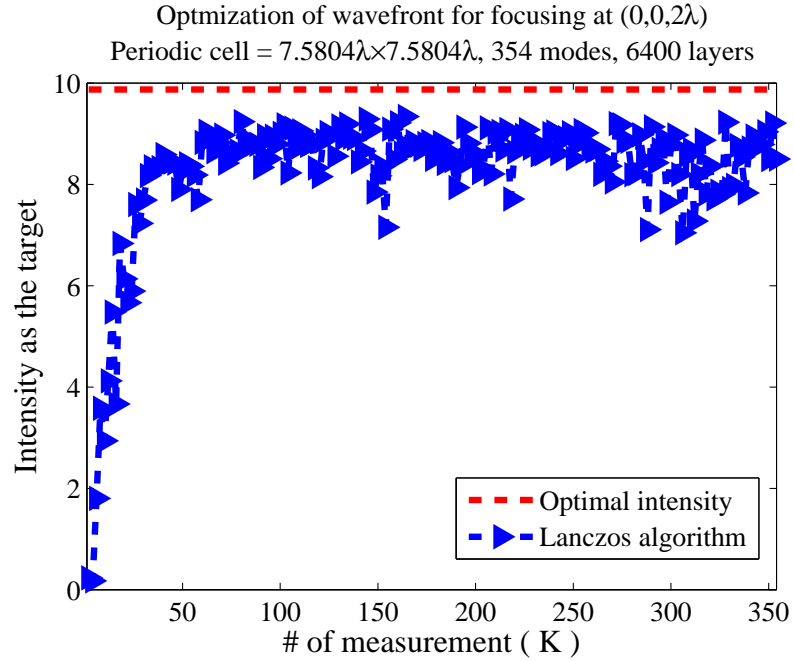
Figure 3.11: The focusing intensity versus the number of measurements in the Lanczos-like algorithm for constructing a near-optimum focusing wavefront.

theoretical DMPK distribution perfectly. In addition, numerical simulations demonstrate that several iterative, physically realizable algorithms for transmission maximization and focusing also work well for 3D random media models.

CHAPTER 4

Advanced Multi-Foci Focusing in 3D Random Media

4.1 Introduction

The need to focus electromagnetic fields passing through random media arises in applications ranging from bio-imaging to non-destructive inspection and electromagnetic hyperthermia treatment, to name but a few. Unfortunately, conventional focusing techniques are very inefficient when used for highly diffusive media containing scatterers that significantly alter the paths traveled by the fields, either causing speckle patterns in the exit aperture or preventing penetration altogether. In Section 3.3.2, we argued that the wavefronts of fields impinging on lossless (non-absorbing) dilute random media model can be shaped to optimally couple into perfectly transmitting wavefronts, the so-called "open channels", and create focused fields upon exit. In Sections 3.4.3 and 3.5.2, we demonstrated the ability to focus fields passing through our 3D media model by using a Lanczos-like algorithm. Unfortunately, the scheme calls for full amplitude and phase control of the incident wave. In many practical situations, only the phase of the field can be efficiently controlled; this is particular true in the optical regime where control often is achieved using phase-only spatial light modulators (SLMs). Furthermore, the scheme is limited in the type and number of foci it is capable of producing.

In this chapter, we present a new family of highly efficient focusing schemes capable of

creating multiple foci under a variety of conditions of practical interest. Our schemes apply to scenarios that allow for phase-only as well as full phase-amplitude modulation of the incident wavefront. They also address problems requiring contrast and non-contrast as well as maximal-total-intensity and even-intensity (fair) focusing. The proposed schemes comprehensively tackle the wavefront shaping problem by leveraging eigen-decompositions, convex optimization, and bisection search algorithms. Specifically, eigen-decompositions are used to handle simple focusing problems when full phase-amplitude modulation is achievable, while convex optimization and bisection search are invoked for focusing problems lacking closed form solutions. We demonstrate the new focusing schemes capabilities' and efficiency by applying them to our 3D random media model.

4.2 Multi-Foci Focusing without Contrast

Focusing without contrast (non-contrast focusing) suggests that we only intend to maximize the field intensity on the candidate foci. The fields at other locations beyond the foci are not considered. This type of focusing may produce extra foci in addition to the specified ones; usually, these additional foci are undesired. On the other hand, focusing with contrast (contrast focusing) implies that in addition to maximizing the field intensity on the candidate foci, we seek to also minimize the field intensity on certain non-foci locations. These non-foci locations requiring minimal disturbance from the (electric) field are needed for particular engineering applications. Focusing with contrast therefore implies that a high ratio of the field intensity at desired foci over the field intensity on specific non-foci locations is desired. We elaborate on the problem of focusing with contrast in Section 4.3.

4.2.1 Maximal-Total-Intensity Focusing

The maximal-total-intensity focusing implies that the sum of the field intensities at all desired foci is maximized. Even-intensity (fair) focusing on the other hand seeks fields

roughly equal intensity at all foci, while attempting to maximize the total intensity. We discuss maximal-total-intensity and even-intensity (fair) focusing for non-contrast and contrast focusing separately.

4.2.1.1 Solution for Phase-Amplitude Modulation

Here, we start from the single-focus problem of Section 3.3.4. The electric field at $\boldsymbol{r}_0$ behind the slab (in region 2) due to an incident wave from Region 1 is

$$\boldsymbol{E}_2^+(\boldsymbol{r}_0) = C(\boldsymbol{r}_0) \cdot \underline{a}_1^+, \tag{4.1}$$

where $C(\boldsymbol{r}_0) \in \mathbb{C}^{3 \times K_1}$ is defined in Eq. (3.26). Suppose we have q candidate foci at $\{\boldsymbol{r}_1, \boldsymbol{r}_2, \ldots, \boldsymbol{r}_q\}$ in Region 2; then, their electric fields can be expressed as

$$\begin{bmatrix} \boldsymbol{E}_2^+(\boldsymbol{r}_1) \\ \boldsymbol{E}_2^+(\boldsymbol{r}_2) \\ \vdots \\ \boldsymbol{E}_2^+(\boldsymbol{r}_q) \end{bmatrix} = \underbrace{\begin{bmatrix} C(\boldsymbol{r}_1) \\ C(\boldsymbol{r}_2) \\ \vdots \\ C(\boldsymbol{r}_q) \end{bmatrix}}_{:=Q} \cdot \underline{a}_1^+, \tag{4.2}$$

in which $Q \in \mathbb{C}^{3q \times K_1}$ and the left hand side vector contains the complex amplitudes of the electric fields along the x, y and z directions at q locations. If the electric fields along a particular direction (x, y or z) are needed, we can extract them as

$$\begin{bmatrix} \boldsymbol{E}_{2,i}^+(\boldsymbol{r}_1) \\ \boldsymbol{E}_{2,i}^+(\boldsymbol{r}_2) \\ \vdots \\ \boldsymbol{E}_{2,i}^+(\boldsymbol{r}_q) \end{bmatrix} = \underbrace{\begin{bmatrix} C_{i,:}(\boldsymbol{r}_1) \\ C_{i,:}(\boldsymbol{r}_2) \\ \vdots \\ C_{i,:}(\boldsymbol{r}_q) \end{bmatrix}}_{:=Q^{\{i=1,2,3 \longrightarrow x,y,z\}}} \cdot \underline{a}_1^+, \quad i = 1, 2, 3, \tag{4.3}$$

in which $Q^{\{x,y,\text{ or } z\}} \in \mathbb{C}^{q \times K_1}$. The corresponding optimization problem to maximize the total electric field intensity among these q locations can be expressed as follows:

$$
\begin{aligned}
\underline{a}_{\text{mf}} &= \arg\max_{\|\underline{a}_1^+\|_2=1} \sum_{i=1}^{q} \| C(\boldsymbol{r}_i) \cdot \underline{a}_1^+ \|_2^2 \\
&= \arg\max_{\|\underline{a}_1^+\|_2=1} \| Q \cdot \underline{a}_1^+ \|_2^2
\end{aligned}
\tag{4.4}
$$

Clearly, the solution to Eq. (4.4) is the first right singular vector of matrix Q corresponding to its largest singular value. Specifically, for the singular value decomposition $Q = \sum_{i=1} \sigma_i \underline{u}_i \cdot \underline{v}_i^H$, we have

$$
\underline{a}_{\text{mf}} = \underline{v}_1.
\tag{4.5}
$$

If the transmission matrix is measured using the technique described in [44–47], we can easily obtain $\underline{v}_1$. In addition, we can physically synthesize the wavefront represented by $\underline{v}_1$ when we have a light modulator capable of controlling both amplitude and phase. Using a twisted nematic LCD combined with a spatial filter, the innovative method developed by van Putten et al. in [58] for full spatial phase and amplitude control provides such an option.

If we ignore the effect of the random medium, viz., treat the slab as a homogeneous medium with a dielectric constant equal to that of the background, then the corresponding focusing problem is

$$
\begin{aligned}
\underline{a}_{\text{nmf}} &= \arg\max_{\|\underline{a}_1^+\|_2=1} \sum_{i=1}^{q} \| B(\boldsymbol{r}_i) \cdot \underline{a}_1^+ \|_2^2 \\
&= \arg\max_{\|\underline{a}_1^+\|_2=1} \| O \cdot \underline{a}_1^+ \|_2^2,
\end{aligned}
\tag{4.6}
$$

in which $B(\boldsymbol{r}) \in \mathbb{C}^{3 \times K_1}$ is defined in Eq. (3.25) and

$$
O = \begin{bmatrix} B(\boldsymbol{r}_1) \\ B(\boldsymbol{r}_2) \\ \vdots \\ B(\boldsymbol{r}_q) \end{bmatrix}.
\tag{4.7}
$$

The solution of Eq. (4.6) is the first right singular vector of matrix O. Since $\underline{a}_{\text{nmf}}$ corresponds to the solution for a transparent slab that does not scatter, we refer to it as the naive focusing wavefront.

4.2.1.2 Solution for Phase-Only Modulation

Although the full spatial phase and amplitude control is possible, the most widely available light modulators only allow for phase control. Not surprisingly, there is a great interest in methods for focusing wavefronts via phase-only modulation. While focusing using phase-only modulators produces results that are suboptimal compared to those produced by full phase-amplitude modulation schemes, our phase-only modulating methods constructing the desired wavefronts with more than 70% of the focusing intensity of the optimum ones.

First, we define

$$
\underline{/a_1^+} = \begin{bmatrix} \underline{/a_1} & \underline{/a_2} & \cdots & \underline{/a_{K_1}} \end{bmatrix}^T,
\tag{4.8}
$$

in which $\underline{/a_i}$ is the phase angle of a_i, and

$$
a_i = |a_i|\, e^{j\underline{/a_i}}, \quad i = 1, \ldots, K_1.
\tag{4.9}
$$

Let $P_1^{K_1}$ denote the set of vectors such that $\forall\, \underline{a}_1^+ = [a_1 \ a_2 \ \cdots \ a_{K_1}]^T \in P_1^{K_1}$, we have

$\|\underline{a}_1^+\|_2 = 1$, and $|a_i| \equiv 1/\sqrt{K_1}$, $(i = 1, \ldots, K_1)$. Apparently, for arbitrary $\underline{a}_1^+$

$$\frac{\angle \underline{a}_1^+}{\sqrt{K_1}} \in P_1^{K_1}. \tag{4.10}$$

Alternatively, for arbitrary $\underline{\theta} = [\theta_1 \quad \theta_2 \quad \ldots \quad \theta_{K_1}]^T \in \mathbb{R}^{K_1}$, define

$$\underline{p}(\underline{\theta}) = \frac{1}{\sqrt{K_1}} \begin{bmatrix} e^{j\theta_1} & e^{j\theta_2} & \ldots & e^{j\theta_{K_1}} \end{bmatrix}^T, \tag{4.11}$$

then, $\underline{p}(\underline{\theta}) \in P_1^{K_1}$. Thus, the corresponding optimization problem leading to maximization of the total electric field intensity at these q locations via phase-only modulation is

$$\underline{a}_{\mathsf{mf},\mathsf{phs}} = \arg\max_{\underline{a}_1^+ \in P_1^{K_1}} \| \, Q \cdot \underline{a}_1^+ \, \|_2^2. \tag{4.12}$$

Unfortunately, Eq. (4.12) does not have a close form solution. In addition, its feasible set is non-convex, because for $\underline{\theta}_1 \neq \underline{\theta}_2$ and $\alpha \in [0, 1]$, $\alpha \, \underline{p}(\underline{\theta}_1) + (1 - \alpha)\underline{p}(\underline{\theta}_2) \notin P_1^{K_1}$. As a result, we can neither solve it precisely nor solve it via the direct use of sophisticated convex optimization scheme [72]. A naively approximate solution to Eq. (4.12) is the feasible set is

$$\underline{a}_{\mathsf{mf},\mathsf{phs}} = \underline{p}(\angle \underline{a}_{\mathsf{mf}}). \tag{4.13}$$

It is usually called the spherical relaxation [73]. However, this approximation is "loose". Here, we consider a "tighter" approximation provided by semidefinite programming (SDP) [74].

We begin by examining the objective function on the right hand side of Eq. (4.12). Note that

$$\begin{aligned} \left\| Q \cdot \underline{a}_1^+ \right\|_2^2 &= \left((\underline{a}_1^+)^H \cdot Q^H \cdot Q \cdot \underline{a}_1^+ \right) \\ &= \mathrm{Tr}\left(Q^H \cdot Q \cdot \underline{a}_1^+ \cdot (\underline{a}_1^+)^H \right), \end{aligned} \tag{4.14}$$

where $\text{Tr}(*)$ denotes the trace of its matrix argument. Let us define a new matrix variable $A = \underline{a}_1^+ \cdot (\underline{a}_1^+)^H$. Since $\underline{a}_1^+ \in P_1^{K_1}$, A is a rank-one, Hermitian, positive semidefinite matrix with $A_{ii} \equiv 1/K_1$, $(i = 1, \ldots, K_1)$. Consequently, starting from Eq. (4.14), we can formulate an alternative optimization problem:

$$A_{\text{opt}} = \underset{A \in \mathbb{C}^{K_1 \times K_1}}{\arg\max} \ \text{Tr}\left(Q \cdot Q^H \cdot A\right)$$
$$\text{subject to } A = A^H, A \succeq 0, \tag{4.15}$$
$$\text{rank}(A) = 1,$$
$$\text{and } A_{ii} = 1/K_1 \text{ for } i = 1, \ldots K_1,$$

where the constraints $A = A^H$ and $A \succeq 0$ indicate that A is a Hermitian, positive semidefinite matrix. If we can solve Eq. (4.15) exactly, then by construction, we must have $A_{\text{opt}} = \underline{a}_{\text{mf,phs}} \cdot \underline{a}_{\text{mf,phs}}^H$ with $\underline{a}_{\text{mf,phs}} \in P_1^{K_1}$. As a result, we would have solved Eq. (4.12) exactly. However, the set of rank one matrices is a non-convex set, since the sum of two rank one matrices is not necessarily rank one. Thus, the rank constraint in Eq. (4.15) makes the problem difficult to solve [73], even though the objective function and other constraints are convex for A.

By eliminating the cumbersome rank-one constraint in Eq. (4.15), we obtain a relaxed optimization problem, which is the so-called SDP problem [74]

$$A_{\text{sdp}} = \underset{A \in \mathbb{C}^{K_1 \times K_1}}{\arg\max} \ \text{Tr}\left(Q^H \cdot Q \cdot A\right)$$
$$\text{subject to } A = A^H, A \succeq 0, \tag{4.16}$$
$$\text{and } A_{ii} = 1/K_1 \text{ for } i = 1, \ldots K_1.$$

This problem can be solved efficiently in polynomial-time [73] using off-the-shelf algorithms, such as CVX [75] or SDPT3 [76]. See Appendix A.1 for details.

If the solution A_{sdp} turns out to be a rank-one matrix, the we have $A_{\text{sdp}} = A_{\text{opt}}$, and

we have solved the original problem in Eq. (4.12). However, Asdp is typically not of rank one. Therefore, we propose the following procedure to obtain approximate solutions to the unrelaxed problem in Eq. (4.15).

Since A_{sdp} is Hermitian and positive semidefinite, it has an eigen-decomposition

$$A_{\mathsf{sdp}} = \sum_{i=1}^{K_1} \lambda_i \, \underline{u}_{i,\mathsf{sdp}} \cdot \underline{u}_{i,\mathsf{sdp}}^H, \tag{4.17}$$

with $\lambda_1 \geq \ldots \lambda_{K_1} \geq 0$. Practically, only the first few eigenvalues $\lambda_1, \lambda_2, \ldots$ are significant. We particularly choose the first eigenvector $\underline{u}_{1,\mathsf{sdp}}$ to construct an approximate solution:

$$\underline{a}_{\mathsf{mf,phs,sdp}} = \underline{p}\left(\angle \underline{u}_{1,\mathsf{sdp}}\right). \tag{4.18}$$

Because the SDP relaxation is a tighter relaxation than the spherical one [73], we expect $\underline{a}_{\mathsf{mf,phs,sdp}}$ to result in higher focus intensity than $\underline{a}_{\mathsf{mf,phs}}$. Note that $\underline{a}_{\mathsf{mf,phs,sdp}}$, given by Eq. (4.18) is an approximation to the solution of Eq. (4.15); thus, it is not guaranteed to be the phase-only modulated wavefront that yields the highest focus intensity. However, it does provide a lower bound on the focus intensity that can be achieved. On the other hand, the deterministic approximation $\underline{a}_{\mathsf{mf,phs,sdp}}$ to the solution of Eq. (4.15) is by no means the closest approximation. Therefore, we can alternatively consider a randomized approximation $\underline{a}_{\mathsf{mf,phs,sdp}}^{\mathsf{rand}}$ produced from A_{sdp} as

$$\underline{a}_{\mathsf{mf,phs,sdp}}^{\mathsf{rand}} = \underline{p}\left(\angle \left(\sum_{i=1}^{K_1} \sqrt{\lambda_i}\, \underline{u}_{i,\mathsf{sdp}} \cdot \underline{u}_{i,\mathsf{sdp}}^H\right) \cdot z\right), \tag{4.19}$$

where $z = z_R + \sqrt{-1}\, z_I$. $z_R, z_I \in \mathbb{R}^{K_1}$ are i.i.d. random vectors that are normally distributed with a zero mean and covariance matrix $I^{K_1 \times K_1}/2$.

4.2.2 Even-Intensity (Fair) Focusing

4.2.2.1 Solution for Phase-Amplitude Modulation

For the multi-foci focusing problem in Eq. (4.4), we aim to maximize the sum of the field intensity over all foci. Sometimes, this process is not desirable because certain foci may turn out weak even when the total brightness of all foci achieves a maximum. Therefore, a more realistic objective function, which imposes a fair focusing constraint on each individual focus spot, can be stated as

$$
\underline{a}_{\mathsf{fmf}} = \arg\max_{\|\underline{a}_1^+\|_2 = 1} \ \min_{i=1,\ldots,q} \left(\| \underbrace{C(\boldsymbol{r}_i)}_{:=Q_i} \cdot \underline{a}_1^+ \|_2^2 \right). \tag{4.20}
$$

Unfortunately, Eq. (4.20) does not have a close form solution. A simple and practical approach to finding an approximate solution to Eq. (4.20) is via multiple updates (MLU). The essence of the proposed MLU scheme lies in updating a wavefront vector iteratively as

$$
(\underline{a}_1^+)^{(k+1)} = \text{normalize}\left(\sum_{i=1}^q \frac{Q_i^H \cdot Q_i \cdot (\underline{a}_1^+)^{(k)}}{\left\| Q_i \cdot (\underline{a}_1^+)^{(k)} \right\|_2} \right). \tag{4.21}
$$

The initial $(\underline{a}_1^+)^{(0)}$ could be a random wavefront, or a candidate solution produced by other methods. Although the MLU cannot guarantee an optimum solution, the outcome is often highly satisfactory in practice. A more sophisticated optimization technique is needed if the MLU fails to provide satisfactory solutions. To handle such situations, we propose a bisection search scheme in tandem with the SDP solver, as described below.

Following the same rationale for reforming the norm maximization problem in Eq. (4.12) to the trace maximization problem in Eq. (4.14), we can reform the fair focusing

problem in Eq. (4.20) as

$$A_{\text{opt}} = \underset{A \in \mathbb{C}^{K_1 \times K_1}}{\arg\max} \ \underset{i=1,\ldots,q}{\min} \left(\text{Tr} \left(Q_i^H \cdot Q_i \cdot A \right) \right)$$

$$\text{subject to } A = A^H, A \succeq 0,$$

$$\text{rank}(A) = 1,$$

$$\text{and } \text{Tr}(A) = 1,$$

(4.22)

in which $\text{Tr}(A) = 1$ indicates the power constraint $\|\underline{a}_1^+\|_2^2 = 1$. By introducing an auxiliary variable η, Eq. (4.22) can be further reformulated as

$$A_{\text{opt}} = \underset{A \in \mathbb{C}^{K_1 \times K_1}}{\arg\max} \ \eta$$

$$\text{subject to } \underset{i=1,\ldots,q}{\min} \left(\text{Tr} \left(Q_i^H \cdot Q_i \cdot A \right) \right) \geq \eta$$

$$A = A^H, A \succeq 0,$$

$$\text{rank}(A) = 1,$$

$$\text{and } \text{Tr}(A) = 1.$$

(4.23)

The variables we seek to optimize here are η and A. However, we are only interested in A when the value of η is maximized. By eliminating the rank-one constraint on A, we convert the optimization problem into a set of convex feasibility problems, that can be solved efficiently using SDP algorithms. A bisection search algorithm is adopted to find the η. This technique is widely used in fractional programming [72, 77].

Let η_{opt} denote the unknown optimal value of the objective function. Given $\eta^* \in \mathbb{R}$, if

the convex problem

$$
\text{find } A \in \mathbb{C}^{K_1 \times K_1}
$$

$$
\text{subject to } \min_{i,\dots,q} \left(\text{Tr}\left(Q_i^H \cdot Q_i \cdot A\right) \right) \geq \eta^*
$$

$$
A = A^H, A \succeq 0,
$$

$$
\text{and } \text{Tr}(A) = 1,
$$

(4.24)

is feasible, then we conclude that $\eta_{\text{opt}} \geq \eta^*$. Otherwise, we conclude that $\eta_{\text{opt}} < \eta^*$. Using this method we establish whether or not the optimal value η_{opt} is smaller (or larger) than a given value η^*. This observation motivates us to use a bisection search to find the η_{opt} iteratively, and to refine the solution A_{opt}. In each iteration of the bisection search, we solve a convex feasibility problem. Algorithm 4.1 demonstrates how this process works. Here, to obtain the phase-amplitude solution, Eq. (4.24) is the feasibility problem needed

---

Algorithm 4.1 Bisection search for finding η_{opt} and the corresponding A_{opt}

1: Input: $\eta_L = $ the lower bound of η
2: Input: $\eta_U = $ the upper bound of η
3: Input: $\sigma = $ the tolerance for accuracy
4: $k = 0$
5: **while** $\eta_U - \eta_L > \sigma$ **do**
6:    $k = k + 1$
7:    $\eta^* = (\eta_U + \eta_L)/2$
8:    solving the feasibility problem in Eq. (4. XX)
9:    **if** *feasible* **then**
10:       $\eta_U = \eta^*$
11:    **else**
12:       $\eta_L = \eta^*$
13:    **end if**
14: **end while**
15: Output: A_{opt}, η^*

---

in line 8 of Algorithm 4.1. The initial input η_L and η_U for the fair focusing problem can be estimated by

$$
\eta_U = \min_{i=1,\dots,q} \left(\sigma_{\max}(Q_i) \right),
$$

(4.25)

$$\eta_L = \max_{i=1,\ldots,q} \left(\sigma_{\min}(Q_i) \right), \tag{4.26}$$

in which $\sigma_{\max}(Q_i)$ and $\sigma_{\min}(Q_i)$ represent the largest and smallest singular values of Q_i, respectively.

After A_{sdp} is found, we proceed with the eigen-decomposition $A_{\mathsf{sdp}} = \sum_{i=1}^{K_1} \lambda_i \underline{u}_{i,\mathsf{sdp}} \cdot \underline{u}_{i,\mathsf{sdp}}^H$ with the eigenvalues arranged as $\lambda_1 \geq \ldots \lambda_{K_1} \geq 0$. We can approximate the optimal solution for this fair focusing problem as

$$\underline{a}_{\mathsf{fmf,sdp}} = \underline{u}_{1,\mathsf{sdp}}. \tag{4.27}$$

4.2.2.2 Solution for Phase-Only Modulation

Replacing the feasible set $\left\| \underline{a}_1^+ \right\|_2 = 1$ in Eq. (4.20) with $\underline{a}_1^+ \in P_1^{K_1}$, we obtain the optimization problem for phase-only modulation:

$$\underline{a}_{\mathsf{fmf,phs}} = \arg\max_{\underline{a}_1^+ \in P_1^{K_1}} \min_{i=1,\ldots,q} \left(\left\| Q_i \cdot \underline{a}_1^+ \right\|_2^2 \right). \tag{4.28}$$

There are two methods for obtaining an approximate solution to the above problem. The first method involves adding the spherical relaxation in the MLU iteration, as

$$(\underline{a}_1^+)^{(k+1)} = \underline{p}\left(\Big/ \left(\sum_{i=1}^q \frac{Q_i \cdot Q_i^H \cdot (\underline{a}_1^+)^{(k)}}{\left\| Q_i^H \cdot (\underline{a}_1^+)^{(k)} \right\|_2} \right) \right), \tag{4.29}$$

If the iteration terminates at step K, the final solution is denoted by $\underline{a}_{\mathsf{fmf,phs,MLU}} = (\underline{a}_1^+)^{(K)}$.

Alternatively, we could generate a solution by formally solving an optimization problem very similar to that for the phase-amplitude solution in Section 4.2.2.1, viz. the bisection search in conjunction with the SDP solver. More specifically, the bisection search framework elaborated upon in Algorithm 4.1 remains valid here for obtaining a phase-only

solution. The feasibility problem needed in line 8 of Algorithm 4.1 is

$$\text{find } A \in \mathbb{C}^{K_1 \times K_1}$$

$$\text{subject to } \min_{i,\ldots,q} \left(\text{Tr} \left(Q_i^H \cdot Q_i \cdot A \right) \right) \geq \eta^* \tag{4.30}$$

$$A = A^H, A \succeq 0,$$

$$\text{and } A_{ii} = 1/K_1 \text{ for } i = 1, \ldots K_1.$$

We see that this feasibility problem is very similar to that in Eq. (4.24), the only differ-ence being that the constraint $\text{Tr}(A) = 1$ in Eq. (4.24) changes to $A_{ii} = 1/\sqrt{K_1}$ for $i = 1, \ldots K_1$. After we obtain an A_{opt} after the bisection search, through its eigen-decomposition $A_{\text{opt}} = \sum_{i=1}^{K_1} \lambda_i \, \underline{u}_i \cdot \underline{u}_i^H$, we can arrive at a deterministic approximation for the modal coef-ficient vector as

$$\underline{a}_{\text{fmf,phs,sdp}} = \underline{p} \left(\angle \underline{u}_1 \right). \tag{4.31}$$

or a randomized approximation as

$$\underline{a}_{\text{fmf,phs,sdp}}^{\text{rand}} = \underline{p} \left(\angle \left(\sum_{i=1}^{K_1} \sqrt{\lambda_i} \, \underline{u}_i \cdot \underline{u}_i^H \right) \cdot z \right). \tag{4.32}$$

Here, $z = z_R + \sqrt{-1} \, z_I$. $z_R, z_I \in \mathbb{R}^{K_1}$ are i.i.d. random vectors that are normally distributed with a zero mean and covariance matrix $I^{K_1 \times K_1}/2$.

4.3 Multi-Foci Focusing with Contrast

4.3.1 Maximal-Total-Intensity Focusing

4.3.1.1 Solution for Phase-Amplitude Modulation

In addition to creating multiple foci at $\{r_1, r_2, \ldots, r_q\}$, some applications require that the focused wavefront avoid creating significant fields at particular spots $\{s_1, s_2, \ldots, s_p\}$.

Under such circumstances, the optimization problem for finding the incident wavefront $\underline{a}_{\mathsf{mfc}}$ for phase-amplitude modulation can be expressed as

$$
\begin{aligned}
\underline{a}_{\mathsf{mfc}} &= \underset{\left\|\underline{a}_1^+\right\|_2 \neq 0}{\arg\max} \frac{\sum_{i=1}^q \left\|\boldsymbol{E}_2^+(\boldsymbol{r}_i)\right\|_2^2}{\sum_{j=1}^p \left\|\boldsymbol{E}_2^+(\boldsymbol{s}_j)\right\|_2^2} \\
&= \underset{\left\|\underline{a}_1^+\right\|_2 \neq 0}{\arg\max} \frac{\sum_{i=1}^q \left\|C(\boldsymbol{r}_i) \cdot \underline{a}_1^+\right\|_2^2}{\sum_{j=1}^p \left\|C(\boldsymbol{s}_j) \cdot \underline{a}_1^+\right\|_2^2} \\
&= \underset{\left\|\underline{a}_1^+\right\|_2 \neq 0}{\arg\max} \frac{\left\|Q \cdot \underline{a}_1^+\right\|_2^2}{\left\|\underbrace{\left[C^T(\boldsymbol{s}_1) \quad C^T(\boldsymbol{s}_2) \quad \ldots \quad C^T(\boldsymbol{s}_p)\right]^T}_{:=P} \cdot \underline{a}_1^+\right\|_2^2},
\end{aligned}
\tag{4.33}
$$

in which $P \in \mathbb{C}^{3p \times K_1}$. The objective function of Eq. (4.33) has a meaningful solution only if its denominator is not zero. If matrix P is left-invertible, viz. the columns of P are linearly independent, we can compute its Moore-Penrose pseudoinverse [69] as $P^\dagger = P \cdot (P^H \cdot P)^{-1}$. Let $\underline{b} = P \cdot \underline{a}_1^+$. Let $\underline{b} = P \cdot \underline{a}_1^+$, and thereby $\underline{a}_1^+ = P^\dagger \cdot \underline{b}$. Then, Eq. (4.33) can be written as

$$
\begin{aligned}
\underline{a}_{\mathsf{mfc}} &= \underset{\left\|\underline{a}_1^+\right\|_2 \neq 0}{\arg\max} \frac{\left\|Q \cdot \underline{a}_1^+\right\|_2^2}{\left\|P \cdot \underline{a}_1^+\right\|_2^2} \\
&= \underset{\left\|\underline{a}_1^+\right\|_2 \neq 0}{\arg\max} \frac{(\underline{a}_1^+)^H \cdot Q^H \cdot Q \cdot \underline{a}_1^+}{(\underline{a}_1^+)^H \cdot P^H \cdot P \cdot \underline{a}_1^+} \\
&= \underset{\left\|\underline{b}\right\|_2 \neq 0}{\arg\max} \frac{\underline{b}^H \cdot (P^\dagger)^H \cdot Q^H \cdot Q \cdot P^\dagger \cdot \underline{b}}{\underline{b}^H \cdot \underline{b}} \\
&= \underset{\left\|\underline{b}\right\|_2 = 1}{\arg\max} \left\|Q \cdot P^\dagger \cdot \underline{b}\right\|_2^2.
\end{aligned}
\tag{4.34}
$$

With the singular value decomposition $Q \cdot P^\dagger = \sum_i \sigma_i \, \underline{u}_i \cdot \underline{v}_i^H$, solution of Eq. (4.34) as

$$
\underline{a}_{\mathsf{mfc}} = P^\dagger \cdot \underline{v}_1.
\tag{4.35}
$$

However, in practice, we usually have a small number (p) of spots where field intensities

needed to be suppressed. This situation leads to $3p < K_1$, and consequently matrix P is not left-invertible. Under such circumstances, we change the objective function in Eq. (4.34) to

$$
\begin{aligned}
\underline{a}_{\mathsf{mfc}} &= \arg\max_{\underline{a}_1^+ \in \mathcal{R}(Q)} \frac{\left\| Q \cdot \underline{a}_1^+ \right\|_2^2}{\left\| P \cdot \underline{a}_1^+ \right\|_2^2 + \varepsilon^2 \left\| Q \cdot \underline{a}_1^+ \right\|_2^2} \\
&= \arg\max_{\underline{a}_1^+ \in \mathcal{R}(Q)} \frac{\left\| Q \cdot \underline{a}_1^+ \right\|_2^2}{\left\| \left[P^T , \varepsilon \cdot Q^T \right]^T \cdot \underline{a}_1^+ \right\|_2^2} ,
\end{aligned}
\tag{4.36}
$$

where $\mathcal{R}(Q)$ denotes the range of matrix Q [78], and ε is a small positive number. A simple and practical approximate solution to Eq. (4.36) can be obtained through the singular value decomposition of the composite matrix:

$$
D = \begin{bmatrix} \mathcal{N}^H(P) \\ \varepsilon \cdot Q \end{bmatrix}
\tag{4.37}
$$

in which $\mathcal{N}(P)$ is the null space of matrix P. Specifically, for $D = \sum_i \sigma_i \underline{u}_i \cdot \underline{v}_i^H$, we have

$$
\underline{a}_{\mathsf{mfc}} = \underline{v}_1.
\tag{4.38}
$$

In practice, the null space of P and Q rarely overlap and thus $\underline{a}_{\mathsf{mfc}} = \underline{v}_1$ is very unlikely to cause the denominator of Eq. (4.36) to vanish.

4.3.1.2 Solution for Phase-Only Modulation

Similar to the non-contrast focusing problem, an approximation solution to

$$
\underline{a}_{\mathsf{mfc,phs}} = \arg\max_{\underline{a}_1^+ \in P_1^{K_1}} \frac{\left\| Q \cdot \underline{a}_1^+ \right\|_2^2}{\left\| P \cdot \underline{a}_1^+ \right\|_2^2} ,
\tag{4.39}
$$

involves applying the spherical relaxation to $\underline{a}_{\text{mfc}}$:

$$\underline{a}_{\text{mfc,phs}} = \underline{p}(\angle \underline{a}_{\text{mfc}}), \tag{4.40}$$

However, if we want a "tighter" approximation, the SDP technique should be used. Here, we proposed a method using the bisection search and SDP solver, which is very similar to the method we used to tackle the non-contrast fair focusing problem in Sections 4.2.2.1 and 4.2.2.2.

The right hand side of Eq. (4.39) can be rewritten as follows:

$$
\begin{aligned}
\underset{\underline{a}_1^+ \in P_1^{K_1}}{\arg\max} \frac{\left\| Q \cdot \underline{a}_1^+ \right\|_2^2}{\left\| P \cdot \underline{a}_1^+ \right\|_2^2} &= \underset{\underline{a}_1^+ \in P_1^{K_1}}{\arg\max} \frac{(\underline{a}_1^+)^H \cdot Q^H \cdot Q \cdot \underline{a}_1^+}{(\underline{a}_1^+)^H \cdot P^H \cdot P \cdot \underline{a}_1^+} \\
&= \underset{\underline{a}_1^+ \in P_1^{K_1}}{\arg\max} \frac{\operatorname{Tr}\left(Q^H \cdot Q \cdot \underline{a}_1^+ \cdot (\underline{a}_1^+)^H\right)}{\operatorname{Tr}\left(P^H \cdot P \cdot \underline{a}_1^+ \cdot (\underline{a}_1^+)^H\right)}.
\end{aligned}
\tag{4.41}
$$

Let $A = \underline{a}_1^+ \cdot (\underline{a}_1^+)^H$; clearly, A is a rank-one Hermitian, positive semidefinite matrix. For phase-only modulation, the feasible set $\underline{a}_1^+ \in P_1^{K_1}$ manifests itself in A as $A_{ii} = 1/K_1, (i = 1, \ldots, K_1)$. Hence, the equivalent optimization problem for A is

$$
\begin{aligned}
A_{\text{opt}} = \underset{A \in \mathbb{C}^{K_1 \times K_1}}{\arg\max} \, &\frac{\operatorname{Tr}\left(Q^H \cdot Q \cdot A\right)}{\operatorname{Tr}\left(P^H \cdot P \cdot A\right)} \\
\text{subject to } &A = A^H, A \succeq 0, \\
&\operatorname{rank}(A) = 1, \\
&\text{and } A_{ii} = 1/K_1 \text{ for } i = 1, \ldots K_1.
\end{aligned}
\tag{4.42}
$$

Eq. (4.42) is very similar to the trace quotient problem but with more restraints on A, and it does not have a closed form solution.

The following reformulation is similar to that for the non-contrast fair focusing prob-

lem. By introducing an auxiliary variable η, the problem in Eq. (4.42) is equivalent to

$$
\begin{aligned}
A_{\mathsf{opt}} = \underset{A \in \mathbb{C}^{K_1 \times K_1}}{\arg\max} \quad & (\eta) \\
\text{subject to } & \mathrm{Tr}\left(Q^H \cdot Q \cdot A\right) \geq \eta \cdot \mathrm{Tr}\left(P^H \cdot P \cdot A\right) \\
& A = A^H, A \succeq 0, \\
& \mathrm{rank}(A) = 1, \\
& \text{and } A_{ii} = 1/K_1 \text{ for } i = 1, \dots K_1.
\end{aligned}
\tag{4.43}
$$

Furthermore, by dropping the rank-one constraint, we convert the above optimization problem into a set of convex feasibility problems with a given $\eta^* \in \mathbb{R}$:

$$
\begin{aligned}
\text{find } & A \in \mathbb{C}^{K_1 \times K_1} \\
\text{subject to } & \mathrm{Tr}\left(Q^H \cdot Q \cdot A\right) \geq \eta^* \cdot \mathrm{Tr}\left(P^H \cdot P \cdot A\right) \\
& A = A^H, A \succeq 0, \\
& \text{and } A_{ii} = 1/K_1 \text{ for } i = 1, \dots K_1.
\end{aligned}
\tag{4.44}
$$

If Eq. (4.44) is feasible, we have $\eta_{\mathsf{opt}} \geq \eta^*$; otherwise $\eta_{\mathsf{opt}} < \eta^*$. The subsequent bisection search procedure is the same as that of Algorithm 4.1; we only change the feasibility problem in line 8 in Eq. (4.44).

The initial input η_L and η_U can be estimated by the theorem given in [79]. Specifically, let $\lambda_1(S) \geq \lambda_2(S) \geq \dots \geq \lambda_{K_1}(S)$ denote the sorted (largest to smallest) eigenvalues of Hermitian, positive semidefinite matrix $S^{K_1 \times K_1}$. In addition, if $\mathrm{rank}(A) = d$, then we have

$$
\max \mathrm{Tr}\left(S \cdot A\right) \leq \frac{1}{d} \sum_{i=1}^{d} \lambda_i(S),
\tag{4.45}
$$

$$
\min \mathrm{Tr}\left(S \cdot A\right) \geq \frac{1}{d} \sum_{i=1}^{d} \lambda_{M-i+1}(S),
\tag{4.46}
$$

in which the equal sign can be achieved if A can be decomposed as $A = W \cdot W^H$, where

W is a $K_1 \times d$ matrix and $d \cdot (W^H \cdot W) = I^{d \times d}$. Actually, this constraint on A is looser than that in Eq. (4.44); thus, we confidently make the following initialization

$$\eta_U = \frac{\sum_{i=1}^{d} \lambda_i (Q^H \cdot Q)}{\sum_{i=1}^{d} \lambda_{K_1-i+1}(P^H \cdot P)}, \tag{4.47}$$

$$\eta_L = \frac{\sum_{i=1}^{d} \lambda_{K_1-i+1}(Q^H \cdot Q)}{\sum_{i=1}^{d} \lambda_i (P^H \cdot P)}. \tag{4.48}$$

The above approach and conclusion are only valid for $\text{Tr}\left(P^H \cdot P \cdot A\right) \neq 0$. Otherwise, η_U does not exist (tends to infinity). Hence, if $\text{Tr}\left(P^H \cdot P \cdot A\right) = 0$ occurs, we make the replacement:

$$P \rightarrow \begin{bmatrix} P \\ \varepsilon \cdot \mathcal{N}(P) \end{bmatrix} = R \tag{4.49}$$

where $\mathcal{N}(P)$ is the null space of P, and ε is a small real number. Consequently, the convex feasibility problem of Eq. (4.44) becomes

$$\begin{aligned}
&\text{find } A \in \mathbb{C}^{K_1 \times K_1} \\
&\text{subject to } \text{Tr}\left(Q^H \cdot Q \cdot A\right) > \eta^* \cdot \text{Tr}\left(R^H \cdot R \cdot A\right) \\
&\qquad A = A^H, A \succeq 0, \\
&\text{and } A_{ii} = 1/K_1 \text{ for } i = 1, \ldots K_1,
\end{aligned} \tag{4.50}$$

in which $R^H \cdot R$ is not singular, thereby rendering a meaningful solution to η_{opt}.

After A_{opt} is found, we proceed with the eigen-decomposition $A_{\text{opt}} = \sum_{i=1}^{K_1} \lambda_i \underline{u}_i \cdot \underline{u}_i^H$ with the eigenvalues arranged as $\lambda_1 \geq \ldots \lambda_{K_1} \geq 0$. 0. We then obtain a deterministic approximation for the modal coefficient vector as

$$\underline{a}_{\text{mfc,phs,sdp}} = \underline{p}\left(\angle \underline{u}_1\right). \tag{4.51}$$

or a randomized approximation as

$$\underline{a}_{\text{mfc,phs,sdp}}^{\text{rand}} = \underline{p} \left(\left/ \left(\sum_{i=1}^{K_1} \sqrt{\lambda_i}\, \underline{u}_i \cdot \underline{u}_i^H \right) \cdot z \right) \right. . \tag{4.52}$$

Here, $z = z_R + \sqrt{-1}\, z_I$. $z_R, z_I \in \mathbb{R}^{K_1}$ are i.i.d. random vectors that are normally distributed with zero mean and covariance matrix $I^{K_1 \times K_1}/2$. Eq. (4.52) provides a stable and near-optimum solution on average.

4.3.2 Even-Intensity (Fair) Focusing

4.3.2.1 Solution for Phase-Amplitude Modulation

For phase-amplitude modulation, the fair focusing problem with contrast can be stated as

$$\underline{a}_{\text{fmfc}} = \arg \max_{\left\| \underline{a}_1^+ \right\|_2 = 1} \; \min_{i=1,\dots,q} \left(\frac{\left\| Q_i \cdot \underline{a}_1^+ \right\|_2^2}{\left\| P \cdot \underline{a}_1^+ \right\|_2^2} \right). \tag{4.53}$$

It is essentially a fractional programming problem that can be solved via bisection search as well. Specifically, let $A = \underline{a}_1^+ \cdot (\underline{a}_1^+)^H$ be a rank-one, Hermitian and positive semidefinite matrix. Then, the equivalent optimization problem for Eq. (4.53) is

$$\begin{aligned}
A_{\text{opt}} = \arg \max_{A \in \mathbb{C}^{K_1 \times K_1}} \; &\min_{i=1,\dots,q} \left(\frac{\text{Tr}\left(Q_i^H \cdot Q_i \cdot A \right)}{\text{Tr}\left(P^H \cdot P \cdot A \right)} \right) \\
&\text{subject to } A = A^H, A \succeq 0, \\
&\text{rank}(A) = 1, \\
&\text{and } \text{Tr}(A) = 1.
\end{aligned} \tag{4.54}$$

Again, to avoid the situation of $\text{Tr}\left(P^H \cdot P \cdot A \right) = 0$, we replace the matrix P with the matrix R defined in Eq. (4.49). By dropping the rank-one constraint, the corresponding

convex feasibility problem for a given contrast ratio η^* is

$$\text{find } A \in \mathbb{C}^{K_1 \times K_1}$$

$$\text{subject to } \min_{i=1,\ldots,q} \left(\text{Tr} \left(Q_i \cdot Q_i^H \cdot A - \eta^* R \cdot R^H \cdot A \right) \right) \geq 0$$

$$A = A^H, A \succeq 0,$$

$$\text{and } \text{Tr}(A) = 1$$

(4.55)

Replacing the feasibility problem in line 8 of Algorithm 4.1 with Eq. (4.55), the maximal feasible η^* can be approached by implementing the bisection search in the same way as above. The corresponding approximate solution to $\underline{a}_{\text{fmfc}}$ is denoted by $\underline{a}_{\text{fmfc,sdp}}$.

4.3.2.2   Solution for Phase-Only Modulation

By changing the feasible set $\left\| \underline{a}_1^+ \right\|_2 = 1$ in Eq. (4.53) to $\underline{a}_1^+ \in P_1^{K_1}$, we reach the corresponding optimization problem for phase-only modulation as

$$\underline{a}_{\text{fmfc,phs}} = \arg\max_{\underline{a}_1^+ \in P_1^{K_1}} \min_{i=1,\ldots,q} \left(\frac{\left\| Q_i \cdot \underline{a}_1^+ \right\|_2^2}{\left\| P \cdot \underline{a}_1^+ \right\|_2^2} \right).$$

(4.56)

Similar to the case of fair-contrast focusing for phase-amplitude modulation, letting $A \approx \underline{a}_1^+ \cdot (\underline{a}_1^+)^H$ with the relaxation on the rank constraint, and replacing matrix P with matrix R, we obtain the corresponding matrix optimization problem:

$$A_{\text{opt}} = \arg\max_{A \in \mathbb{C}^{K_1 \times K_1}} \min_{i=1,\ldots,q} \left(\frac{\text{Tr} \left(Q_i^H \cdot Q_i \cdot A \right)}{\text{Tr} \left(R^H \cdot R \cdot A \right)} \right)$$

$$\text{subject to } A = A^H, A \succeq 0,$$

$$\text{and } A_{ii} = 1/K_1 \text{ for } i = 1, \ldots K_1.$$

(4.57)

This problem can also be solved via the bisection search approach. After A_{opt} obtained, with the eigen-decomposition $A_{\text{opt}} = \sum_{i=1}^{K_1} \lambda_i \underline{u}_i \cdot \underline{u}_i^H$ where the eigenvalues arranged as $\lambda_1 \geq \ldots \lambda_{K_1} \geq 0$, we can reach a deterministic approximation for the modal coefficient

vector as

$$\underline{a}_{\text{fmfc,phs,sdp}} = \underline{p}\left(\angle\underline{u}_1\right).$$ (4.58)

or a randomized approximation as

$$\underline{a}_{\text{fmfc,phs,sdp}}^{\text{rand}} = \underline{p}\left(\angle\overline{\left(\sum_{i=1}^{K_1}\sqrt{\lambda_i}\,\underline{u}_i\cdot\underline{u}_i^H\right)\cdot z}\right),$$ (4.59)

where $z = z_R + \sqrt{-1}\,z_I$. $z_R, z_I \in \mathbb{R}^{K_1}$ are i.i.d. random vectors that are normally distributed with zero mean and covariance matrix $I^{K_1 \times K_1}/2$.

4.4 Summary of Focusing Methods

Tables 4.1 and 4.2 summarize the objective functions and available solutions for different focusing conditions and interests.

Table 4.1: Objective functions and solutions for multi-foci focusing without contrast

contrast option	without contrast			
focusing preference	maximal total-intensity		even-intensity (fair)	
modulation option	phase-amplitude	phase-only	phase-amplitude	phase-only
objective function	Eq. (4.4)	Eq. (4.12)	Eq. (4.20)	Eq. (4.28)
solution	$\underline{a}_{\text{mf}}$ in Eq. (4.5) close form	$\underline{a}_{\text{mf,phs}}$ in Eq. (4.13) spherical relaxation	$\underline{a}_{\text{fmf,MLU}}$ in Eq. (4.21) MLU solution	$\underline{a}_{\text{fmf,phs,MLU}}$ in Eq. (4.29) MLU solution
		$\underline{a}_{\text{mf,phs,sdp}}$ in Eq. (4.18) SDP solution deterministic	$\underline{a}_{\text{fmf,sdp}}$ in Eq. (4.27) SDP solution deterministic	$\underline{a}_{\text{fmf,phs,sdp}}$ in Eq. (4.31) SDP solution deterministic
		$\underline{a}_{\text{mf,phs,sdp}}^{\text{rand}}$ in Eq. (4.19) SDP solution randomized		$\underline{a}_{\text{fmf,phs,sdp}}^{\text{rand}}$ in Eq. (4.32) SDP solution randomized

4.5 Numerical Simulations

To investigate the performance of the proposed multi-foci focusing algorithms, we test them on a random media model in Figure 3.1. This random media model is a periodic

Table 4.2: Objective functions and solutions for multi-foci focusing with contrast

contrast option	with contrast			
focusing preference	maximal total-intensity		even-intensity (fair)	
modulation option	phase-amplitude	phase-only	phase-amplitude	phase-only
objective function	Eq. (4.34) or Eq. (4.36)	Eq. (4.39)	Eq. (4.53)	Eq. (4.56)
solution	$\underline{a}_\text{mfc}$ in Eq. (4.35) close form	$\underline{a}_\text{mfc,phs}$ in Eq. (4.40) spherical relaxation		
	or $\underline{a}_\text{mfc}$ in Eq. (4.38) close form	$\underline{a}_\text{mfc,phs,sdp}$ in Eq. (4.51) SDP solution deterministic	$\underline{a}_\text{fmfc,sdp}$ in Eq. (4.55) SDP solution deterministic	$\underline{a}_\text{fmfc,phs,sdp}$ in Eq. (4.51) SDP solution deterministic
		$\underline{a}_\text{mfc,phs,sdp}^\text{rand}$ in Eq. (4.52) SDP solution randomized		$\underline{a}_\text{fmfc,phs,sdp}^\text{rand}$ in Eq. (4.59) SDP solution randomized

multi-layer slab. The specific parameters are $D_x = D_y = 7.58\lambda$, $l = 4.0\lambda$, $K_1 = 354$. The number of layers is $N_c = 600$, where λ denotes the wavelength of the EM wave. We compute its scattering matrix via a highly-accurate, IE-based 3D solver that characterizes the field scattered from each scatterer. The periodic 3D Green's function is evaluated rapidly by using a recursive Shanks transformation. Care is taken to ensure 6 digit accuracy in the calculation of each entry of the scattering matrix.

For the multi-foci focusing problem without contrast, we aim for 12 foci that form a "C" shape on the xy plane located 2.0λ behind the slab (Region 2). By applying different focusing algorithms proposed for different conditions and preferences, we obtain the corresponding focused wavefronts and reconstruct the electric field intensity on the plane where the foci reside. Field intensities demonstrate the efficacy of each algorithm. For each result, we also provide the value of the $\|Q \cdot \underline{a}_1^+\|_2$ and the minimal focusing intensity among the 12 foci $\min_{i=1,\ldots,q} \left(\|Q_i \cdot \underline{a}_1^+\|_2 \right)$.

First of all, we excite the slab from Region 1 with the naive focusing wavefront $\underline{a}_\text{nmf}$ as if no slab is present. The electric field intensity on the focal plane is shown in Figure 4.1a. The expected foci are marked by squares. As can be seen, all foci are hard to distinguish from the background noise, because the focused wavefront is completely distorted by the slab.

However, if we excite the slab with the optimized $\underline{a}_{mf}$ from Eq. (4.5), a clear "C" shape appears on the focal plane, as shown in Figure 4.1b. Nevertheless, the focus intensities

(a) $\underline{a}_{nmf}$ (b) $\underline{a}_{mf}$

Figure 4.1: Electric field intensity on the $(x, y, 2\lambda)$ plane behind the slab (in Region 2) due to (a) $\underline{a}_{nmf}$, obtaining $\|Q \cdot \underline{a}_{nmf}\|_2 = 3.9722$ and $\min_{i=1,\dots,q} \|Q_i \cdot \underline{a}_{nmf}\|_2 = 0.70575$; (b) $\underline{a}_{mf}$, obtaining $\|Q \cdot \underline{a}_{mf}\|_2 = 17.5863$ and $\min_{i=1,\dots,q} \|Q_i \cdot \underline{a}_{mf}\|_2 = 1.9229$.

among the 12 foci are highly uneven. Some foci on the left side are remarkably weaker than others. We apply the even-intensity (fair) focusing optimizer via bisection search and SDP from Eq. (4.27). All foci become even as shown in Figure 4.2. Comparing to the previous one, the minimal focusing intensity of individual spot among the 12 foci has been enhanced more than 2-fold (from 1.9229 to 5.0153), while the overall focusing intensity has barely changed (17.5864 vs. 17.3735). For reference, Figure (4.3a) and Figure (4.3b) illustrate the results of the MLU optimized fair focusing wavefronts initialized with $\underline{a}_{nmf}$ and $\underline{a}_{mf}$, respectively. The number of MLU iterations is set to 100. We see that different initializations do not affect the final results much. The MLU algorithm performs well with results only slightly inferior to that of the bisection search $+$ SDP method in this particular example.

Next, we check the efficacy of focused wavefronts for phase-only modulation. Figure

Figure 4.2: Electric field intensity on the $(x, y, 2\lambda)$ plane behind the slab (in Region 2) due to $\underline{a}_{\text{fmf,sdp}}$, obtaining $\|Q \cdot \underline{a}_{\text{fmf,sdp}}\|_2 = 17.3735$ and $\min_{i=1,\ldots,q} \|Q_i \cdot \underline{a}_{\text{fmf,sdp}}\|_2 = 5.0153$.

(a) $\underline{a}_{\text{fmf,MLU}}$ initialized with $\underline{a}_{\text{nmf}}$

(b) $\underline{a}_{\text{fmf,MLU}}$ initialized with $\underline{a}_{\text{mf}}$

Figure 4.3: Electric field intensity on the $(x, y, 2\lambda)$ plane behind the slab (in Region 2) due to (a) $\underline{a}_{\text{fmf,MLU}}$ initialized with $\underline{a}_{\text{nmf}}$, obtaining $\|Q \cdot \underline{a}_{\text{fmf,MLU}}\|_2 = 17.4469$ and $\min_{i=1,\ldots,q} \|Q_i \cdot \underline{a}_{\text{fmf,MLU}}\|_2 = 4.6693$; (b) $\underline{a}_{\text{fmf,MLU}}$ initialized with $\underline{a}_{\text{mf}}$, obtaining $\|Q \cdot \underline{a}_{\text{fmf,MLU}}\|_2 = 17.4474$ and $\min_{i=1,\ldots,q} \|Q_i \cdot \underline{a}_{\text{fmf,MLU}}\|_2 = 4.6724$.

(4.4) shows the result of $\underline{a}_{\text{mf,phs}}$ from simple spherical relaxation based on $\underline{a}_{\text{mf}}$. By contrast, the results from the SDP solver, $\underline{a}_{\text{mf,phs,sdp}}$ and $\underline{a}_{\text{mf,phs,sdp}}^{\text{rand}}$, are presented in Figure 4.5a and

Figure 4.4: Electric field intensity on the $(x, y, 2\lambda)$ plane behind the slab (in Region 2) due to $\underline{a}_{\mathsf{mf,phs}}$, with $\|Q \cdot \underline{a}_{\mathsf{mf,phs}}\|_2 = 13.8183$ and $\min_{i=1,\ldots,q} \|Q_i \cdot \underline{a}_{\mathsf{mf,phs}}\|_2 = 2.4301$.

4.5b, respectively.

(a) $\underline{a}_{\mathsf{mf,phs,sdp}}$

(b) $\underline{a}_{\mathsf{mf,phs,sdp}}^{\mathsf{rand}}$

Figure 4.5: Electric field intensity on the $(x, y, 2\lambda)$ plane behind the slab (in region 2) due to (a) $\underline{a}_{\mathsf{mf,phs,sdp}}$, obtaining $\|Q \cdot \underline{a}_{\mathsf{mf,phs,sdp}}\|_2 = 15.1189$ and $\min_{i=1,\ldots,q} \|Q_i \cdot \underline{a}_{\mathsf{mf,phs,sdp}}\|_2 = 1.8218$; (b) $\underline{a}_{\mathsf{mf,phs,sdp}}^{\mathsf{rand}}$, obtaining $\|Q \cdot \underline{a}_{\mathsf{mf,phs,sdp}}^{\mathsf{rand}}\|_2 = 14.8613$ and $\min_{i=1,\ldots,q} \|Q_i \cdot \underline{a}_{\mathsf{mf,phs,sdp}}^{\mathsf{rand}}\|_2 = 2.1285$.

We see that the overall focus intensities from the SDP solutions are modestly superi-

ority to the spherical relaxation solution (15.1189 and 14.8613 over 13.8183). The results for even-intensity (fair) focusing wavefronts for phase-only modulation are shown in Figs. 4.6a and 4.6b. Compared to the results of $\underline{a}_{\text{mf,phs,sdp}}$ and $\underline{a}_{\text{mf,phs,sdp}}^{\text{rand}}$ in Figs. 4.5a and 4.5b, the additional even-intensity enforcement does not induce "fairness" on the focusing intensity. However, if we apply the MLU algorithm to generate the corresponding fair focusing
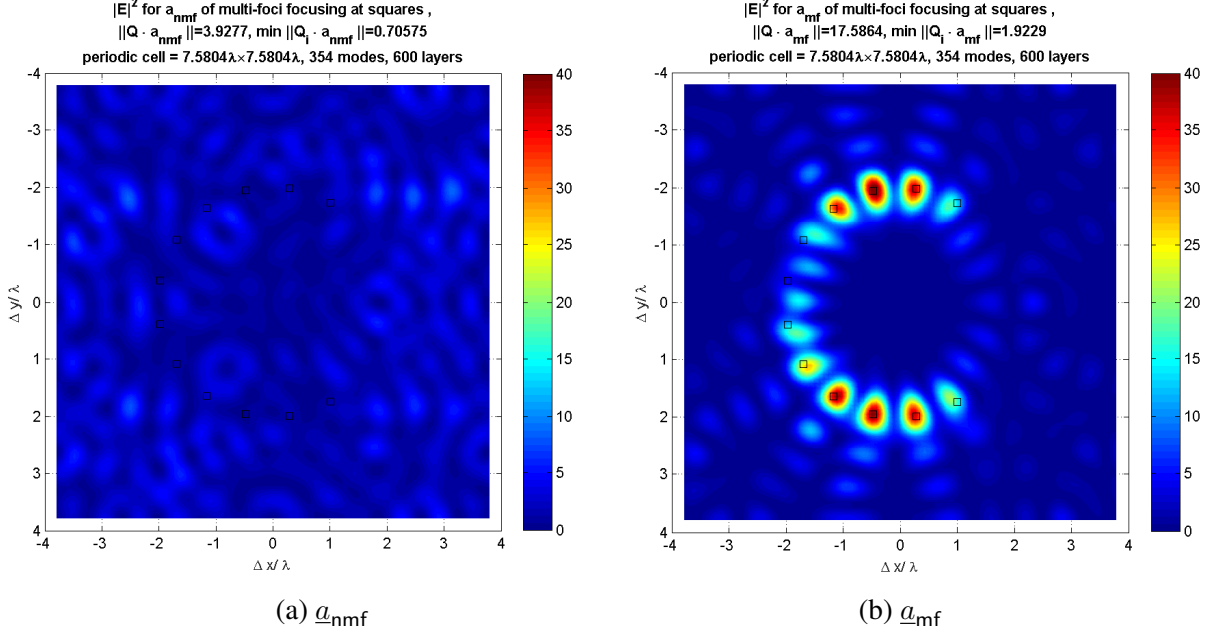

Figure 4.6: Electric field intensity on the $(x, y, 2\lambda)$ plane behind the slab (in Region 2) due to (a) $\underline{a}_{\text{mf,phs,sdp}}$, obtaining $\|Q \cdot \underline{a}_{\text{mf,phs,sdp}}\|_2 = 15.1189$ and $\min_{i=1,\ldots,q} \|Q_i \cdot \underline{a}_{\text{mf,phs,sdp}}\|_2 = 1.8218$; (b) $\underline{a}_{\text{mf,phs,sdp}}^{\text{rand}}$, obtaining $\|Q \cdot \underline{a}_{\text{mf,phs,sdp}}^{\text{rand}}\|_2 = 14.8613$ and $\min_{i=1,\ldots,q} \|Q_i \cdot \underline{a}_{\text{mf,phs,sdp}}^{\text{rand}}\|_2 = 2.1285$.

wavefronts for the phase-only modulation, the result is much better, as shown in Figs. 4.7a and 4.7b. Each of the figures is the result of the MLU algorithm working on the initialization $\underline{a}_{\text{mf,phs}}$ and $\underline{a}_{\text{mf,phs,sdp}}$, respectively. Apparently, this case differs from the case of fair focusing for phase-amplitude modulation. In fair focusing for phase-only modulation, the MLU algorithm does a better job than the bisection + SDP method. Again, different initializations do not seem to affect the MLU results much.

For the multi-foci focusing problem with contrast, we seek a set of desired foci forming a circle with another set of spots —- where field intensities need to be suppressed —- dis-

(a) $\underline{a}_{\mathsf{fmf,phs,MLU}}$ initialized with $\underline{a}_{\mathsf{mf,phs}}$ (b) $\underline{a}_{\mathsf{fmf,phs,MLU}}$ initialized with $\underline{a}_{\mathsf{mf,phs,sdp}}$

Figure 4.7: Electric field intensity on the $(x, y, 2\lambda)$ plane behind the slab (in Region 2) due to (a) $\underline{a}_{\mathsf{fmf,phs,MLU}}$ initialized with $\underline{a}_{\mathsf{mf,phs}}$, obtaining $\|Q \cdot \underline{a}_{\mathsf{fmf,phs,MLU}}\|_2 = 14.3852$ and $\min_{i=1,...,q} \|Q_i \cdot \underline{a}_{\mathsf{fmf,phs,MLU}}\|_2 = 3.6328$; (b) $\underline{a}_{\mathsf{fmf,phs,MLU}}$ initialized with $\underline{a}_{\mathsf{mf,phs,sdp}}$, obtaining $\|Q \cdot \underline{a}_{\mathsf{fmf,phs,MLU}}\|_2 = 14.3724$ and $\min_{i=1,...,q} \|Q_i \cdot \underline{a}_{\mathsf{fmf,phs,MLU}}\|_2 = 3.6507$.

tributed in the gaps of the foci and forming a concentric ring. First, we use a non-contrast focusing method; in essence, the solution $\underline{a}_{\mathsf{mf}}$ of the maximal-total-intensity focusing problem for phase-amplitude modulation is used to focus on the desired foci. The result is shown in Figure 4.8. In this figure, the desired foci are marked by squares, while the spots where fields need to be suppressed are marked by circles. We see that many unwanted foci appear near the circles, mainly due to the complicated interference of EM waves arriving at the focal plane from all directions. On the other hand, the result from the contrast focusing wavefront $\underline{a}_{\mathsf{mfc}}$ generated via Eq. (4.36) completely suppresses the fields on the circular spots, as shown in Figure 4.9a. For wavefront $\underline{a}_{\mathsf{mfc}}$, the total field intensity among the suppressed spots $\|P \cdot \underline{a}_{\mathsf{mfc}}\|_2 = 5.203 \times 10^{-15}$ is practically zero. Moreover, by adding the even-intensity constraint to this phase-amplitude contrast focusing problem, the obtained wavefront $\underline{a}_{\mathsf{fmf,sdp}}$ from the bisection search + SDP method in Eq. 4.55 results in even better overall focusing intensity. It also achieves better fairness of the focusing intensities
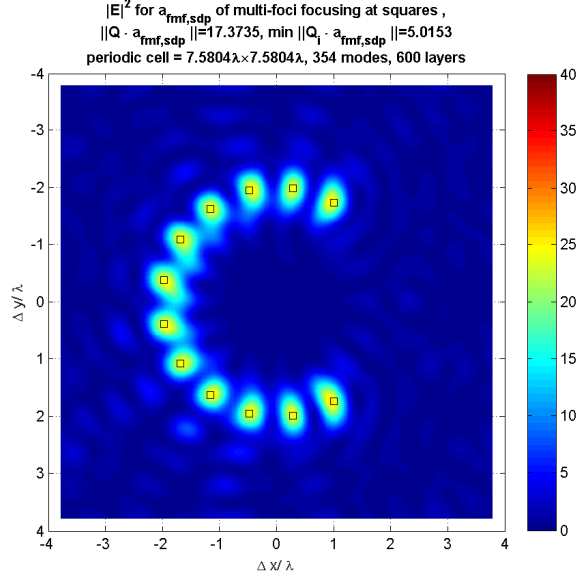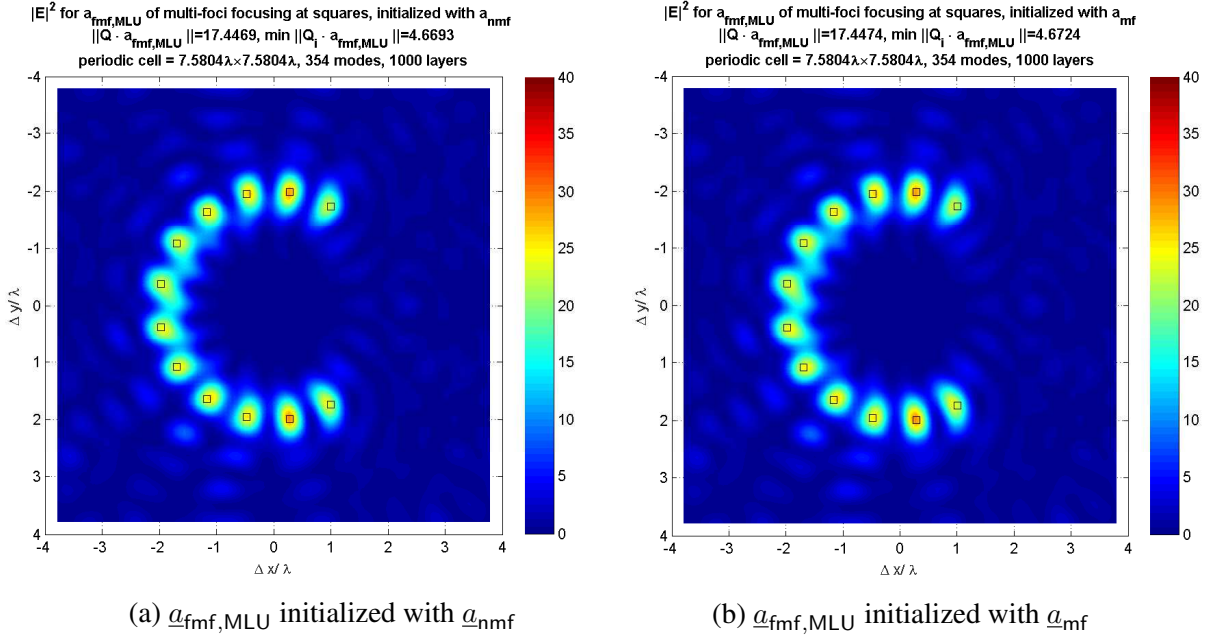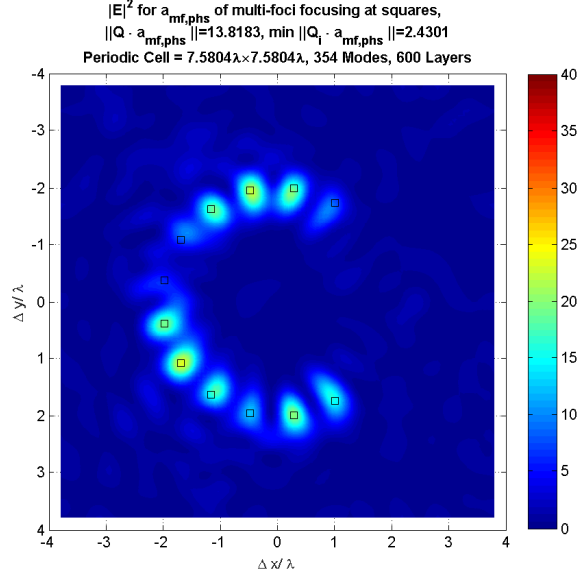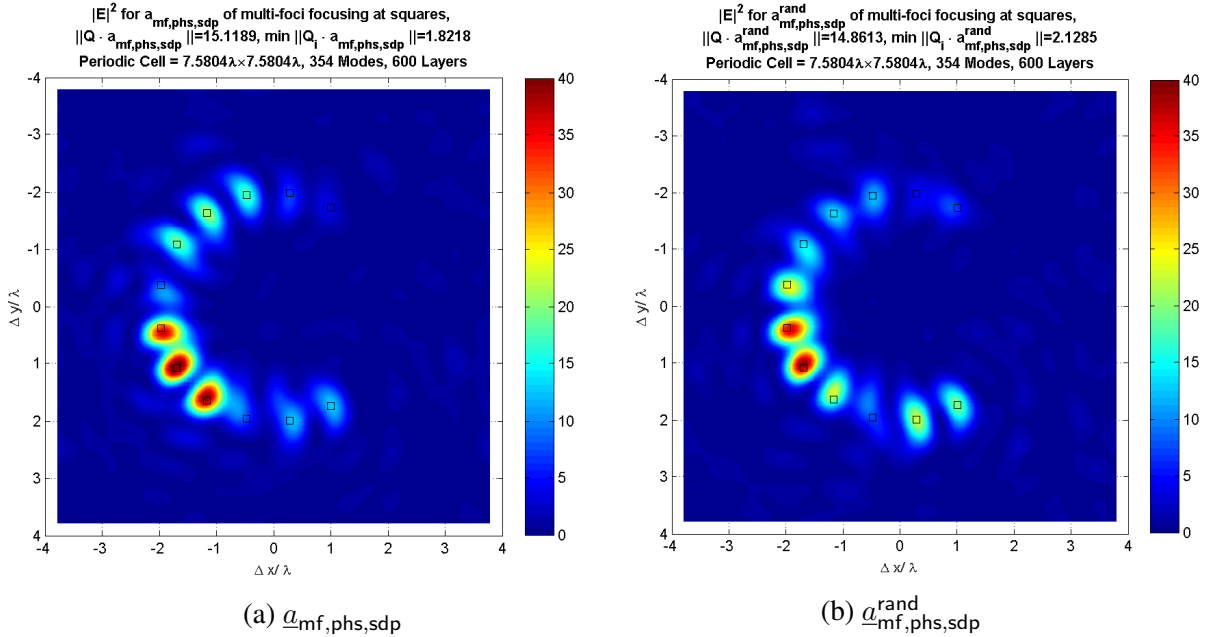
Figure 4.8: Electric field intensity on the $(x, y, 2\lambda)$ plane behind the slab (in Region 2) due to $\underline{a}_{\mathrm{mf}}$, obtaining $\|Q \cdot \underline{a}_{\mathrm{mf}}\|_2 = 16.9994$, $\|P \cdot \underline{a}_{\mathrm{mf}}\|_2 = 12.4216$ and $\min_{i=1,\dots,q} \|Q_i \cdot \underline{a}_{\mathrm{mf,phs}}\|_2 = 4.0698$.

among the foci, as demonstrated in Figure 4.9b. In the case of contrast focusing for phase-only modulation, Figure 4.10 presents the result of $\underline{a}_{\mathrm{mfc,phs}}$, the spherical relaxation from $\underline{a}_{\mathrm{mfc}}$. Obviously, the spherical relaxation is not performing well w.r.t. maintaining field intensities at the foci. Instead, the $\underline{a}_{\mathrm{mfc,phs,sdp}}$ and $\underline{a}_{\mathrm{mfc,phs,sdp}}^{\mathrm{rand}}$ obtained from bisection search + SDP method result in better focusing intensity, as shown in Figs. 4.11a and 4.11b, respectively. Furthermore, by enforcing the even-intensity request, the $\underline{a}_{\mathrm{fmfc,phs,sdp}}$ and $\underline{a}_{\mathrm{fmfc,phs,sdp}}^{\mathrm{rand}}$ obtained from Eq. (4.31) and Eq. (4.32) result in slightly better outcomes with regard to the fairness of the focusing intensities among the foci, as shown in Figure (4.12a) and Figure (4.12b), respectively.

Lastly, we investigate how the thickness L of the random medium (multi-layer slab) affects the performance of the proposed multi-foci focusing algorithms. To do so, we inspect the focusing intensity, contrast ratio, and focusing fairness for the corresponding focusing methods as a function of L. In the following study, we continue to employ the C-shape arranged foci case for non-contrast focusing, and the circularly arranged foci (and
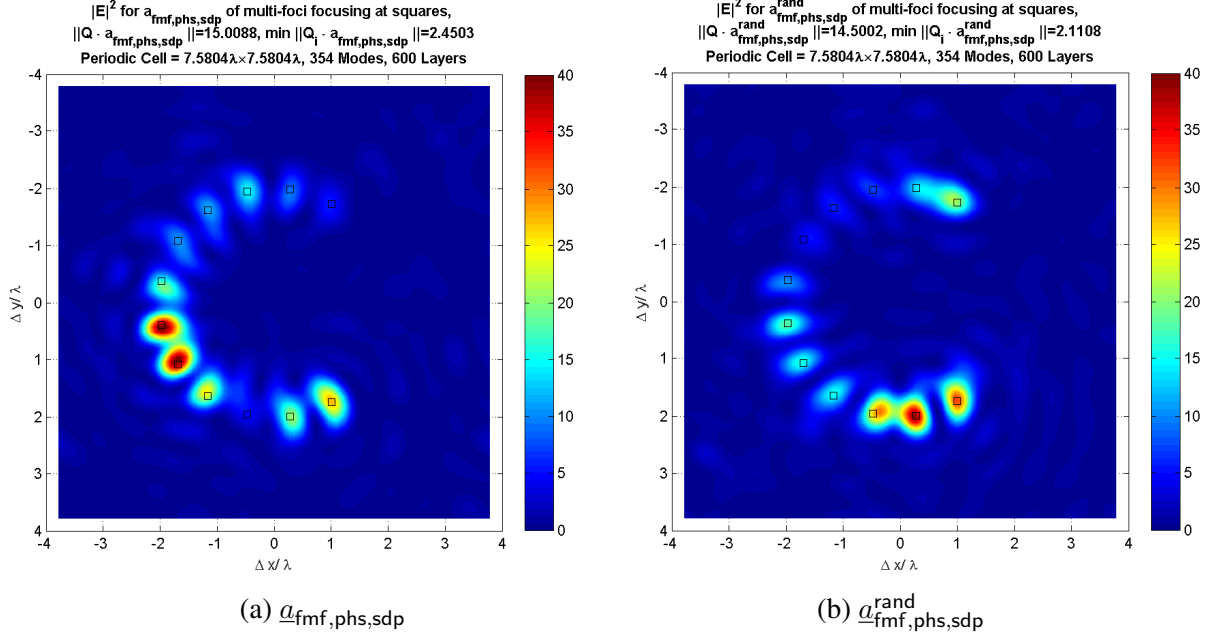
Figure 4.9: Electric field intensity on the $(x, y, 2\lambda)$ plane behind the slab (in Region 2) due to (a) $\underline{a}_{\text{mfc}}$, obtaining $\|Q \cdot \underline{a}_{\text{mfc}}\|_2 = 11.6216$, $\|P \cdot \underline{a}_{\text{mfc}}\|_2 = 5.203 \times 10^{-15}$ and $\min_{i=1,\ldots,q} \|Q_i \cdot \underline{a}_{\text{mfc}}\|_2 = 2.5026$; (b) $\underline{a}_{\text{fmfc,sdp}}$, obtaining $\|Q \cdot \underline{a}_{\text{fmfc,sdp}}\|_2 = 14.3724$, $\|P \cdot \underline{a}_{\text{fmfc,sdp}}\|_2 = 7.3774 \times 10^{-6}$ and $\min_{i=1,\ldots,q} \|Q_i \cdot \underline{a}_{\text{fmfc,sdp}}\|_2 = 4.2923$.

suppressed spots) case for contrast focusing. The thickness of the slab L ranges from 320λ to $3.52 \times 10^4 \lambda$, as the corresponding number of periodic layers ranges from 80 to $8,800$.

For non-contrast focusing, Figure 4.13a shows the average relative focusing intensity with respect to that achieved by $\underline{a}_{\text{mf}}$ for $\underline{a}_{\text{nmf}}$, $\underline{a}_{\text{mf,phs}}$, $\underline{a}_{\text{mf,phs,sdp}}$ and $\underline{a}_{\text{mf,phs,sdp}}^{\text{rand}}$, as a function of L. We see that all three optimized focusing wavefronts overwhelmingly perform better than the naive focusing wavefront. For phase-only modulation, the solution $\underline{a}_{\text{mf,phs,sdp}}$ form the SDP solver is slightly superior to $\underline{a}_{\text{mf,phs}}$ resulting from spherical relaxation. Inspection of the fairness of different focusing methods is shown in Figure 4.13b. Here, the fairness is defined as the minimal field intensity among all foci divided by the maximal field intensity observed at one of them. We see that enforcing the even-intensity condition substantially improves the fairness of the focusing for all fair focusing methods — even though increasing the thickness of the media slowly deteriorates the results. For phase-amplitude modulation, the bisection search + SDP method obtains better results than the
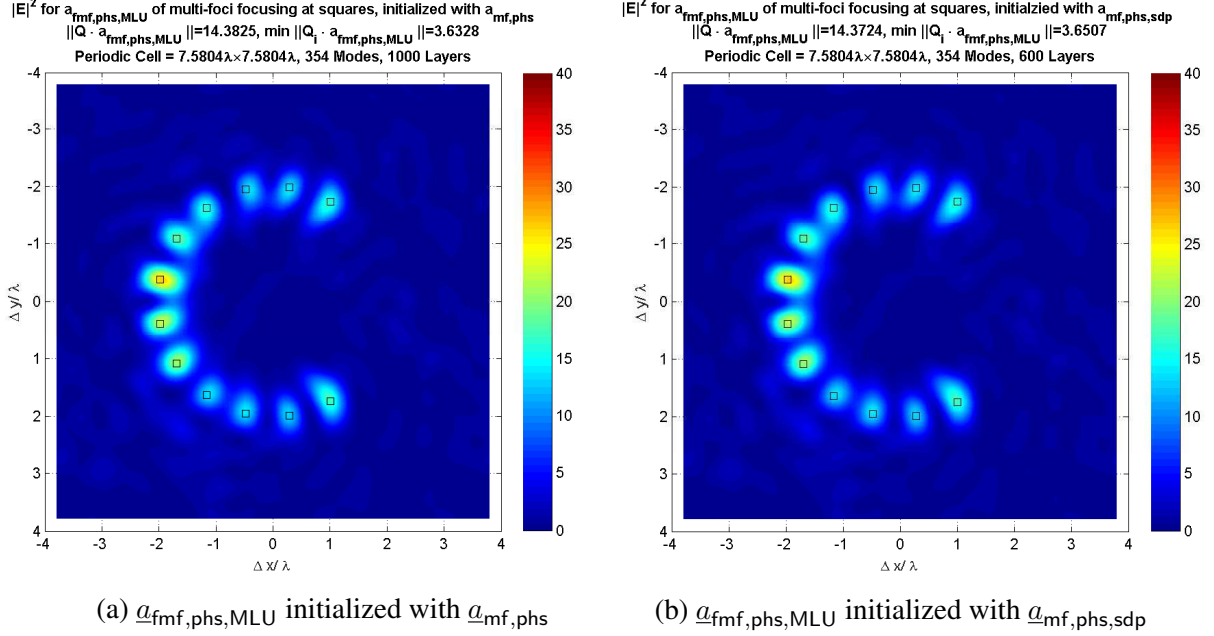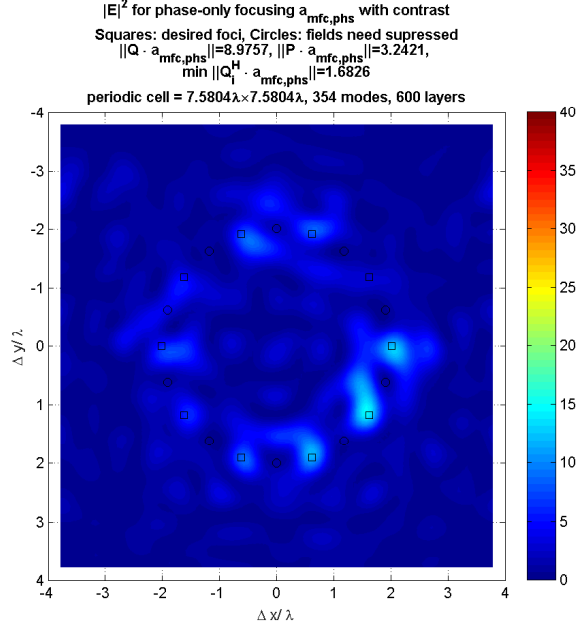
Figure 4.10: Electric field intensity on the $(x, y, 2\lambda)$ plane behind the slab (in Region 2) due to $\underline{a}_{\mathsf{mfc,phs}}$, obtaining $\|Q \cdot \underline{a}_{\mathsf{mfc,phs}}\|_2 = 8.9757$, $\|P \cdot \underline{a}_{\mathsf{mfc,phs}}\|_2 = 3.2421$ and $\min_{i=1,\ldots,q} \|Q_i \cdot \underline{a}_{\mathsf{mf,phs}}\|_2 = 1.6826$.

MLU method. However, for phase-only modulation, the pattern is the other way around: the MLU method does a better job than the bisection search + SDP method.

For contrast focusing, we check the achieved contrast ratio for the optimized wavefronts $\underline{a}_{\mathsf{mfc,phs}}$, $\underline{a}_{\mathsf{mfc,phs,sdp}}$ and $\underline{a}^{\mathsf{rand}}_{\mathsf{mfc,phs,sdp}}$ for phase-only modulation. Figure 4.14a shows the results. Among these methods, $\underline{a}_{\mathsf{mfc,phs,sdp}}$ achieves the maximal contrast ratio on average, but with large uncertainty (variance). For phase-amplitude modulation, the optimized wavefronts, $\underline{a}_{\mathsf{mfc}}$ and $\underline{a}_{\mathsf{fmfc,sdp}}$ always generate nearly zero field intensity at the spots where fields are suppressed, viz., $\|P \cdot \underline{a}^+_1\|_2 \approx 0$. They do so despite the thickness for all realizations of the random media. Hence, their contrast ratios tend to infinity and therefore are not presented in the figure. The fairness of several contrast focusing methods is demonstrated in Figure 4.14b. As shown in the figure, by enforcing the even-intensity condition, fairness reaches a three-fold improvement for phase-amplitude modulated wavefronts and a two-fold improvement in phase-only modulated wavefronts.

(a) $\underline{a}_{\text{mfc,phs,sdp}}$ (b) $\underline{a}^{\text{rand}}_{\text{mfc,phs,sdp}}$
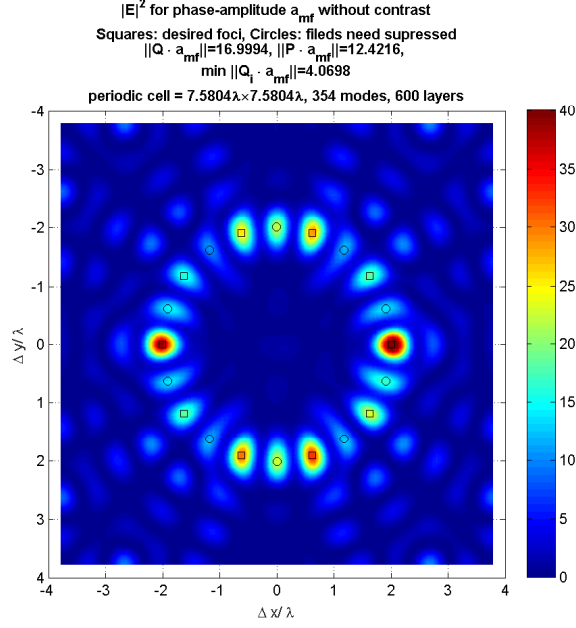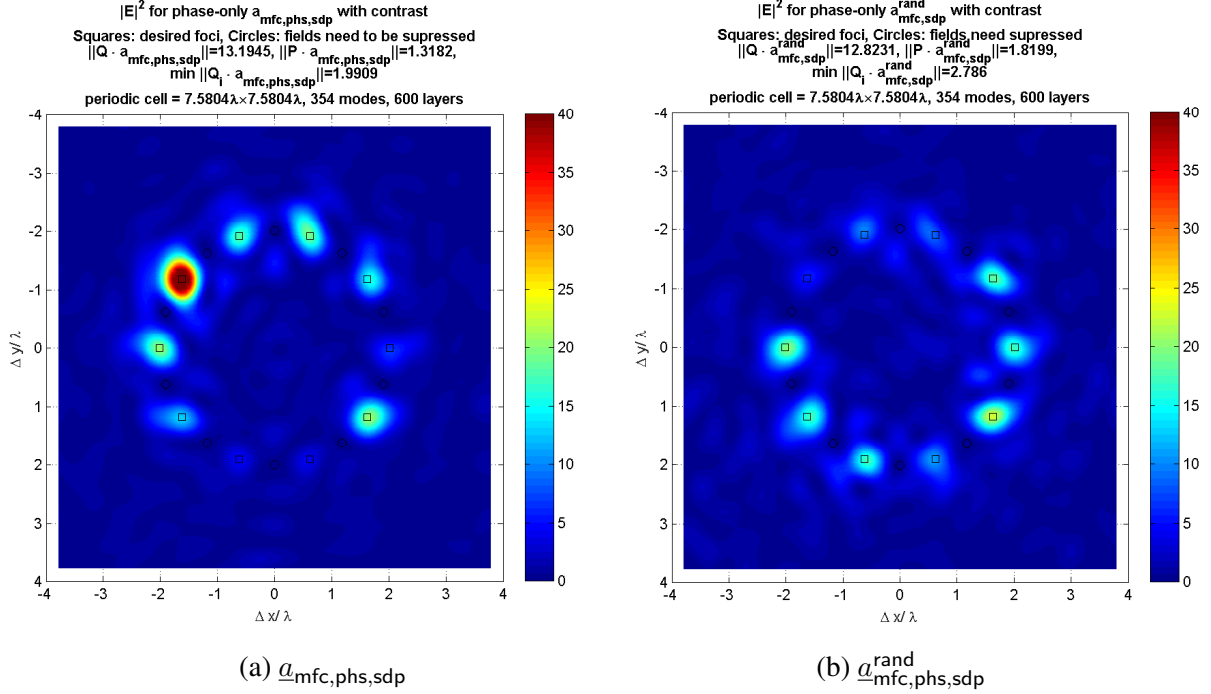
Figure 4.11: Electric field intensity on $(x, y, 2\lambda)$ plane behind the slab (in Region 2) due to (a) $\underline{a}_{\text{mfc,phs,sdp}}$, obtaining $\|Q \cdot \underline{a}_{\text{mfc,phs,sdp}}\|_2 = 13.1945$, $\|P \cdot \underline{a}_{\text{mfc,phs,sdp}}\|_2 = 1.3182$ and $\min_{i=1,\ldots,q} \|Q_i \cdot \underline{a}_{\text{mfc,phs,sdp}}\|_2 = 1.9909$; (b) $\underline{a}^{\text{rand}}_{\text{mfc,phs,sdp}}$, obtaining $\|Q \cdot \underline{a}^{\text{rand}}_{\text{mfc,phs,sdp}}\|_2 = 12.8231$, with $\min_{i=1,\ldots,q} \|Q_i \cdot \underline{a}^{\text{rand}}_{\text{mfc,phs,sdp}}\|_2 = 2.786$ and $\|P \cdot \underline{a}^{\text{rand}}_{\text{mfc,phs,sdp}}\|_2 = 1.8199$.

4.6   Conclusion

This chapter presented a comprehensive set of focusing schemes for creating multiple foci for non-contrast and contrast optimization problems, with a preference for max-total-intensity vs. even-intensity, and for phase-amplitude and phase-only modulators. Numerical results for two focusing arrangements —- "C"-shape foci and circularly arranged foci/suppressing-spots —- demonstrate the efficacies of the proposed schemes. Numerical experiments on focusing/suppressing fields on the circularly arranged spots also demonstrate the necessity of the contrast focusing schemes. When inspecting how the thickness of the random media affects the efficacies of the proposed schemes, we see that they remain performant for very thick media; in our thickness-related study, the thickness of the media was as large as $3.52 \times 10^4 \lambda$, or 8800 periodic layers.

(a) $\underline{a}_{\mathsf{fmfc,phs,sdp}}$
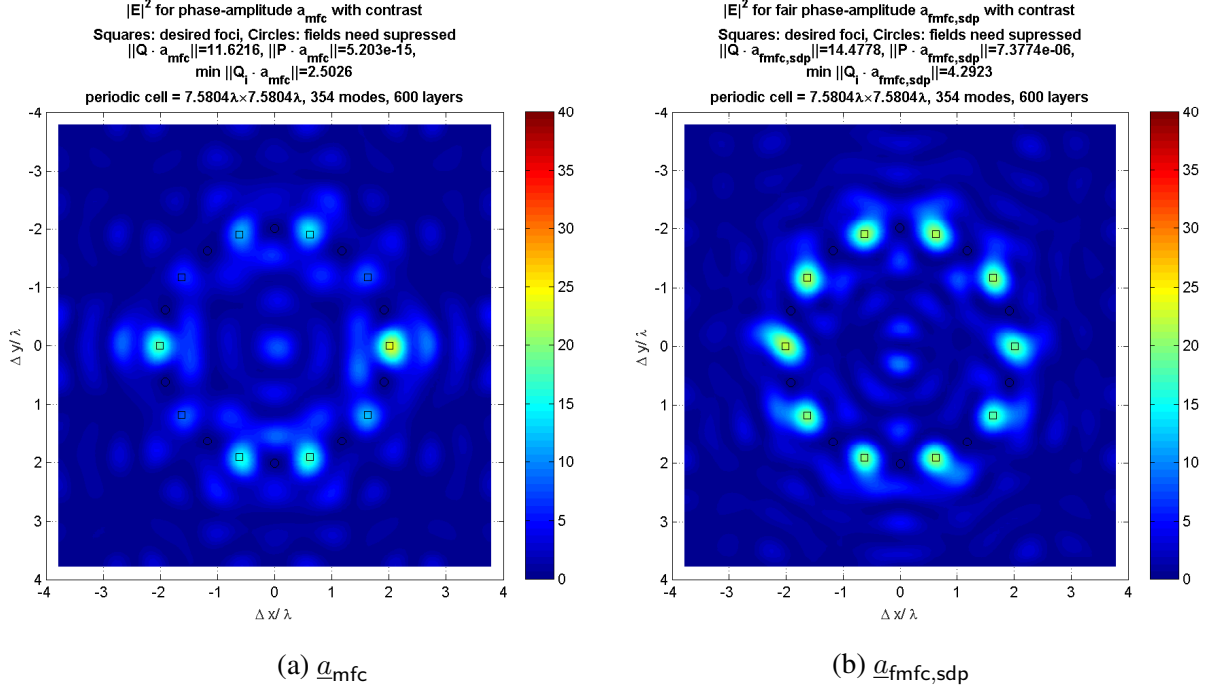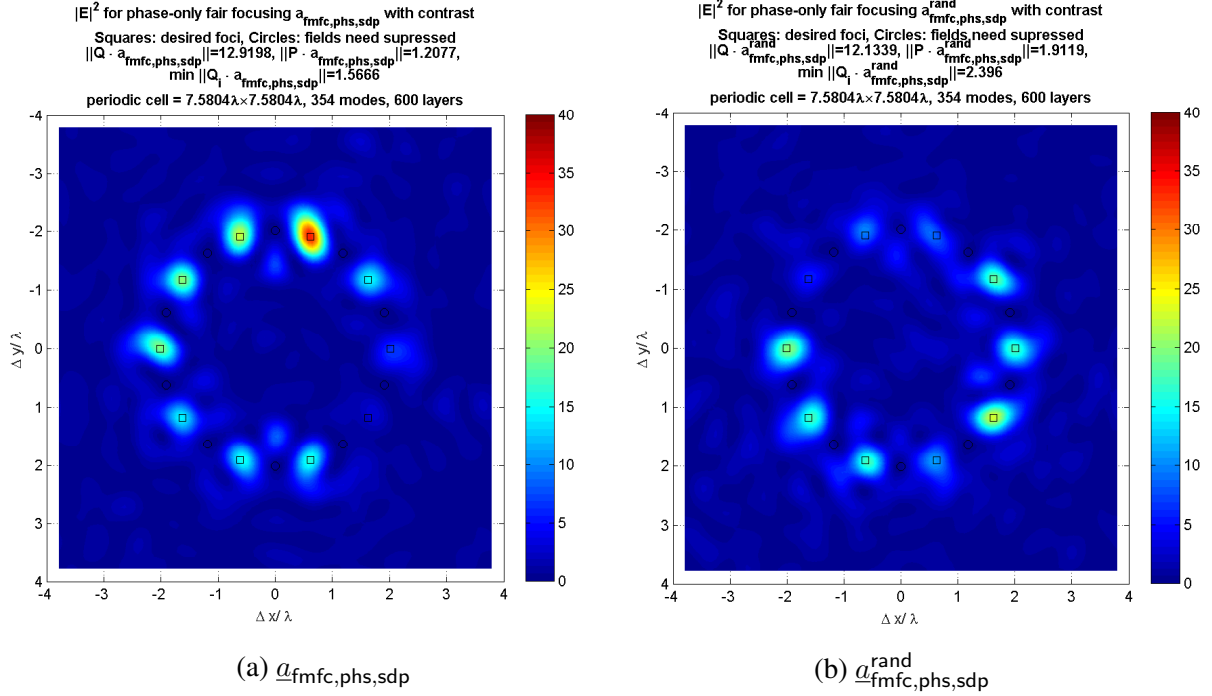
(b) $\underline{a}_{\mathsf{fmfc,phs,sdp}}^{\mathsf{rand}}$

Figure 4.12: Electric field intensity on the $(x, y, 2\lambda)$ plane behind the slab (in Region 2) due to (a) $\underline{a}_{\mathsf{fmfc,phs,sdp}}$, obtaining $\|Q \cdot \underline{a}_{\mathsf{fmfc,phs,sdp}}\|_2 = 12.9198$, $\|P \cdot \underline{a}_{\mathsf{fmfc,phs,sdp}}\|_2 = 1.2077$ and $\min_{i=1,...,q} \|Q_i \cdot \underline{a}_{\mathsf{fmfc,phs,sdp}}\|_2 = 1.5666$; (b) $\underline{a}_{\mathsf{fmfc,phs,sdp}}^{\mathsf{rand}}$, obtaining $\|Q \cdot \underline{a}_{\mathsf{fmfc,phs,sdp}}^{\mathsf{rand}}\|_2 = 12.1399$, $\|P \cdot \underline{a}_{\mathsf{fmfc,phs,sdp}}^{\mathsf{rand}}\|_2 = 1.9119$ and $\min_{i=1,...,q} \|Q_i \cdot \underline{a}_{\mathsf{fmfc,phs,sdp}}^{\mathsf{rand}}\|_2 = 2.396$.
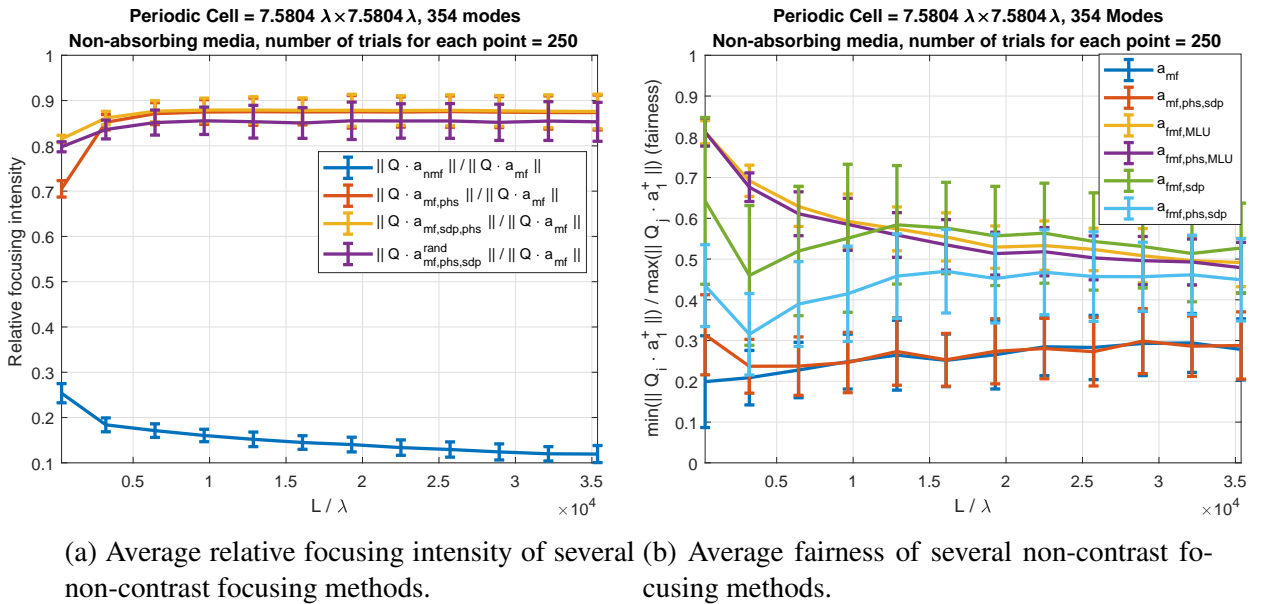
(a) Average relative focusing intensity of several non-contrast focusing methods.

(b) Average fairness of several non-contrast focusing methods.

Figure 4.13: Intensity and fairness inspection for non-contrast focusing methods.
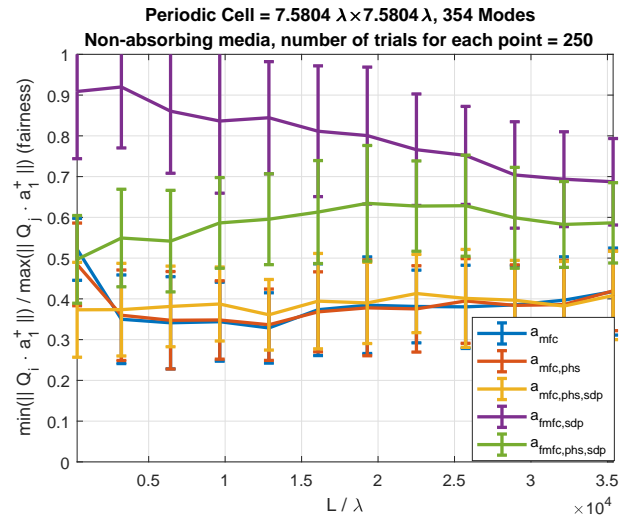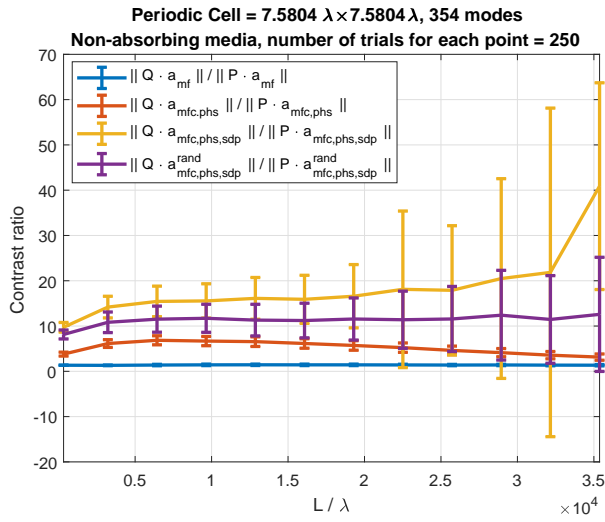
(a) Average contrast ratio of several contrast focusing methods.

(b) Average fairness of several contrast focusing methods.

Figure 4.14: Contrast ratio and fairness inspection for contrast focusing methods.

CHAPTER 5

Methods for Retrieving the Transmission Characteristics of Random Media

5.1 Introduction

Wavefront shaping requires knowledge of the transmission characteristics of the target medium; hence, measuring or computing these characteristics is a prerequisite for further optical applications. Figure 5.1 illustrates a setup for measuring the transmission characteristics of a random media by using an ultrasound transducer. An SLM is used to modulate and send wavefronts to the target medium. In addition, the ultrasonic transducer also sends a wave into the medium to detect the transmitted EM field inside or behind the medium due to the incident wavefront. This transmitted field is linearly related to the incident wavefront; thus, when collecting the information of the transmitted field and the incident wavefront, we are able to estimate the transmission characteristics of that medium along with its linear/algebraic representation, such as the measurement matrix Q defined in Eq. (4.2), or the transmission matrix defined in Eq. (2.25). By manipulating these matrices, we then can find a wavefront that can pass through the medium's open channels, and use the SLM to synthesize such optimized wavefront.

Accurate, efficient, and convenient approaches for measuring the transmitted field and retrieving the transmission characteristics of random media therefore are of great importance to all optical techniques involving wavefront sensing. In this chapter, we introduce
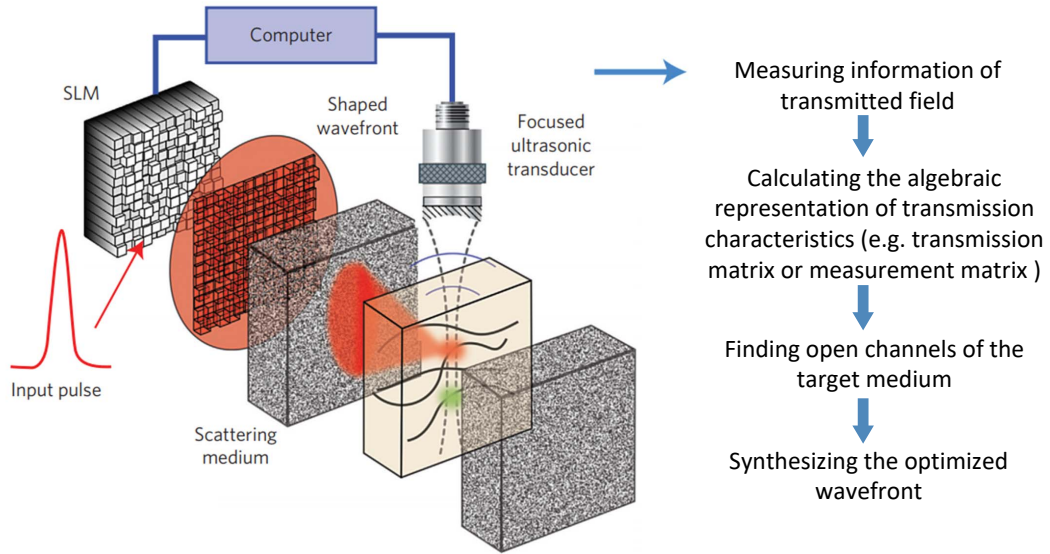
Figure 5.1: Illustration of measuring the transmitted field and retrieving the transmission characteristics of the target media by using an ultrasound transducer. This figure is adopted from [1].

several methods for retrieving the transmission characteristics of the target medium in two scenarios: 1) retrieving the measurement matrix Q through intensity-only field measurement; and 2) retrieving the transmission matrix S_{21} through backscattering analysis. There is an important motivation for retrieving Q via intensity-only measurements: compared to full phase-amplitude measurements of the transmitted field, intensity-only measurements are simpler and can be performed in practice by many off-the-shelf optical devices. Here, we proposed three algorithms: alternating minimization, Phase-Lift, and Phase-Cut. The motivation for retrieving S_{21} via backscattering analysis is that the common ways of measuring the transmitted field are usually inconvenient or invasive; they are particular unsuitable for biomedical applications. These measurement methods require deploying an extra field detector such as the ultrasound transducer illustrated in Figure 5.1, or injecting radiation sources inside the media, such as fluorescent microspheres; by reciprocity, we measure the transmitted field outside the medium due to the sources inside the medium. Therefore, retrieving S_{21} via backscattering analysis has many benefits. Section 5.3 will elaborate on

the mechanics of backscattering analysis. In this category, we propose two algorithms: the alternating minimization and proximal gradient.

5.2 Retrieving the Measurement Matrix Q through Intensity-Only Measurement

The measurement matrix Q defined in Eq. (4.2) is essentially a stack of the coordinate matrices of q measurement spots multiplying the transmission matrix S_{21}. For a given incident wavefront $\underline{a}_1^+$ with matrix Q we obtain the complex amplitudes of transmitted fields as

$$\underline{e}(\boldsymbol{r}_{1:q}) = Q \cdot \underline{a}_1^+. \tag{5.1}$$

Meanwhile, if there are n different incident wavefronts, we have n different transmitted fields as

$$\underbrace{[\underline{e}_1, \ldots, \underline{e}_n]}_{:=E} = Q \cdot \underbrace{\left[(\underline{a}_1^+)_1, \ldots, (\underline{a}_1^+)_n\right]}_{:=A}. \tag{5.2}$$

When $n \geq K_1$ and E can be measured accurately, i.e. when the amplitude and phase of the transmitted field at the q spots can be measured accurately, then retrieving Q is as simple as solving the linear equation

$$Q = E \cdot A^\dagger, \tag{5.3}$$

where $A^\dagger$ is the Moore-Penrose pseudoinverse of A. However, retrieving Q is not straightforward if we can only measure the amplitude (intensity) of the transmitted field; in essence, we can only obtain $|E|$ instead of E. Consider the matrix $\hat{Q}$ which has row-wise phase ambiguity relative to the "true" Q as

$$|E| = |\hat{Q} \cdot A|, \tag{5.4}$$

where

$$\hat{Q} = \begin{bmatrix} e^{j\theta_1} & & \\ & \ddots & \\ & & e^{j\theta_{3q}} \end{bmatrix} \cdot Q. \tag{5.5}$$

$\theta_i, i = 1, \ldots, 3q$ are arbitrary in general. We naturally end up with a phase retrieval problem commonly encountered in many scientific and engineering applications. Here, we propose three algorithms to tackle this problem: *alternating minimization, Phase-Lift, Phase-Cut*.

5.2.1 Alternating Minimization (Retrieving Q)

Alternating minimization (Alt-Min) originates from the pioneering work of Gerchberg [80] and Fienup [81]. Many researchers recently used this algorithm in applications related to signal processing, imaging, and matrix completion [82–85]. This method employs an alternating projection iteratively between the unknown phases of the measurements (phase of the E field) and the unknown underlying vector(s) (measurement matrix $\hat{Q}$). Although there are few theoretical guarantees for the convergence of Alt-Min, this method performs very well empirically. Specifically, by chopping up $\hat{Q}$ row-wisely as

$$\hat{Q} = \begin{bmatrix} \underline{\hat{q}}_1^T \\ \underline{\hat{q}}_2^T \\ \vdots \\ \underline{\hat{q}}_{3q}^T \end{bmatrix} \in \mathbb{C}^{3q \times K_1}, \tag{5.6}$$

and chopping up E^T column-wisely as

$$|E^T| = \begin{bmatrix} |\underline{e}_1|, |\underline{e}_2|, \ldots, |\underline{e}_{3q}| \end{bmatrix} \in \mathbb{R}^{n \times 3q}, \tag{5.7}$$

we obtain the linear equation

$$\text{diag}(|\underline{e}_i|) \cdot \underline{d}_i = A^T \cdot \hat{\underline{q}}_i, \, (i = 1, \ldots, 3q).$$ (5.8)

Here, the $\underline{d}_i$ are the phase unknowns, i.e. they form a $\mathbb{C}^n$ vector with a unit absolute value for each entry. In the following, we omit the subscript i and use $\{\hat{\underline{q}}, |\underline{e}|, \underline{d}\}$ to denote the data/solution set applied to any i-th column/row of the original matrix. Finding $\underline{d}$ and $\hat{\underline{q}}$ means solving the minimization problem

$$\underset{|\underline{d}|=1, \; \hat{\underline{q}}}{\arg\min} \left\| A^T \cdot \hat{\underline{q}} - \text{diag}(|\underline{e}|) \cdot \underline{d} \right\|_2.$$ (5.9)

We note that once $\underline{d}$ is given, solving $\hat{\underline{q}}$ is a standard least square minimization problem. On the other hand, if $\hat{\underline{q}}$ is given, the optimal $\underline{d}$ is determined by $\underline{d} = \exp(j \big/ A^T \cdot \hat{\underline{q}})$. Algorithm 5.1 iteratively refines the solution $\hat{\underline{q}}$ and $\underline{d}$. In practice, initializing $\hat{\underline{q}}^0$ to be the leading

---

Algorithm 5.1 Alternating minimization for finding $\hat{\underline{q}}$

Input: A, $|\underline{e}|$ and $k_{\max}$
Initialize: $\hat{\underline{q}}^0$
for $k = 1 : k_{\max}$ **do**
  $\underline{d}^k := \exp\big(j \big/ A^T \cdot \hat{\underline{q}}^{k-1}\big)$
  $\hat{\underline{q}}^k = (A^T)^\dagger \cdot \overline{\text{diag}(|\underline{e}|)} \cdot \underline{d}^k$
end for
Output: $\hat{\underline{q}} = \underline{q}^{k_{\max}}$

---

eigen-vector of matrix $S = A \cdot \text{diag}(|\underline{e}|^2) \cdot A^T$ helps with convergence.

5.2.2 Phase-Lift

To use the Phase-Lift method, we first reformulate the phase retrieval problem as an optimization problem for finding a rank-one matrix. Specifically, since

$$|\underline{e}|^2 = |A^T \cdot \hat{\underline{q}}|^2 = \text{diag}\big(A^* \cdot A^T \cdot \hat{\underline{q}} \cdot \hat{\underline{q}}^H\big),$$ (5.10)

we can replace $\hat{\underline{q}} \cdot \hat{\underline{q}}^H$ with a Hermitian matrix X of rank one. Therefore, the previous phase retrieval problem is equivalent to the following problem:

$$
\begin{aligned}
\text{find}\ \ & X \in \mathbb{C}^{K_1 \times K_1} \\
\text{subject to}\ \ & \text{diag}\big(A^* \cdot A^T \cdot X\big) = |\underline{e}|^2, \\
& X \succeq 0. \\
& \text{rank}(X) = 1.
\end{aligned}
\tag{5.11}
$$

However, the rank-one constraint is non-convex, turning the above problem in general NP-hard. Therefore, we relax it to a trace minimization problem as

$$
\begin{aligned}
\underset{X \in \mathbb{C}^{K_1 \times K_1}}{\arg\min}\ \ & \text{Tr}(X) \\
\text{subject to}\ \ & \text{diag}\big(A^* \cdot A^T \cdot X\big) = |\underline{e}|^2, \\
& X \succeq 0.
\end{aligned}
\tag{5.12}
$$

This is a canonical convex optimization problem and can be solved efficiently by any SDP solver. After X is found, we proceed with the eigen-decomposition $X = \sum_{i=1}^{K_1} \lambda_i \, \underline{u}_i \cdot \underline{u}_i^H$, and $\hat{\underline{q}} = \sqrt{\lambda_1}\underline{u}_1$ is the approximated solution (or exact solution if $\text{rank}(X) = 1$). The number of required measurements n for obtaining a unique solution is $n = c_0 K_1 \log K_1$, where c_0 is a sufficiently large constant.

5.2.3 Phase-Cut

Similar to the Phase-Lift method, the Phase-Cut method also transforms the phase retrieval problem to a convex optimization problem. In the Phase-Cut method, however, the optimizing variable is the phase of $|\underline{e}|$ instead of the vector $\hat{\underline{q}}$. Starting with Eq. (5.9), if $\underline{d}$ is given, the optimal $\underline{q}$ is given by $\underline{q} = (A^T)^\dagger \cdot \text{diag}(|\underline{e}|) \cdot \underline{d}$. Thus, the phase retrieval problem

is equivalent to

$$\underset{|\underline{d}|=\underline{1}}{\arg\min} \left\| (A^\dagger \cdot A)^T \cdot \text{diag}(|\underline{e}|) \cdot \underline{d} - \text{diag}(|\underline{e}|) \cdot \underline{d} \right\|_2^2, \tag{5.13}$$

Here, the objective function can be rewritten as

$$
\begin{aligned}
&\left\| (A^\dagger \cdot A)^T \cdot \text{diag}(|\underline{e}|) \cdot \underline{d} - \text{diag}(|\underline{e}|) \cdot \underline{d} \right\|_2^2 \\
=&\left\| \left((A^\dagger \cdot A)^T - I \right) \cdot \text{diag}(|\underline{e}|) \cdot \underline{d} \right\|_2^2 \\
=&\underline{d}^H \cdot \text{diag}(|\underline{e}|) \cdot \widetilde{M} \cdot \text{diag}(|\underline{e}|) \cdot \underline{d},
\end{aligned}
\tag{5.14}
$$

where $\widetilde{M} = \left((A^\dagger \cdot A)^T - I \right)^H \cdot \left((A^\dagger \cdot A)^T - I \right)$. By denoting $M = \text{diag}(|\underline{e}|) \cdot \widetilde{M} \cdot \text{diag}(|\underline{e}|)$, the optimization problem becomes

$$
\begin{aligned}
&\underset{\underline{d} \in \mathbb{C}^n}{\arg\min} \ \underline{d}^H \cdot M \cdot \underline{d} \\
&\text{subject to} \ \ |\underline{d}| = \underline{1}.
\end{aligned}
\tag{5.15}
$$

Because $\underline{d}^H \cdot M \cdot \underline{d} = \text{Tr}(M \cdot \underline{d} \cdot \underline{d}^H)$, we replace $\underline{d} \cdot \underline{d}^H$ by a rank-one Hermitian matrix D. Thus, Eq. (5.15) can be restated as

$$
\begin{aligned}
&\underset{D \in \mathbb{C}^{n \times n}}{\arg\min} \ \text{Tr}(M \cdot D) \\
&\text{subject to} \ \ \text{diag}(D) = \underline{1}, \\
&\qquad\qquad\quad D \succeq 0, \\
&\qquad\qquad\quad \text{rank}(D) = 1.
\end{aligned}
\tag{5.16}
$$

By dropping the cumbersome rank-one constraint, we obtain a convex optimization problem:

$$\underset{D \in \mathbb{C}^{n \times n}}{\arg\min} \ \mathrm{Tr}(M \cdot D)$$

$$\text{subject to } \mathrm{diag}(D) = \underline{1}, \tag{5.17}$$

$$D \succeq 0.$$

This problem can be solved by any standard SDP solver. Through the eigen-decomposition $D = \sum_{i=1}^{n} \lambda_i \underline{u}_i \cdot \underline{u}_i^H$, we assign $\underline{e} = \mathrm{diag}(|\underline{e}|) \cdot \exp(j \underline{/u_1})$ yielding the approximate solution

$$\hat{\underline{q}} = (A^T)^\dagger \cdot \underline{e}. \tag{5.18}$$

Similar to the Phase-Lift method, the number of minimal required measurements to obtain a unique solution is $c_0 K_1 \log K_1$, where c_0 is a sufficiently large constant.

5.2.4 Numerical Experiments of Retrieving Matrix Q

The following numerical experiments investigate the accuracy and efficiency of the three proposed methods for retrieving the measurement matrix Q, which is based on a random media model with the parameters $D_x = D_y = 4.16\lambda$, $\ell = 4.0\lambda$ and $N_c = 1,280$. The number of propagating modes in our mode is $K_1 = 114$.

Figure 5.2 shows the average retrieval error as a function of the relative number of measurements n/K_1. The retrieval results are averaged over 250 trials, and each trial represents a sample of the scattering system of the random medium. As expected, when the number of measurements n exceeds the number of modes K_1 by about a factor of five, all three algorithms guarantee accurate retrieval. The errors of the Phase-Lift and the Phase-Cut settle at magnitude of $10^{-6} \sim 10^{-5}$ and $10^{-11} \sim 10^{-10}$, respectively. Meanwhile, the error of the Alt-Min procedure oftentimes reaches machine precision $\sim 10^{-16}$. However, if we proceed with the Alt-Min after the Phase-Lift and the Phase-Cut following their re-

trieval results, their residual error can be quickly eliminated with only a few iterations, as demonstrated in 5.2b.
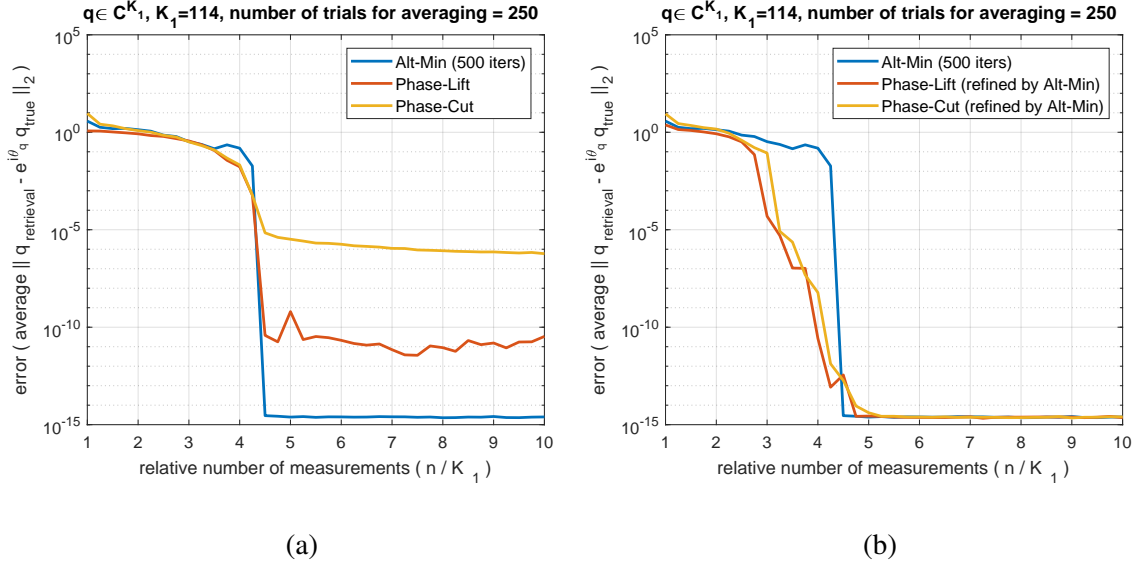
Figure 5.2: The retrieving accuracy of the three methods versus the relative number of measurements n/K_1 for the measurement matrix Q. (a) With the primitive results of Phase-Lift and Phase-Cut; (b) With the refined results of Phase-Lift and Phase-Cut by Alt-Min.

Fig. 5.3 shows a heatmap of a trial indicating the retrieving accuracy of Alt-Min as a function of the relative number of measurements n/K_1 and the number of Alt-Min iterations. There is a threshold for the number of measurements n required for successful retrieval. Below that threshold, the Alt-Min cannot converge and obtain a reasonable result, no matter how many iterations occur. Beyond that threshold, Alt-Min rapidly converges and guarantees accurate retrieval.

Next, we consider a situation in which the measured $|\underline{e}|$ is contaminated by noise $\underline{e}_{\mathrm{noise}}$. Hence, the actual measured field intensity is $|\underline{e}+\underline{e}_{\mathrm{noise}}|$, and the relative noise level is defined as $\|\underline{e}_{\mathrm{noise}}\|_2/\|\underline{e}\|_2$. Figure 5.4a and 5.4b present the heatmap of the retrieval accuracy as functions of the relative number of measurements n/K_1 and relative noise level. As shown in the two figures, when the minimal required number of the measurements is satisfied, the relative retrieval error is approximately at the same level as the noise. Both the Alt-Min and the Phase-Cut are workable in the presence of a wide range of relative noise level from
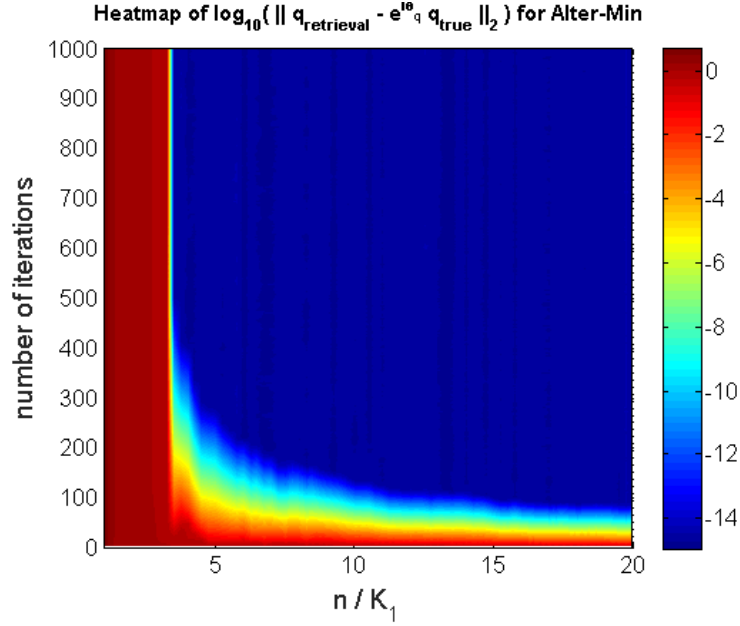
Figure 5.3: Heatmap of the retrieving accuracy of Alt-Min as a function of the relative number of measurement n/K_1 and the number of Alt-Min iterations

10^{-15} to about 10^{-1}; thus, these retrieval methods are noise tolerant. However, Phase-Lift is relatively less noise tolerant. Figure 5.5 shows the maximum noise tolerated by Phase-Lift for successful retrieval. Within the range of tolerated noise, the retrieval accuracy is approximately the same level as the noise.

5.3 Retrieving the Transmission Matrix S_{21} through Backscattering Analysis

In the following sections, we introduce methods for retrieving the transmission matrix S_{21} through backscattering analysis. In principle, S_{21} retrieval requires measuring the transmitted field passing through the random medium. As shown in Figure 5.6, to measure the transmitted field, one needs to deploy an EM field detector, e.g. an ultrasound transducer. Alternatively, we might inject a radiating source inside the medium, which in effect means we measure the transmitted field outside the medium due to a source embedded

(a) Alter-Min (b) Phase-Cut (refined by Alt-Min)
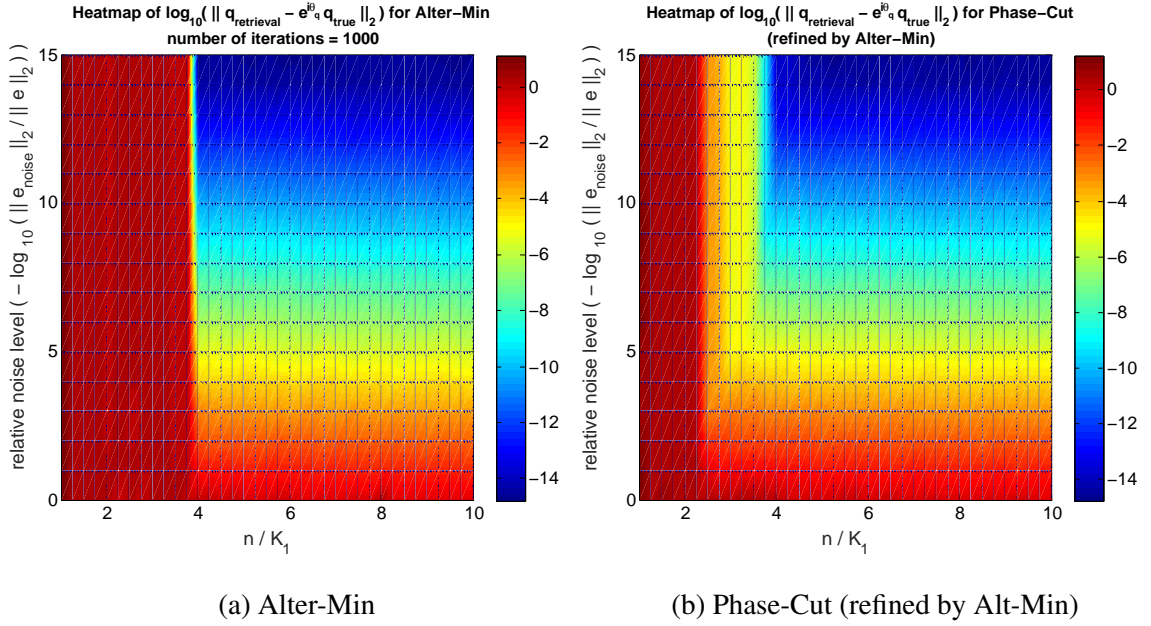
Figure 5.4: The heatmap of the retrieval accuracy as functions of the relative number of measurements n/K_1 and noise level.
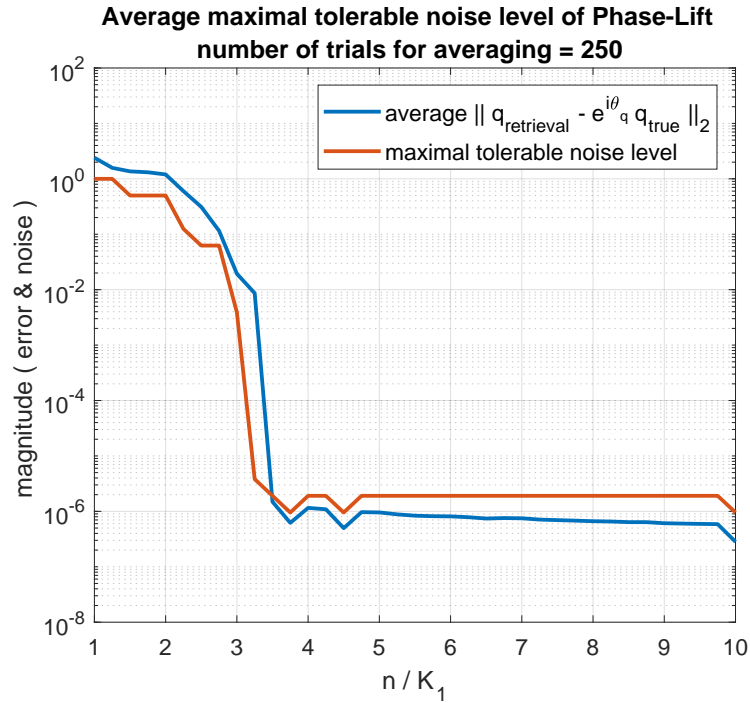
Figure 5.5: The magnitude of maximal tolerated noise of Phase-Lift and the corresponding retrieval accuracy, as a function of the relative number of measurements n/K_1.

within the medium. These measurement methods are either inconvenient or invasive, and are particular unsuitable for biomedical applications. Retrieving S_{21} via backscattering
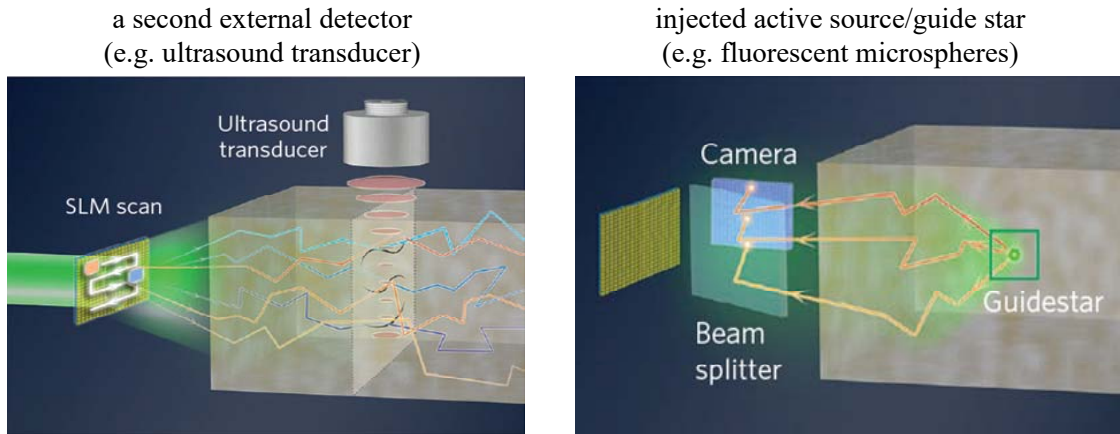
Figure 5.6: Illustration of two traditional methods for measuring the transmitted field passed through a random medium. This figure is adopted from [2].
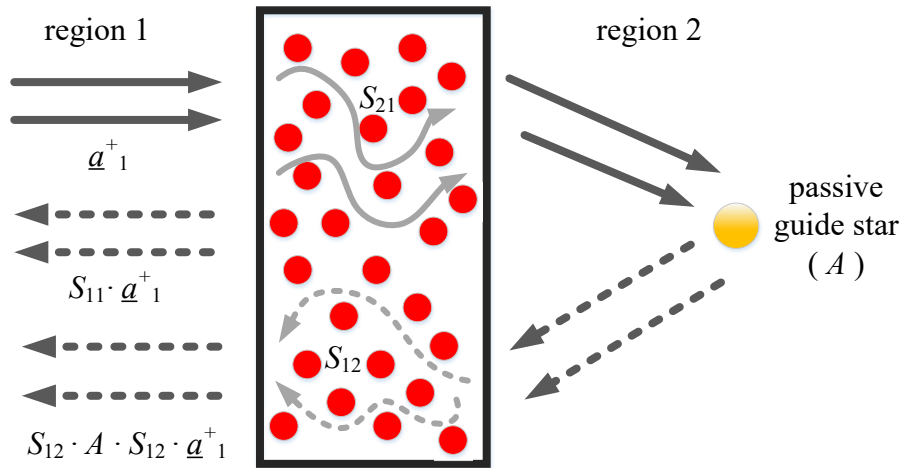
Figure 5.7: Sketch of the scattering system involving a passive guide star, which is utilized to retrieve S_{21} via backscattering analysis.

analysis avoids these inconveniences. Figure 5.7 illustrates the principle of backscattering analysis. The incident wavefront illuminates the medium from Region 1: part of the wave reflects, and part of it passes through the medium and impinges on one or more scatterer(s) with known scattering characteristics. We call these scatterers passive guide stars or simply guide stars, as opposed to so-called active guide stars, such as fluorescent microspheres.

Because these guide stars are not actively radiating, they can be existing tissue (like blood cells),thereby avoiding invasive implantation. The backscattered wave from these guide stars travels back into the medium and finally propagates to Region 1. We intend to retrieve S_{21} by examining the final backscattered wave that makes the roundtrip. Mathematically, we can formulate the path traveled by the incident wavefront as follows. We start from the mediums forward transmission matrix S_{21} (from Region 1 to Region 2) and backward transmission matrix S_{21} (from Region 2 to Region 1) as well as its reflection matrix S_{11}. A guide star is located behind the random medium in Region 2, and has reflection matrix A. By shining an incident wavefront $\underline{a}_1^+$ from Region 1, the total output wavefront observed in Region 2 is

$$\underline{a}_1^- = S_{12} \cdot A \cdot S_{21} \cdot \underline{a}_1^+ + S_{11} \cdot \underline{a}_1^+. \tag{5.19}$$

In practice, obtaining S_{11} is straightforward; we measure the backscattering field if no scatterers are presented in Region 2. Thus, assuming that S_{11} is known, we can extract the backscattered wavefront due to the guide star:

$$\underline{a}_*^- = \underline{a}_1^- - S_{11} \cdot \underline{a}_1^+ = S_{12} \cdot A \cdot S_{21} \cdot \underline{a}_1^+. \tag{5.20}$$

By using the reciprocity $S_{12} = S_{21}^T$, and replacing $\underline{a}_*^-$ and $\underline{a}_1^+$ by $\underline{y}$ and $\underline{x}$, respectively, we obtain

$$\underline{y} = S_{21}^T \cdot A \cdot S_{21} \cdot \underline{x}. \tag{5.21}$$

An extension of Eq. (5.21) involves having multiple independent incident wavefronts $[\underline{x}_1, \underline{x}_2, \ldots, \underline{x}_k]$, and their corresponding backscattering wavefronts $\left[\underline{y}_1, \underline{y}_2, \ldots, \underline{y}_k\right]$ obtained from measurement, leading to the following matrix equation in t the unknown S_{21}:

$$\underbrace{\left[\underline{y}_1, \underline{y}_2, \ldots, \underline{y}_k\right]}_{:=Y} = S_{21}^T \cdot A \cdot S_{21} \cdot \underbrace{\left[\underline{x}_1, \underline{x}_2, \ldots, \underline{x}_k\right]}_{:=X}. \tag{5.22}$$

Furthermore, by using multiple guide stars associated with known reflection matrices $\{A_1, A_2, \ldots, A_n\}$, we can form a system of matrix equations as

$$\begin{cases} Y_1 = S_{21}^T \cdot A_1 \cdot S_{21} \cdot X_1 \\ Y_2 = S_{21}^T \cdot A_2 \cdot S_{21} \cdot X_2 \\ \ldots \ldots \\ Y_n = S_{21}^T \cdot A_n \cdot S_{21} \cdot X_n \end{cases}. \tag{5.23}$$

Here, the $\{X_1, X_2, \ldots, X_n\}$ can either be identical or different. For each (A_i, X_i, Y_i) in Eq. (5.23) and using a sufficient number of independent incident wavefronts which means $k \geq K_1$ we can obtain the matrix $S_{21}^T \cdot A_i \cdot S_{21} = Z_i$ via least squares as

$$S_{21}^T \cdot A_i \cdot S_{21} = Y_i \cdot X_i^\dagger. \tag{5.24}$$

where $X^\dagger$ is the Moore-Penrose pseudo inverse of X. Thus, Eq. (5.23) can be rewritten as follows:

$$\begin{cases} Z_1 = S_{21}^T \cdot A_1 \cdot S_{21} \\ Z_2 = S_{21}^T \cdot A_2 \cdot S_{21} \\ \ldots \ldots \\ Z_n = S_{21}^T \cdot A_n \cdot S_{21} \end{cases}, \tag{5.25}$$

in which Z_i and $A_i, (i = 1, \ldots, n)$ are known, and S_{21} is to be determined. Because Eq. (5.25) is nonlinear in S_{21}, we do not have a direct solution. In the following sections, we propose two methods for solving it.

5.3.1 Alternating Minimization (Retrieving S_{21})

Since Eq. (5.25) is nonlinear, we turn it into an optimization problem with the object function

$$\arg\min_{S_{21}} \sum_{i=1}^{n} \left\| Z_i - S_{21}^T \cdot A_i \cdot S_{21} \right\|_2. \tag{5.26}$$

By replacing S_{21} and S_{21}^T with P and Q, respectively, we can rewrite the object function as

$$\arg\min_{P,Q} \left(\left\| P^T - Q \right\|_2 + \sum_{i=1}^{n} \left\| Z_i - Q \cdot A_i \cdot P \right\|_2 \right). \tag{5.27}$$

In Eq. (5.27), we note that once P is given, we only need to consider the second part of the minimization problem, i.e.

$$\arg\min_{P,Q} \sum_{i=1}^{n} \left\| Y_i - Q \cdot A_i \cdot P \right\|_2, \tag{5.28}$$

and finding the best Q can be cast as a least square problem. Specifically, since

$$\begin{aligned} &\sum_{i=1}^{n} \left\| Y_i - Q \cdot A_i \cdot P \right\|_2 \\ &\geq \left\| \underbrace{\begin{bmatrix} Y_1 & \dots & Y_n \end{bmatrix}}_{:=\hat{Y}} - Q \cdot \underbrace{\begin{bmatrix} (A_1 \cdot P) & \dots & (A_n \cdot P) \end{bmatrix}}_{:=\hat{X}} \right\|_2, \end{aligned} \tag{5.29}$$

the best Q for minimizing the right hand side of Eq. (5.29) is

$$Q = \hat{Y} \cdot \hat{X}^\dagger. \tag{5.30}$$

Assuming that we have enough independent A_i and X_i to guarantee $\mathrm{rank}(\hat{X}) = K_1$. In order to ensure the first part of Eq. (5.27), once Q is solved via least squares minimization, we reduce the discrepancy between P and Q by forming a new P:

$$P := \alpha P + (1 - \alpha) Q^T, \tag{5.31}$$

in which α is a scalar in $(0, 1)$. Then algorithm to solve Eq. (5.27) iteratively is presented in Algorithm 5.2.

In Algorithm 5.2, we only solve the least square minimization problem for Q in each iteration; we therefore call it the unilateral alternating minimization method (UniAlterMin).

Algorithm 5.2 Unilateral alternating minimization (UniAlterMin)

1: Input: backscattering matrices of guide stars $\{A_1 \ \ldots \ A_n\}$
2: Input: measurements $[Y_1 \ \ldots \ Y_n] = \hat{Y}$
3: Input: $\varepsilon = $ termination condition
4: Input: $0 < \alpha < 1$
5: Initialize: P^0
6: $k = 0$
7: **while** Eq. (5.27)$> \varepsilon$ **do**
8: $\quad \hat{X} = \left[(A_1 \cdot P^k) \ \ldots \ (A_n \cdot P^k)\right]$
9: $\quad Q^k = \hat{Y} \cdot \hat{X}^\dagger$
10: $\quad P^{k+1} = \alpha P^k + (1 - \alpha)(Q^k)^T$
11: $\quad k = k + 1$
12: **end while**
13: Output: $P = P^k, Q = Q^k$

However, we can also find the least square solution for P in each iteration. Specifically, if Q is given, we have

$$\sum_{i=1}^{n} \|Y_i - Q \cdot A_i \cdot P\|_2 \geq \left\| \underbrace{\begin{bmatrix} Y_1 \\ \vdots \\ Y_n \end{bmatrix}}_{\hat{Y}} - \underbrace{\begin{bmatrix} Q \cdot A_1 \\ \vdots \\ Q \cdot A_n \end{bmatrix}}_{\hat{X}} \cdot P \right\|_2. \tag{5.32}$$

Then, the best P for minimizing the right hand size of Eq. (5.32) is

$$P = \hat{X}^\dagger \cdot \hat{Y}. \tag{5.33}$$

Combining Eqs. (5.30) and (5.33), we can proceed with the least squares minimization for both Q and P in each iteration to achieve a better convergence speed. Doing so, the bilateral alternating minimization (BiAlterMin) in Algorithm 5.3 emerges.

Algorithm 5.3 Bilateral alternating minimization (BiAlterMin)

1: Input: backscattering matrices of guide stars $\{A_1 \ \ldots \ A_n\}$
2: Input: measurements $[Y_1 \ \ldots \ Y_n] = \hat{Y}_1, [Y_1; \ \ldots; \ Y_n] = \hat{Y}_2$
3: Input: $\varepsilon = $ termination condition
4: Input: $0 < \alpha_1 < 1, 0 < \alpha_2 < 1$
5: Initialize: P^0
6: $k = 0$
7: **while** Eq. (5.27)$> \varepsilon$ **do**
8: $\quad \hat{X}_1 = \left[(A_1 \cdot P^k) \ \ldots \ (A_n \cdot P^k) \right]$
9: $\quad Q' = \hat{Y}_1 \cdot \hat{X}_1^\dagger$
10: $\quad Q^k = (1 - \alpha_2)(P^k)^T + \alpha_2 Q'$
11: $\quad \hat{X}_2 = \left[(Q^k \cdot A_1); \ \ldots; \ (Q^k \cdot A_n) \right]$
12: $\quad P' = \hat{X}_2^\dagger \cdot \hat{Y}_2$
13: $\quad P^{k+1} = \alpha_1 P' + (1 - \alpha_1)(Q^k)^T$
14: $\quad k = k + 1$
15: **end while**
16: Output: $P = P^k, Q = Q^k$

5.3.2 Proximal Gradient

Using basic results from linear algebra, the product of three matrices $B \cdot X \cdot C = Y$ can be reformulated using Kronecker products as

$$B \cdot X \cdot C = Y \Rightarrow (C^T \otimes B) \cdot \text{vec}(X) = \text{vec}(Y), \tag{5.34}$$

where $\text{vec}(*)$ denotes the vectorization of a matrix formed by stacking its columns into a single column vector, and operator $\otimes$ denotes the Kronecker product defined as

$$C^T \otimes B = \begin{bmatrix} c_{1,1}B & c_{2,1}B & \ldots & c_{m,1}B \\ c_{1,2}B & c_{2,2}B & \ldots & c_{m,2}B \\ \vdots & \vdots & \ddots & \vdots \\ c_{1,n}B & c_{2,n}B & \ldots & c_{m,n}B \end{bmatrix}, \tag{5.35}$$

in which C^T is an $n \times m$ matrix and B is a $p \times q$ matrix. Thus, the Kronecker product forms a $np \times mq$ matrix. Based on Eq. (5.34), the linear systems in Eq. (5.25) can be reformed

as follows:

$$\left(S_{21}^T \otimes S_{21}^T\right) \cdot \underbrace{\left[\text{vec}(A_1)\ \text{vec}(A_2)\ \dots\ \text{vec}(A_n)\right]}_{\hat{X}}$$

$$= \underbrace{\left[\text{vec}(Z_1)\ \text{vec}(Z_2)\ \dots\ \text{vec}(Z_n)\right]}_{\hat{Y}}. \tag{5.36}$$

Although Eq. (5.36) is a linear system for $S_{21}^T \otimes S_{21}^T$, we do not intend to solve it directly since its dimension is $K_1^2 \times K_1^2$, which is usually too large for conventional matrix factorization solvers of cubic complexity using limited computational resources. Instead, we translate Eq. (5.36) into an optimization problem and exploit the property of $S_{21}^T \otimes S_{21}^T$ to construct an efficient optimization algorithm.

Although Eq. (5.36) is a linear system regarding $S_{21}^T \otimes S_{21}^T$, we do not intend to solve it directly since its dimension is $K_1^2 \times K_1^2$, which is usually too large for conventional matrix factorization solvers of cubic complexity on a limited computational resource. Instead, we are going to translate Eq. (5.36) into an optimization problem and exploit the property of $S_{21}^T \otimes S_{21}^T$ to construct an efficient optimization algorithm.

First, considering two matrices $B \in \mathbb{C}^{m \times n}$ and $C \in \mathbb{C}^{p \times q}$, we note that the entries of $B \otimes C$ are the distribution of the complete set of elementary product $\{b_{i,j}c_{k,l} | 1 \leq i \leq m, 1 \leq j \leq n, 1 \leq k \leq p, 1 \leq l \leq q\}$, and each product is only presented once in $B \otimes C$. Therefore, $B \otimes C$ has exactly the same elements of that in $\text{vec}(B) \cdot \text{vec}^T(C)$, which is apparently a rank-one matrix. Let $\mathcal{R}(*)$ denote the element rearrangement operator defined by

$$\mathcal{R}(\underbrace{B \otimes C}_{\mathbf{X}}) = \text{vec}(B) \cdot \text{vec}(C)^T. \tag{5.37}$$

According to the definition of the Kronecker product, $\mathbf{X}$ consists of $m \times n$ blocks $X_{i,j} \in$

$\mathbb{C}^{p \times q}(1 \leq i \leq m, 1 \leq j \leq n)$. The precise rearrangement of operator $\mathcal{R}$ is

$$\mathcal{R}(\mathbf{X}) = \begin{bmatrix} X_1 \\ \vdots \\ X_n \end{bmatrix}, X_j = \begin{bmatrix} \text{vec}(X_{1,j})^T \\ \vdots \\ \text{vec}(X_{m,j})^T \end{bmatrix}, (1 \leq j \leq n). \tag{5.38}$$

If $\mathbf{X} = S_{21}^T \otimes S_{21}^T$, then we have $\mathcal{R}(\mathbf{X}) = \text{vec}(S_{21}^T) \cdot \text{vec}(S_{21}^T)^T$, and consequently, $\mathcal{R}(\mathbf{X}) = \mathcal{R}(\mathbf{X})^T$. As a result, let $\mathbf{S}$ be a $K_1^2 \times K_1^2$ matrix; then, $\mathbf{S} = S_{21}^T \otimes S_{21}^T$ is the solution of the following optimization problem:

$$\underset{\mathbf{S}}{\arg\min} \ \left\| \mathbf{S} \cdot \hat{X} - \hat{Y} \right\|_F$$
$$\text{subject to} \quad \mathcal{R}(\mathbf{S}) = \mathcal{R}(\mathbf{S})^T \tag{5.39}$$
$$\text{rank}\big(\mathcal{R}(\mathbf{S})\big) = 1.$$

If for a certain number of guide stars n and associate measurements (viz. the number of columns of $\hat{X}$ and $\hat{Y}$) with $1 < n \ll K_1^2$, we find a $\widetilde{\mathbf{S}}$ satisfying

$$\left\| \widetilde{\mathbf{S}} \cdot \hat{X} - \hat{Y} \right\|_F < \varepsilon, \tag{5.40}$$

and the $\widetilde{\mathbf{S}}$ additionally satisfies the two constraints in Eq. (5.39), we can expect that

$$\left\| \widetilde{\mathbf{S}} - S_{21}^T \otimes S_{21}^T \right\|_F < c\varepsilon, \tag{5.41}$$

where c is a non-negative constant. Hence, the approximate solution $\widetilde{S}_{21}^T$ can be recovered from $\mathcal{R}(\widetilde{\mathbf{S}})$ as

$$\widetilde{S}_{21}^T = \text{mat}(e^{i\theta} \sqrt{\sigma_1} \underline{u}_1)^{K_1 \times K_1} \tag{5.42}$$

Here, σ_1 and $\underline{u}_1$ are the largest singular value and the associate left singular vector of $\mathcal{R}(\widetilde{\mathbf{S}})$. $\text{mat}(*)^{m \times n}$ is the reverse operator of $\text{vec}(*)$ which reshapes the vector into an $m \times n$ matrix

in a column-major order. $e^{i\theta}$ is a phase shift, and θ is estimated by

$$\theta = \frac{1}{2K_1} \sum_{i=1}^{K_1} \left(\angle \underline{v}_{i,1}^* - \angle \underline{u}_{i,1} \right),$$ (5.43)

where $\underline{v}_1^*$ is the conjugate of the largest right singular vector of $\mathcal{R}(\tilde{\mathbf{S}})$ and $\angle_*$ extracts the phase angle of a complex number. It should be noted that $\tilde{S}_{21}^T$ has global $\pm$ sign ambiguity w.r.t. to the "true" S_{21}^T,

Still, solving the optimization problem Eq. (5.39) is not an easy task. One particular difficulty is that the rank-one constraint rank $\text{rank}\big(\mathcal{R}(\mathbf{S})\big) = 1$ is not easy to enforce. Therefore, we relax the rank-one constraint of $\mathcal{R}(\mathbf{S})$ to rank minimization, and then relax it further to its nuclear norm minimization as

$$\text{rank}\big(\mathcal{R}(\mathbf{S})\big) = 1 \xrightarrow{\text{relax}} \arg\min_{\mathbf{S}} \text{rank}\big(\mathcal{R}(\mathbf{S})\big)$$
$$\xrightarrow{\text{relax}} \arg\min_{\mathbf{S}} \|\mathcal{R}(\mathbf{S})\|_*$$ (5.44)

Here, $\|X\|_*$ is the nuclear norm of matrix X, defined as the sum of Xs singular values. The minimization of the nuclear norm is considered to be tightest convex relaxation of the matrix-rank penalty according to recent studies [86]. As a result, the optimization problem in Eq. (5.39) becomes

$$\arg\min_{\mathbf{S}} \quad \frac{1}{2}\left\| \mathbf{S} \cdot \hat{X} - \hat{Y} \right\|_F^2 + \lambda \|\mathcal{R}(\mathbf{S})\|_*$$
$$\text{subject to} \quad \mathcal{R}(\mathbf{S}) = \mathcal{R}(\mathbf{S})^T$$ (5.45)

in which λ is a non-negative weight scalar. We also add a $1/2$ coefficient to the first squared Frobenius norm part as it aids in deriving the proximal gradient algorithm. Despite the slight relaxation, a significant advantage of the optimization problem in Eq. (5.45) compared to Eq. (5.39) is that the former optimization problem is convex, and hence guaranteed to be solvable [72].

The problem in Eq. (5.45) belongs to a larger class of the generic convex optimization problem that can be solved using off-the-shelf SDP solvers, such as CVX [75]. However, we do not intend to solve it in such a generic way due to its high computational cost. The computational complexity of solving $\mathbf{S}$ via CVX is $O(N^{4.5})$, where N here is the dimension of $S_{21}^T \otimes S_{21}^T$, which is K_1^2. Such a high complexity would prevent us from applying the proposed schemes to practical applications even when K_1 is as small, say 100. Therefore, we employ the proximal gradient method [87] for solving Eq. (5.45). Let $f(\mathbf{S}) = \frac{1}{2}\big\|\mathbf{S} \cdot \hat{X} - \hat{Y}\big\|_F^2$ and $g(\mathbf{S}) = \lambda\|\mathcal{R}(\mathbf{S})\|_*$. The iterates of the proximal gradient scheme, denoted by superscript k, take the following form

$$\mathbf{S}^k = \text{prox}_{t_k g}\big(\mathbf{S}^{k-1} - t_k\nabla f(\mathbf{S}^{k-1})\big). \tag{5.46}$$

Here, the proximity function is defined as

$$\text{prox}_{t_k g}(\mathbf{S}') = \arg\min_{\mathbf{S}} \frac{1}{2}\|\mathbf{S} - \mathbf{S}'\|_F^2 + t_k g(\mathbf{S}), \tag{5.47}$$

and the gradient of f is given by

$$\nabla f(\mathbf{S}) = \mathbf{S} \cdot \hat{X} \cdot \hat{X}^H - \hat{Y} \cdot \hat{X}^H. \tag{5.48}$$

The evaluation in Eq. (5.47) corresponds to the singular value thresholding (SVT) operation [88]. Specifically, let $\tilde{\mathbf{S}}^{k-1} = \mathbf{S}^{k-1} - t_k\nabla f(\mathbf{S}^{k-1})$; then,

$$\mathcal{R}(\mathbf{S}^k) = \text{SVT}_{t_k\lambda}\big(\mathcal{R}(\tilde{\mathbf{S}}^{k-1})\big). \tag{5.49}$$

The SVT operator is defined for a given threshold $\tau > 0$:

$$\text{SVT}_\tau(Z) = \sum_i (\sigma_i - \tau)^+ u_i v_i^H, \tag{5.50}$$

Here, $U\Sigma V^H$ is the singular value decomposition of Z with σ_i denoting the ith largest singular value and u_i and v_i denoting the ith columns of U and V. In addition, $(*)^+ = \max(*, 0)$, which sets negative values to zero. The proximal gradient method converges for a constant step-size $t_k = t < 2/\ell$, where ℓ is the Lipschitz constant of ∇f. In the case of Eq. (5.48), $\ell = 2\|\hat{X}\|_2^2$.

Our target solution, $\mathbf{T} = \mathcal{R}(\mathbf{S}) = \mathcal{R}(S_{21}^T \otimes S_{21}^T)$ is exactly rank one if no noise is presented. Thus, the weight coefficient λ needs to be properly set in order to let the SVT approximation converge to the correct optimum, since the minimal nuclear norm of the feasible $\mathbf{T}$ is not necessarily rank-one. Nonetheless, it is very likely to be low-rank. Therefore, an alternative approximation to Eq. (5.47) involves employing the truncated SVD (TSVD) as

$$\mathcal{R}(\mathbf{S}^k) = \text{TSVD}_{r=1}\big(\mathcal{R}(\tilde{\mathbf{S}}^{k-1})\big). \tag{5.51}$$

Here, $\text{TSVD}_r(*)$ stands for the rank-r TSVD operator defined as

$$\text{TSVD}_r(Z) = \sum_{i=1}^{r} \sigma_i u_i v_i^H, \tag{5.52}$$

where σ_i, u_i and v_i are the same as those for the SVT operator. Notably, the TSVD operator is non-convex; thus, by using it, the theoretical convergence of the proximal gradient method is not guaranteed. However, in practice, the proximal gradient almost always converges with the TSVD operator when the target matrix is rank-one.

5.3.3 Numerical Experiments of Retrieving Matrix S_{21}

5.3.3.1 Guide Star Modeling

Usually, the sizes of guide stars are small compared to the wavelength of the operating EM wave; thus, they can be regarded as particle/point scatterers. A spherical symmetric particle scatterer generates isotropic scattering waves in all direction (related to a specific

polarization), irrespective the direction of the incident wave. However, we prefer particle scatterers with substantial variation in scattering amplitudes with direction. Such guide stars are able to provide a set of diverse reflection matrices $\{A_1, A_2, \ldots, A_n\}$ (their S_{11}) upon simple rotation. This diversity of $\{A_1, A_2, \ldots, A_n\}$ is essential for successful S_{21} retrieval. Therefore, we modeled three non-spherical-symmetrical PEC geometries —- a cube, an ellipsoid, and a paraboloid —- to be used as guide stars, as shown in Figure 5.8. Each geometry has 247 possible incarnations obtained through 3D rotation and seven scales defined by their major dimension a. They range between $\lambda/3 \leq a \leq 4\lambda/3$, where λ is the wavelength of the operating EM wave. Thus, we create a set of $5,187$ variants of the guide star. The reflection matrices A of these variants are obtained through the use of MoM as well as the *action and reaction* procedure. This procedure is similar to obtaining the scattering matrix of a system we introduced in Section 2.3.3. When these guide stars are used in a scattering system to retrieve S_{21}, they are put behind the random medium at an arbitrary location. This location arbitrariness adds extra variance to their scattering behaviors. Consequently, we are able to generate an arbitrary number of distinct reflection matrices $\{A_1, A_2, \ldots, A_n\}$ the use in S_{21} retrieval.
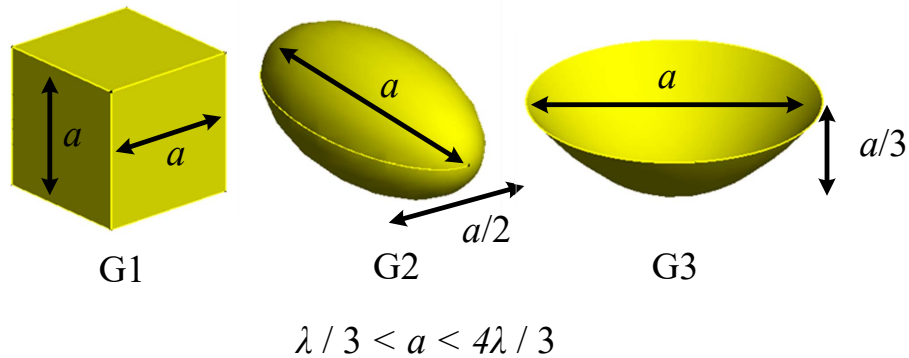

Figure 5.8: Three geometries used as guide stars

5.3.3.2 Using Guide Stars with Unlimited Variants

We first test the proposed retrieval methods by using guide stars modeled from the variants of the three geometries mentioned above. Figure 5.9a and 5.9b demonstrate the

retrieval accuracy as a function of the number of guide stars n in the UniAlterMin and BiAlterMin methods, respectively. In each trial, n guide stars are randomly selected from the guide stars' pool with $5,187$ variants. Because the number of guide star n used for the maximal case ($n = 5K_1$) has not exceed the total number of variants for the three geometries created, these tests involve no repeated use of a guide stars variant in each of the trials. In other words, we have made the reflection matrices $\{A_1, A_2, \ldots, A_n\}$ as diverse as possible; as a consequence, the convergence of the retrieval results for both the UniAlterMin and BiAlterMin method is extraordinarily fast. As shown in the two figures, successful retrieval only requires the number of guide stars n to be more than approximately $1.5K_1$ for UniAlterMin and $1.0K_1$ for BiAlterMin. The retrieval accuracy is reaches machine precision with little uncertainty (very small variance, indicated by the vertical bars), when n satisfies the minimum sample request. We also use the same set of guide stars to test the performance of the proximal gradient method, with similar results shown in Figure 5.10. To guarantee successful successful retrieval, the proximal gradient with TSVD requires fewer guide stars than the SVT.

(a) UniAlterMin   (b) BiAlterMin
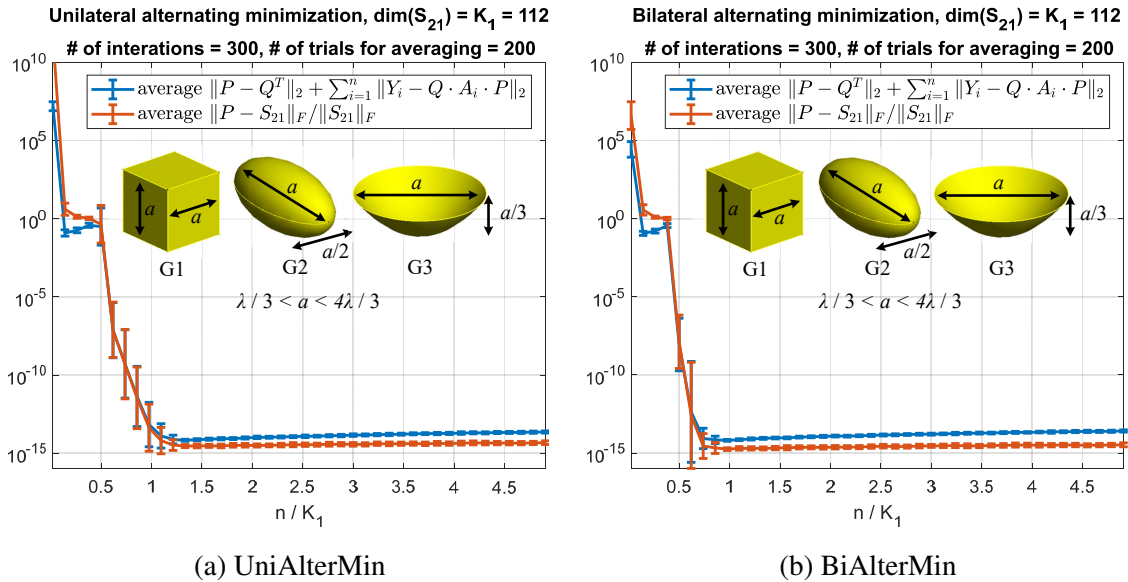
Figure 5.9: Retrieval accuracy as a function of the number of guide stars n in use for alternating minimization methods with unlimited guide star variants.

(a) Proximal gradient with SVT.

(b) Proximal gradient with TSVD.
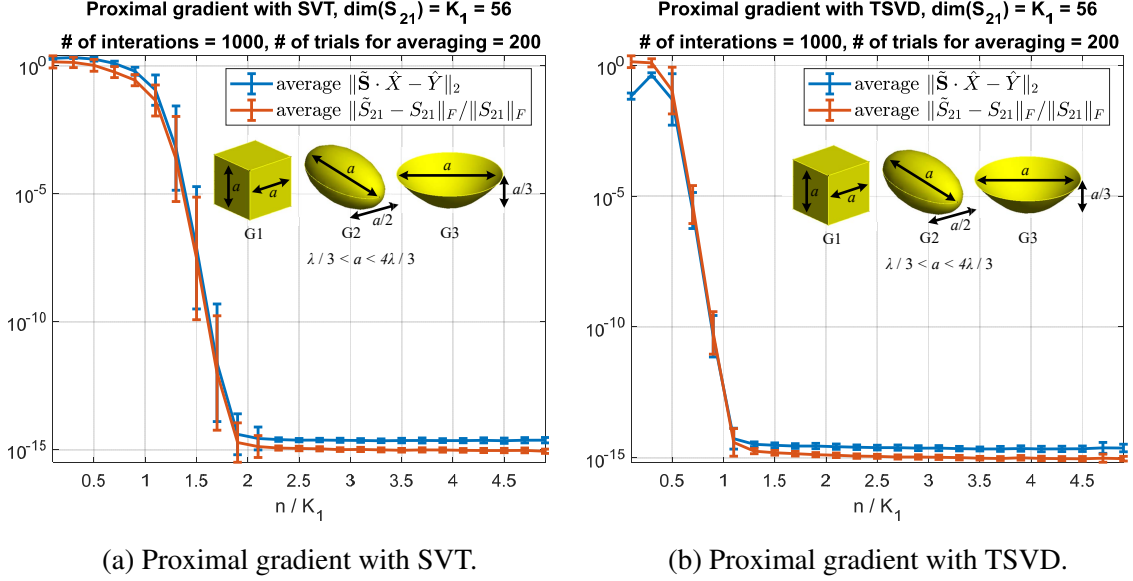
Figure 5.10: Retrieval accuracy as a function of the number of guide stars n in use for proximal gradient methods with unlimited guide star variants.

5.3.3.3 Using Guide Stars with Limited Variants

Because S_{21} retrieval proves to be very successful when using unlimited variants of the guide stars, we wonder about the retrieval performance when guide star variants are limited. Here, we create another geometry –- a corner reflector — to be used as a guide star. Unlike the guide stars in the previous examples, this corner reflector only produces variants through rotation about its central axis, and its concave side always faces (or faces away from) Region 1 (Figure 5.7). If the concave side faces Region 1, the corner reflector reflects waves back directly towards their incoming directions (reflective guide star). On the other hand, if the concave side faces away from Region 1, the corner reflector reflects waves diffusively (diffusive guide star). The length of its edge is fixed at 0.7λ. The rotation along its central axis creates only 68 variants. Hence, when the number of guide stars n used in a trial exceeds the number of variants, some variants are used again though they differ in terms of their location. Figure 5.11 illustrates the use of reflective guide stars, including retrieval performance for all proposed methods. Figure 5.12 show the corresponding results for the case of diffusive guide stars. As can be seen, the use of a

limited set of variants results in a decline of the retrieval accuracy. The average retrieval accuracy can still reach machine precision though the variance is much larger, albeit within an acceptable range. Analysis reveals that diffusive guide stars provide more stable retrieval accuracy with smaller variance compared to reflective guide stars.

(a) UniAlterMin

(b) BiAlterMin

(c) Proximal gradient with SVT

(d) Proximal gradient with TSVD
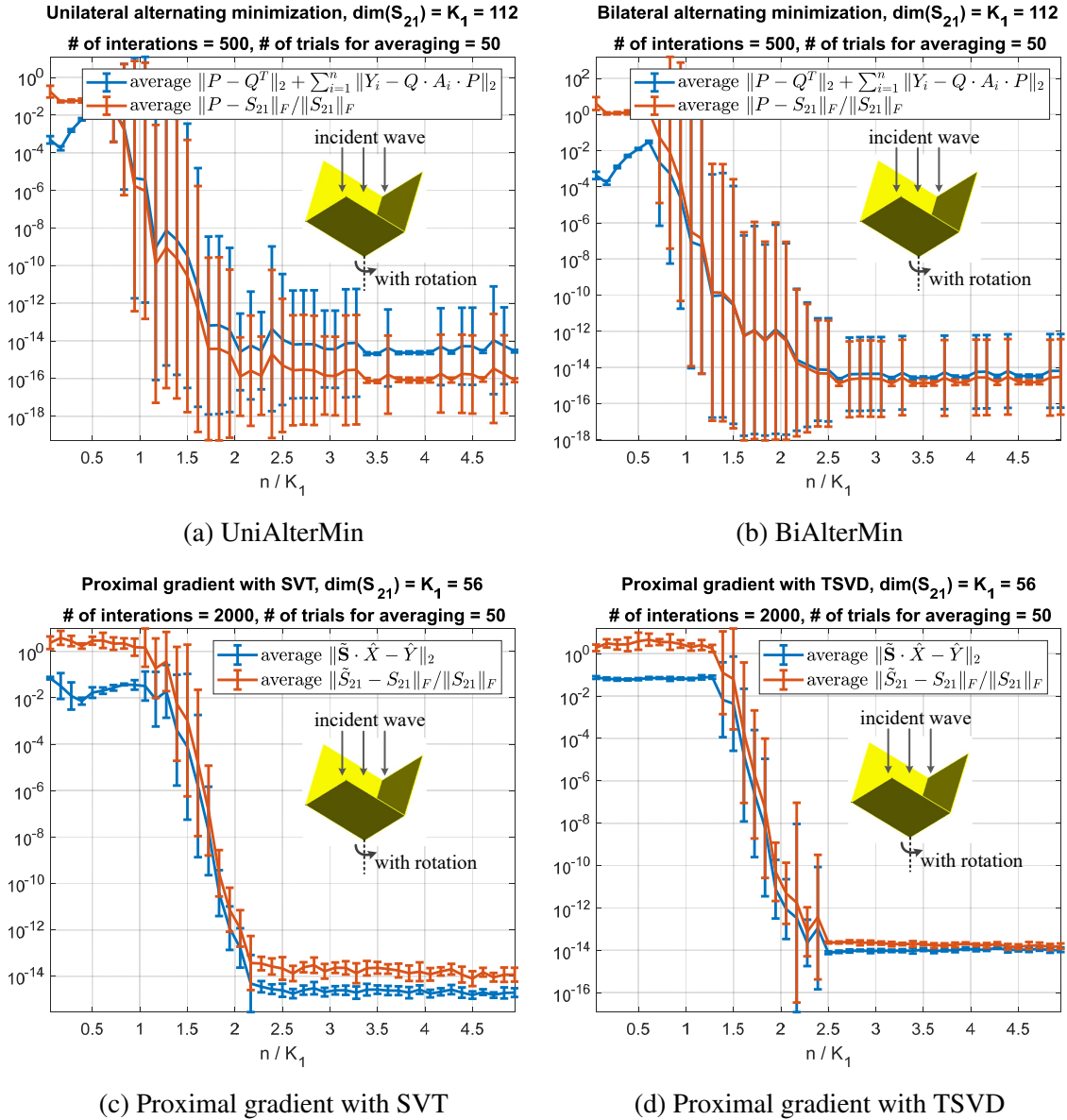
Figure 5.11: Retrieval accuracy as a function of the number of guide stars n in use with limited variants of reflective scattering guide stars.

(a) UniAlterMin

(b) BiAlterMin

(c) Proximal gradient with SVT

(d) Proximal gradient with TSVD
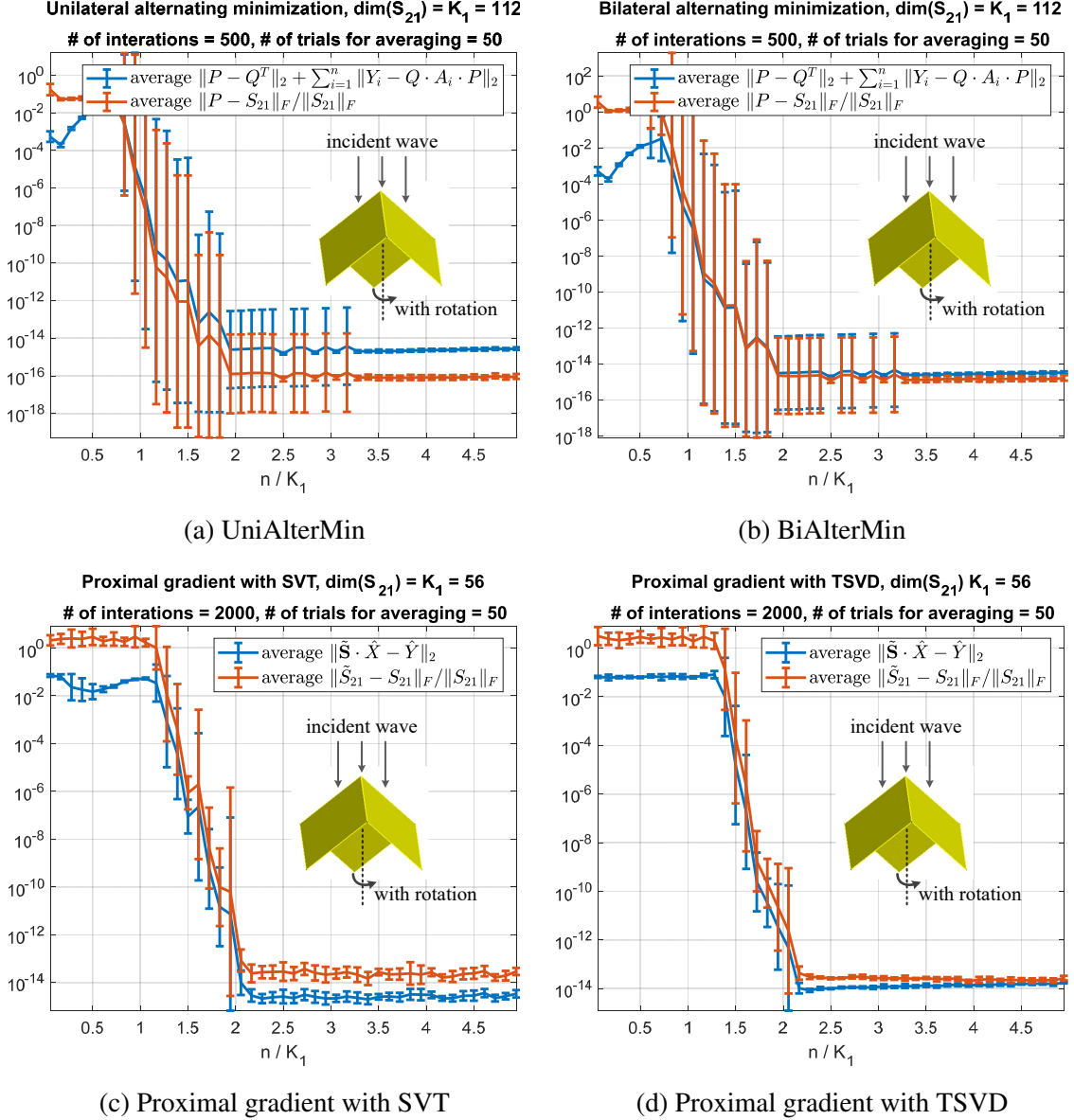
Figure 5.12: Retrieval accuracy as a function of the number of guide stars n in use with limited variants of diffusive scattering guide stars.

5.4 Conclusion

In this Chapter, we proposed three algorithms fl Alt-Min, Phase-Lift and Phase-Cut — for retrieving the measurement matrix Q from intensity-only samples of the transmitted field. Numerical experiments indicate that all algorithms can successfully retrieve the measurement matrix with a minimum number of measurements; in addition, Alter-Min and

Phase-Cut are noise tolerant. We also proposed two algorithms fl alternating minimization tion and proximal gradient — for retrieving the transmission matrix S_{21} via backscattering analysis. The proposed techniques have potential applications in biomedical applications. For S_{21} retrieval, the number of guide stars must exceed a certain minimum, and the diversity of the guide stars also positively relates to successful retrieval. Numerical experiments demonstrate that simple guide stars which perform reflective or diffusive backscattering are capable of providing successful retrieval.

CHAPTER 6

Time Domain Focusing in 3D Random Media

6.1   Introduction

In Chapter 4, we discussed a family of methods that comprehensively tackle the wavefront shaping problem by leveraging eigendecompositions, convex optimization, and bisection search algorithms. However, these wavefront-shaping techniques only exploit the fields spatial degrees of freedom and therefore only yield satisfactory results over a narrow frequency range. In reality, the target may require a pulsating illumination for a specified duration. Here, to accommodate such applications, we develop efficient focusing schemes for transient fields. Specifically, we present a set of schemes for creating a single or multiple pulsating space-time focus/foci. By optimally exploiting the system's temporal degrees of freedom, the proposed schemes achieve even tighter spatial foci than achievable using narrowband signals. The proposed schemes first decompose wideband signals into uncorrelated spectral components, each of which is modulated to construct an optimal single frequency wavefront. Next, leveraging Fourier transform methods, optimal single frequency wavefronts are superimposed to construct foci at desired locations and pre-specified times. Not unlike our previous frequency-domain methods, the new time-domain techniques apply to scenarios that allow for phase/delay-only as well as full phase/delay-amplitude modulation of the incident wavefront. We demonstrate the schemes' abilities to create multiple pulsating asynchronous or simultaneous foci after passing through 3D random media com-

posed of multi-layer periodic slabs.

6.2 Spatial Modulation and Temporal Synthesization

Due to the Nyquist-Shannon sampling theorem, a wideband signal can be perfectly synthesized by superimposing many monochromatic signals. Previously, we have developed a variety of methods that use monochromatic wave to generate focus/foci at specific locations beyond a random medium. Time domain focusing, which requires that the foci occur at pre-specified times in addition to their location specification, is realized via proper superposition of monochromatic waves of different frequencies. Namely, the spatiotemporal (pulsating) focus/foci is generated as a combination of many spatial monochromatic foci. This process is illustrated in Figure 6.1.
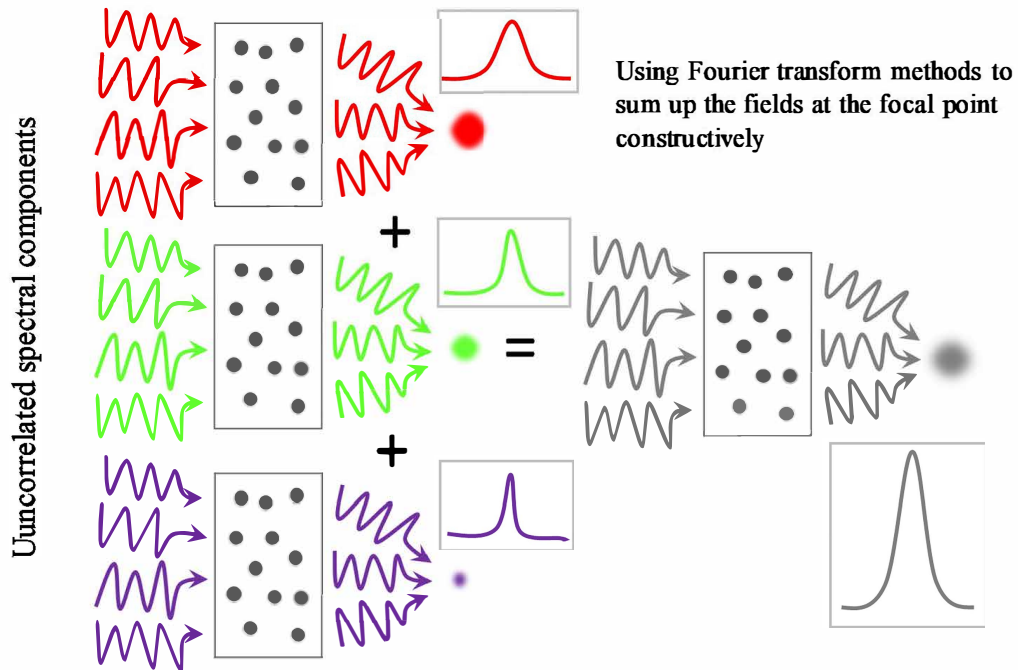

Figure 6.1: The illustration of generating a spatiotemporal focus by combining many spatial monochromatic foci constructively.

6.2.1 Spatial Modulation

We already introduced methods for constructing spatial foci in Chapter 4; here we briefly review the procedure of generating a single focus through phase-amplitude and phase-only modulation. For a given random medium and for operating frequency f_1, we can determine a set of propagating modes and compute the transmitting matrix $S_{21}^{f_1}$. Each propagating mode has a propagation vector $\boldsymbol{k}_i$, and a polarization direction $\hat{\boldsymbol{p}}_i$. Hence, the complex amplitude of the electric field at $\boldsymbol{r}$ behind the random media is the superposition of these propagating modes. Thus, the E field in the x-direction at $\boldsymbol{r}$ is

$$E_x(\boldsymbol{r}) = \sum_i b_i(\hat{\boldsymbol{p}}_i)_x e^{-j\boldsymbol{k}_i \cdot \boldsymbol{r}} = \underline{b}^T \cdot [(\hat{\boldsymbol{p}}_1)_x e^{-j\boldsymbol{k}_1 \cdot \boldsymbol{r}} \quad (\hat{\boldsymbol{p}}_2)_x e^{-j\boldsymbol{k}_2 \cdot \boldsymbol{r}} \quad \dots] = \underline{b}^T \cdot \underline{c}(\boldsymbol{r}), \quad (6.1)$$

where $\underline{b} = [b_1, b_2, \dots, b_i, \dots]^T$ are the modal coefficients on the output side due to an incident wavefront with modal coefficients $\underline{a}$, i.e.

$$\underline{b} = S_{21}^{f_1} \cdot \underline{a}. \tag{6.2}$$

If full phase-amplitude modulation is possible, the amplitude of $E_x(\boldsymbol{r})$ with a normalized incident wavefront can be maximized by constructing $\underline{a}$ as

$$\underline{a}_{\text{foc}}^{f_1}(\boldsymbol{r}) = \frac{\left(\underline{c}^T(\boldsymbol{r}) \cdot S_{21}^{f_1}\right)^*}{\left\|\left(\underline{c}^T(\boldsymbol{r}) \cdot S_{21}^{f_1}\right)^*\right\|_2}. \tag{6.3}$$

If we are restricted to phase-only modulation, then we solve the optimization problem

$$A_{\text{sdp}} = \underset{A \in \mathbb{C}^{M \times M}}{\arg\max} \operatorname{Tr}\left(\underline{b} \cdot \underline{b}^H \cdot A\right)$$

$$\text{subject to } A = A^H, A \succeq 0, \tag{6.4}$$

$$\text{and } A_{ii} = 1/K_1 \text{ for } i = 1, \dots K_1,$$

where K_1 is the number of propagating modes. After solving Eq. (6.4) by SDP, the approximate solution for phase-only modulation is

$$\underline{a}^{f_1}_{\text{pfoc}}(\boldsymbol{r}) = p\Big(\underline{/\text{eig}(A_{\text{sdp}}, 1)}\Big), \tag{6.5}$$

where $\text{eig}(A_{\text{sdp}}, 1)$ is the eigenvector of A_{sdp} associated with the eigenvalue of the largest magnitude. $\underline{/\underline{v}} = \underline{\theta}$ is the operator to take the angle of each complex entry of vector $\underline{v}$, and $p(\underline{\theta})$ is the normalized phase vector of $\underline{\theta}$, defined as

$$p(\underline{\theta}) = \frac{1}{\sqrt{|\underline{\theta}|}} e^{j\theta}, \tag{6.6}$$

where $|\underline{\theta}|$ is the size of vector $\underline{\theta}$. Now, the focused field at $\boldsymbol{r}$ is

$$E^{f_1}_{\text{foc}}(\boldsymbol{r}) = \underline{c}^T \cdot S^{f_1}_{21} \cdot \underline{a}^{f_1}_{\text{foc}}(\boldsymbol{r}), \tag{6.7}$$

or

$$E^{f_1}_{\text{pfoc}}(\boldsymbol{r}) = \underline{c}^T \cdot S^{f_1}_{21} \cdot \underline{a}^{f_1}_{\text{pfoc}}(\boldsymbol{r}). \tag{6.8}$$

We can further normalize the magnitude of the focus to 1.0 by rescaling the incident wavefront as

$$\hat{\underline{a}}^{f_1}_{\text{(p)foc}}(\boldsymbol{r}) = \frac{\underline{a}^{f_1}_{\text{(p)foc}}(\boldsymbol{r})}{E^{f_1}_{\text{(p)foc}}(\boldsymbol{r})}. \tag{6.9}$$

One aspect of the above procedure to note is that it is only meaningful at higher frequencies. When the frequency is very low, the number of propagating modes is small and their wavelength is large, and the system possesses too few degrees of freedom to produce uneven field intensity in space.

6.2.2 Temporal Synthesization

By repeating spatial modulation, we can construct focused fields $\{E^{f_1}_{\text{(p)foc}}(\boldsymbol{r}), E^{f_2}_{\text{(p)foc}}(\boldsymbol{r}), \dots,$ $E^{f_i}_{\text{(p)foc}}(\boldsymbol{r}), \dots\}$ for a given location $\boldsymbol{r}$ at pre-specified operating frequencies f_i, and the corresponding incident wavefronts $\{\hat{\underline{a}}^{f_1}_{\text{(p)foc}}(\boldsymbol{r}), \hat{\underline{a}}^{f_1}_{\text{(p)foc}}(\boldsymbol{r}), \dots, \hat{\underline{a}}^{f_1}_{\text{(p)foc}}(\boldsymbol{r}), \dots\}$. Essentially, each focused field $E^{f_i}_{\text{(p)foc}}(\boldsymbol{r})$ is a sinusoidal function in the time domain, i.e.

$$E^{f_i}_{\text{(p)foc}}(\boldsymbol{r}, t) = E^{f_i}_{\text{(p)foc}}(\boldsymbol{r}) e^{j2\pi f_i t}, \tag{6.10}$$

and therefore we can use them collectively to synthesize a temporal pulse at $\boldsymbol{r}$. Again, two things should be noted: 1) For different frequencies f_i, the number of propagating modes and their propagating directions are different; 2) There should be enough high frequency components to make "focusing" possible.

The procedure for constructing a pulse is as follow:

1. Choose a desired pulse function $x(t)$, produce temporal samples $x(t_{1:n})$ and compute its discrete Fourier transform $X(f_{1:n})$;

2. Compute the modal coefficients of the focused incident wavefronts at $\boldsymbol{r}$ for frequencies $\{f_1, f_2, \dots f_i, \dots\}$, i.e. $\{\hat{\underline{a}}^{f_1}_{\text{(p)foc}}(\boldsymbol{r}), \hat{\underline{a}}^{f_2}_{\text{(p)foc}}(\boldsymbol{r}), \dots, \hat{\underline{a}}^{f_i}_{\text{(p)foc}}(\boldsymbol{r}), \dots\}$;

3. Send the synthetic incident wavefronts $X(f_1) \cdot \hat{\underline{a}}^{f_1}_{\text{(p)foc}}(\boldsymbol{r})$, $X(f_2) \cdot \hat{\underline{a}}^{f_2}_{\text{(p)foc}}(\boldsymbol{r})$, $\dots$, $X(f_i) \cdot$ $\hat{\underline{a}}^{f_i}_{\text{(p)foc}}(\boldsymbol{r})$, $\dots$ into the medium, and evaluate the complex amplitudes of the electric field behind the medium at different locations $E(\boldsymbol{r}', f)$ for $f = f_1, f_2, \dots, f_i, \dots$;

4. For validation, compute the electrical field in the time domain $E^{TD}(\boldsymbol{r}', t_{1:n})$ via inverse discrete Fourier transform $E(\boldsymbol{r}', f_{1:n}) \rightarrow E^{TD}(\boldsymbol{r}', t_{1:n})$. A pulsating focus is expected at $\boldsymbol{r}' = \boldsymbol{r}$.

If multiple pulses $x_1(t), x_2(t), \dots, x_j(t), \dots$ at different locations $\boldsymbol{r}_1, \boldsymbol{r}_2, \dots, \boldsymbol{r}_j, \dots$, need to be generated, we construct the incident wavefront as the sum of the synthetic wave-

front for each pulse as

$$\underline{a}^{f_i}_{(\text{p})\text{mfoc}} = \sum_j X_j(f_i) \cdot \underline{\hat{a}}^{f_i}_{(\text{p})\text{foc}}(\boldsymbol{r}_j),\tag{6.11}$$

for each operating frequency f_i in Step 3. For phase-only modulation, the aggregate wave-front need to be constructed as

$$\underline{a}^{f_i}_{\text{pmfoc}} := \|\underline{a}^{f_i}_{\text{pmfoc}}\|_2 \cdot p\left(\angle \underline{a}^{f_i}_{\text{pmfoc}}\right).\tag{6.12}$$

6.3 Numerical Simulation

We consider a random medium with periodic lattice $D_x = D_y = 9.54361\,m$ and $12,800$ periodic layers. The vertical distance between each layer is $4.0\,m$. The sampling frequency in the time domain is 600 MHz. The total number of samples is $1,001$. Thus, there are 500 even frequency components from 0 to 300 MHz. The number of propagating modes ranges from 2 to 586 for different frequencies. A Sinc function $x(t) = |a|\text{sinc}(\omega t)$ ($\omega = 5 \times$
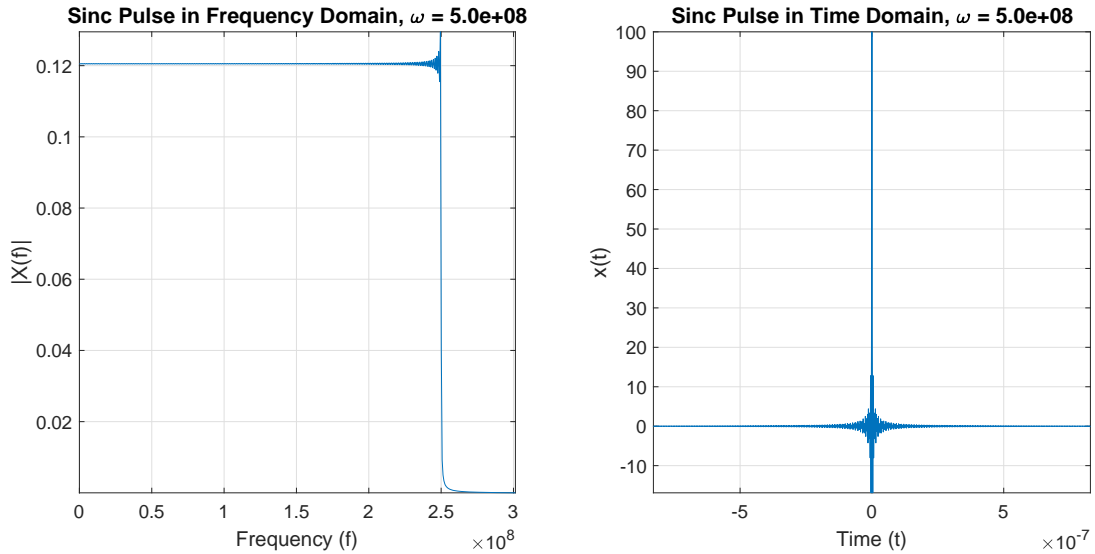

Figure 6.2: The Sinc pulse $x(t) = |a|\text{sinc}(\omega t)$.

$10^8, |a| = 100.0$) and a Gaussian function $x(t) = |a|e^{-t^2/(2\sigma^2)}$ ($\sigma = 2 \times 10^{-9}, |a| = 100.0$) are chosen for the temporal waveforms.
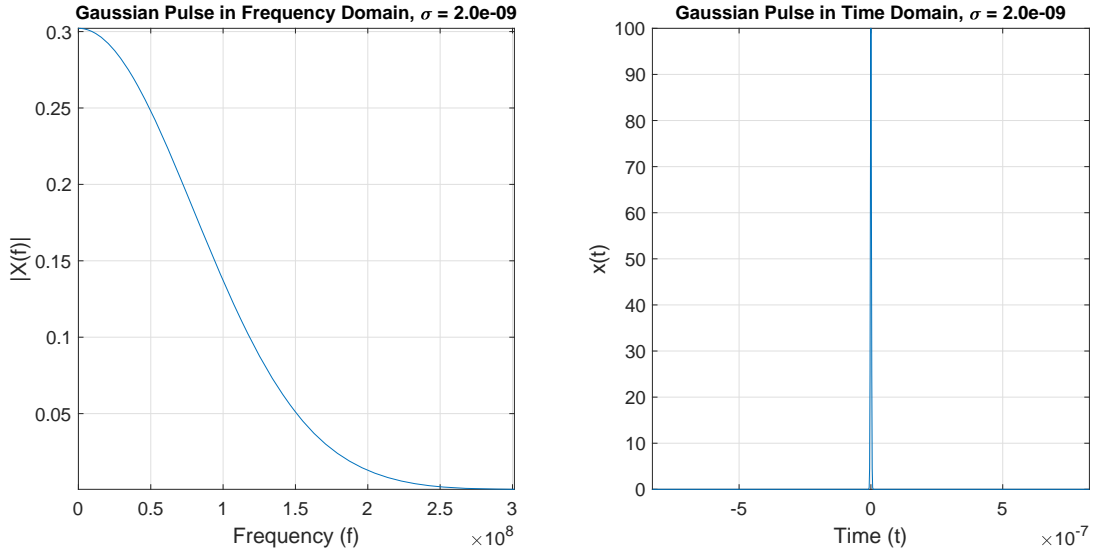
Figure 6.3: The Gaussian pulse $x(t) = |a|e^{-t^2/(2\sigma^2)}$.

Figure 6.4 illustrates a of single pulsating focus that peaks at $t = 0.0$ and location $(0, 0, 2\lambda)$ behind the medium. Phase-amplitude modulated Sinc and Gaussian pulses, as well as a phase-only modulated Gaussian pulse are used, respectively. We can see that the Sinc pulse is more spatially concentrated. This is because the Since pulse contains more high-frequency wave fields than the Gaussian one, which enables constructive interference at finer spatial scales.

Figure 6.5 illustrates the occurrences of first 5 of 5×5 asynchronous foci evenly distributed on the $(x, y, 2\lambda)$ plane behind the medium. The foci are generated by either Sinc or Gaussian pulses, and created by either phase-amplitude or phase-only modulation.

Figure 6.6 illustrates the occurrences of a 2×2 grid synchronous foci evenly distributed on the $(x, y, 2\lambda)$ plane behind the medium. The foci are either generated by Sinc or Gaussian pulses, created by phase-amplitude modulation. The wave field produced by Sinc pulses has better resolution than that due to Gaussian ones.

Since phase-only modulation techniques are less effective for focusing than phase-amplitude modulation methods, when synthesizing using the same pulse, the phase-only modulated incident wavefront needs to be more intense than its phase-amplitude counter-

(a) Sinc pulse from phase-amplitude modulation.

(b) Gaussian pulse from phase-amplitude modulation.

(c) Gaussian pulse from phase-only modulation.
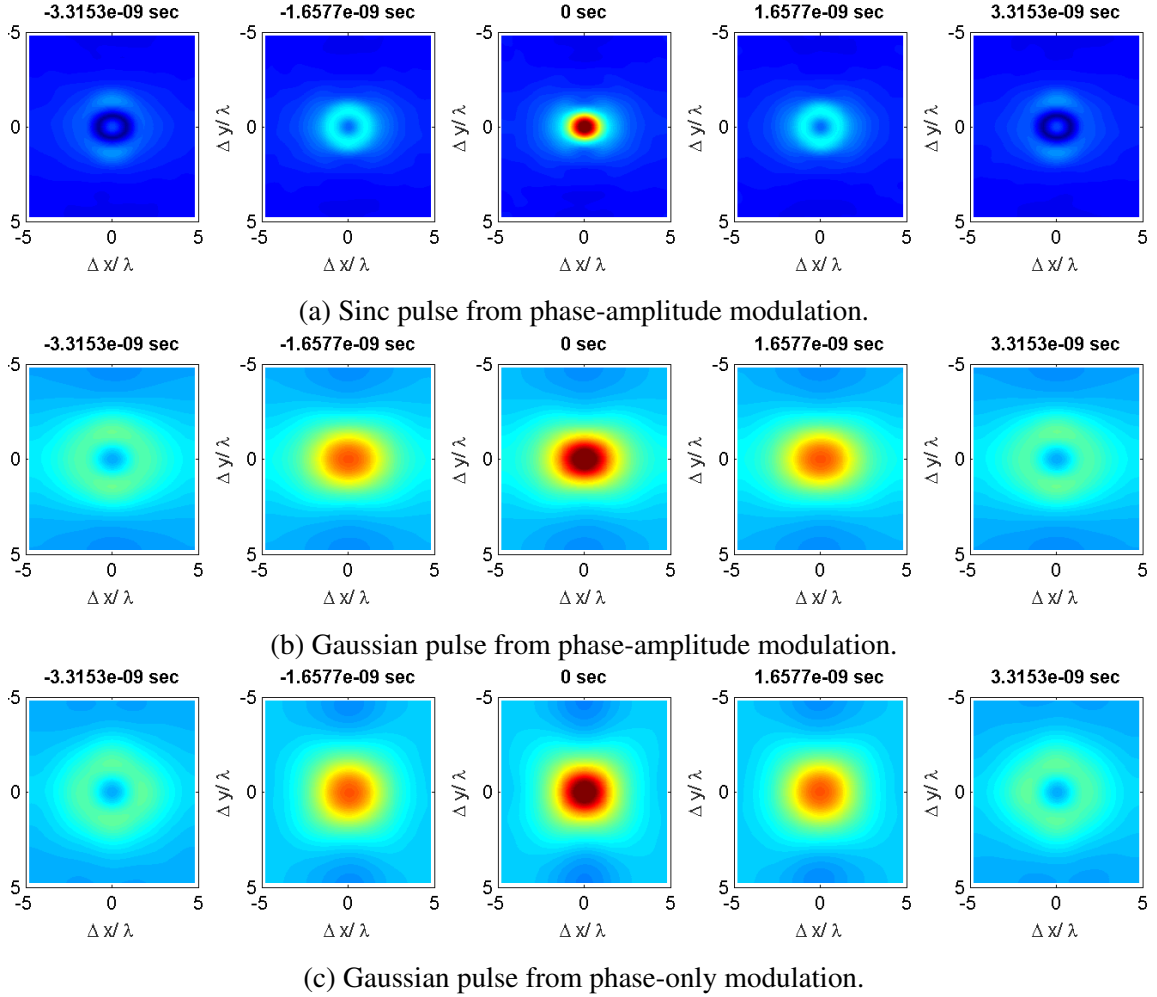
Figure 6.4: The occurrence of one pulsating focus at the center of the target plane.

part. Figure 6.7 shows the difference of power required by phase-amplitude and phase-only modulation for synthesizing using the same single Sinc pulse and single Gaussian pulse.

When generating multiple pulses as the previous example of 5×5 asynchronous Sinc pulses, the result of phase-amplitude modulation are more likely to preserve the amplitudes of the prescribed pulses, as illustrated in Figure 6.8.

6.4 Conclusions

In this chapter, we presented a method for generating pulsating foci for a the wave field passing through random media by leveraging Fourier transform methods, which can
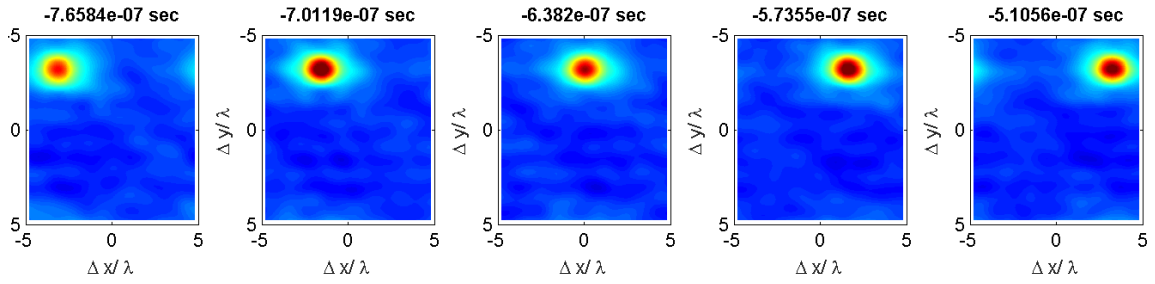
(a) Sinc pulse from phase-amplitude modulation.
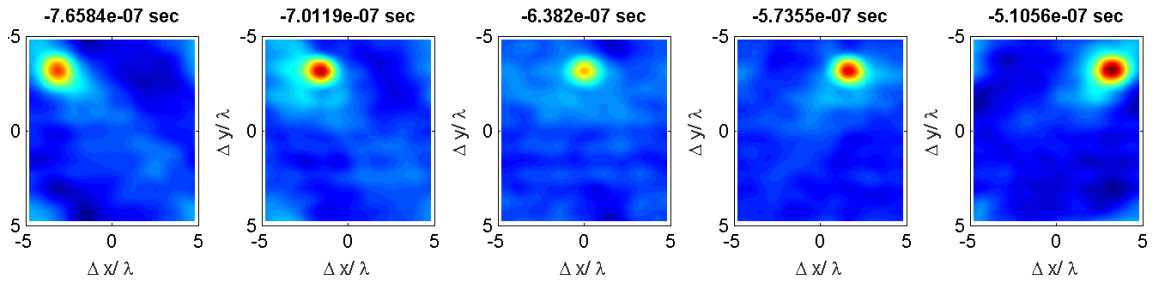
(b) Sinc pulse from phase-only modulation.
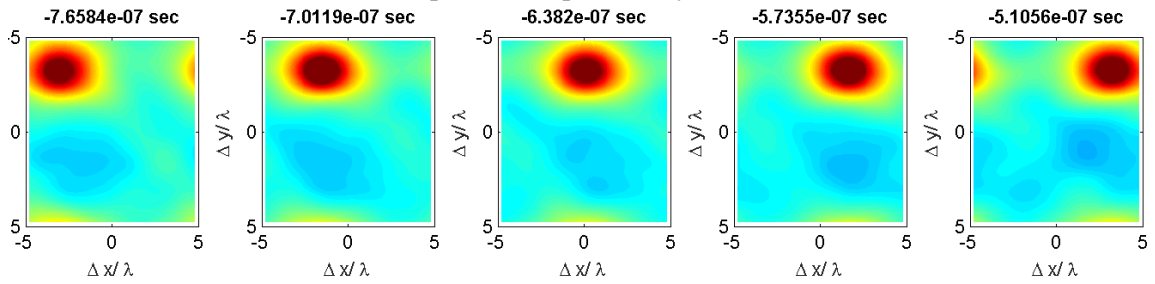
(c) Gaussian pulse from phase-amplitude modulation.
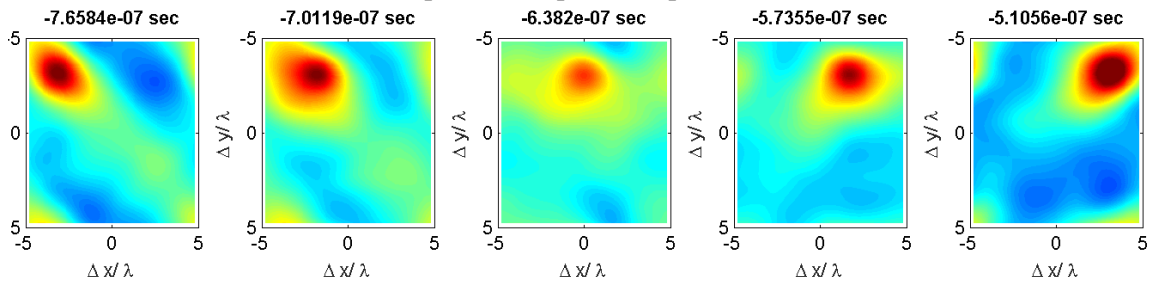
(d) Gaussian pulse from phase-only modulation.

Figure 6.5: The occurrences of first 5 of 5×5 asynchronous foci evenly distributed on the target plane.

be used in applications requiring transient illumination with an additional advantage of forming tighter spatial foci than achievable using narrowband signals. This technique is versatile in that multiple foci can be created at desired locations and pre-specified times, by using either phase-only or full phase-amplitude SLMs.

(a) Sinc pulse from phase-amplitude modulation.

(b) Gaussian pulse from phase-amplitude modulation.

Figure 6.6: The occurrence of synchronous 2×2 foci on the target plane.
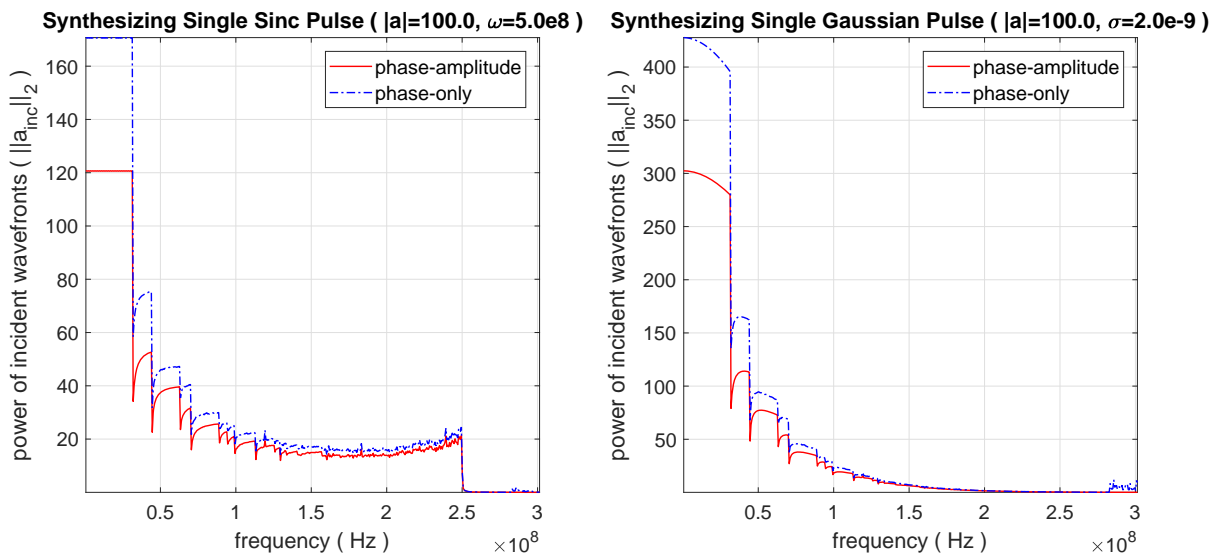
Figure 6.7: Comparison of the power consumption for synthesizing the same pulse
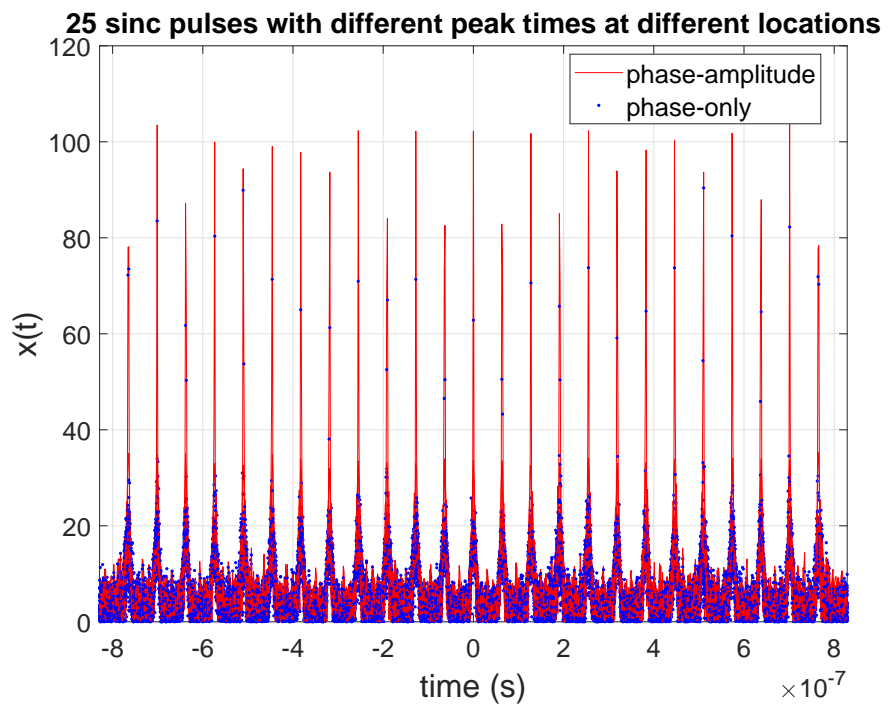
Figure 6.8: The obtained amplitudes of the 25 Sinc pulse with equally prescribed amplitude of $|a| = 100.0$.

<center>**CHAPTER 7**</center>

Transmission Properties of Absorbing Random Media

7.1   Introduction

As we know, random media typically hinder the passage of EM waves by two distinct mechanisms: backscattering and absorption. For ideal non-absorbing r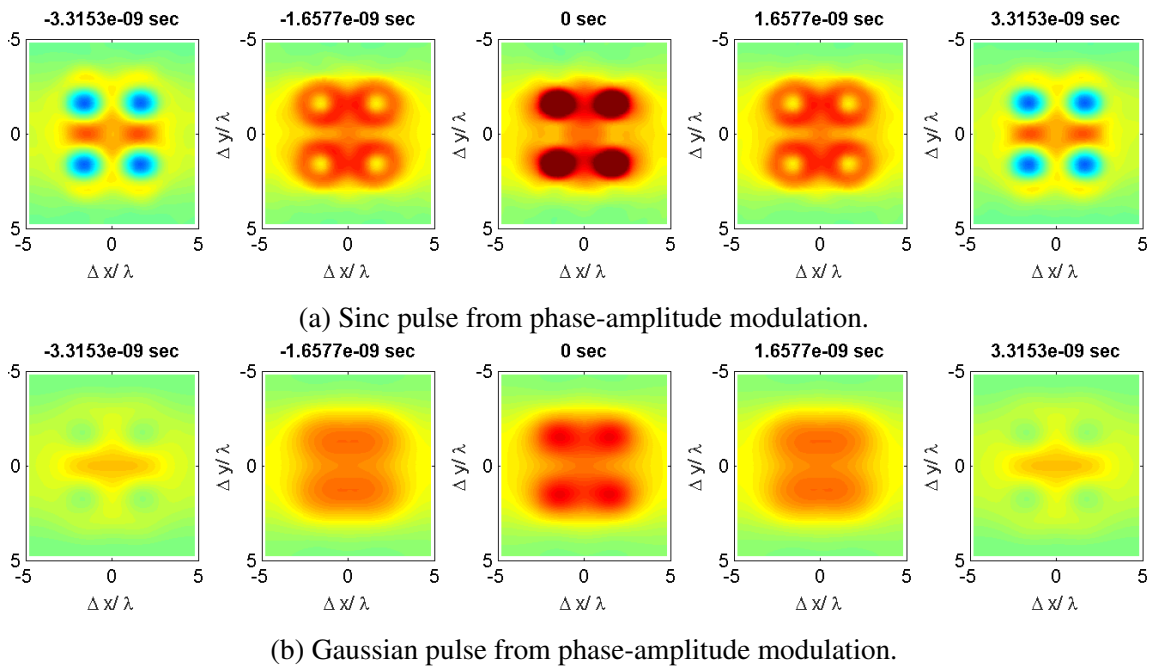andom media with strong backscattering, previous theoretical and experimental developments suggest that their EM transmission coefficients conform to the DMPK distribution [38–41, 63], thereby predicting the existence of a few highly transmitting eigen-wavefronts. We have confirmed this phenomenon by rigorous numerical evidence through the analysis of the eigenvalue distribution of S_{21} of our 3D random media model presented in Figure 3.3; similar observations for 2D were made in [55]. The existence of open channels in non-absorbing random media forms the basis for the development of schemes for constructing wavefronts that produce highly focused fields when exiting such media. Our in-depth understanding of the non-absorbing case notwithstanding, the characteristics of EM transmission through absorbing random media have not been well-studied. However, because scattering matrices of non-absorbing random media are a special type of random matrix, we believe that those of absorbing media also belong to a generic set that is well studied in random matrix theory (RMT) [36, 37]. Based on this reasoning, we conjecture that a homogeneous absorbing random medium can be characterized by a maximum transmission coefficient max with

<center>127</center>

Tracy-Widom fluctuations [89, 90]. If this characterization holds true, it will shed light on the study of advanced techniques for increasing wave penetration through absorbing random media.

In this chapter, we characterize the backscattering and transmission characteristics of 3D periodic absorbing random media composed of lossy conducting elements residing in a lossless host. The media considered are structurally similar to the non-absorbing random media studied earlier. Through extensive numerical simulation of wave scattering by such absorbing media and inspection of their scattering matrices, we construct the probability distribution of their transmission coefficients. We find this distribution to be distinct from that of non-absorbing media and characterized by a $\tau_{\max} < 1.0$. Furthermore, we investigate the fluctuations of $\tau_{\max}$ caused by the randomness, and observe that it conforms to a universal Tracy-Widom probability distribution, as opposed to the exponential distribution of $\tau_{\max}$ for non-absorbing media. The efficacy of a backscattering-minimizing method for transmission maximization for absorbing media is also verified.

7.2 Distribution of Transmission Coefficients of Absorbing Random Media

7.2.1 Model of Absorbing Random Media

A model for an absorbing random medium can be obtained straightforwardly by extending the non-absorbing random medium model elaborated in Chapter 2. The former model is constructed by embedding many perfect electrically conducting (PEC) scatterers in a homogeneous dielectric host, which is non-absorbing, i.e. both the scatterers and the host are lossless. By adding a non-zero sheet resistance ρ_s to the scatterers, the incident waves induce weaker surface currents than PEC scatterers, and consequently scatter less and absorb more energy, causing attenuation.

The computational recipe to obtain the scattering matrix of absorbing media is almost identical to that for non-absorbing media; the only difference occurs at the calculation of the impedance matrix for solving Maxwell's equations by MoM, which now should take the sheet resistance ρ_s into account.

7.2.2   Numerical Result

Similar to the non-absorbing case, to investigate the empirical distribution of the transmission coefficients of 3D absorbing random media, we undertake a simulation of $10,000$ random trials. The accumulated distribution of the transmission coefficients of the eigen-wavefronts is shown in Figure 7.1. Here, the sheet resistance of the scatterers is $\rho_s = 0.4\Omega/\text{sq}$. All slabs have periodicity $D_x = D_y = 11.22\lambda$, $l = 4.0\lambda$, $K_1 = 802$ and the number of layers is $N_c = 3660$. The distribution exhibits a unimodal shape instead of the bimodal shape for the non-absorbing case. The number of eigen-wavefronts decreases with the transmission coefficient, and finally vanish around $\tau_{\max} = 0.776$. The specific value of $\tau_{\max}$ is inversely related to the value of ρ_s. Taking a closer look at the $\tau_{\max}$ limit, we find that the histogram fits a square root limit when $\tau \to \tau_{\max}$; this trend will be further examined in the following section when we investigate fluctuations of $\tau_{\max}$.

7.3   Fluctuation of the Maximal Transmission Coefficient

For an absorbing random medium, the most important characteristic we care about is $\tau_{\max}$. Since a portion of the energy from the incident EM wave is inevitably absorbed by the medium, $\tau_{\max}$ cannot be unity. Clearly, $\tau_{\max}$ is principally determined by the dissipation rate per unit area and the thickness of the medium, i.e. the parameters ρ_s, l, D_x, D_y and N_c in our model. Here, we are interested in the statistics of $\tau_{\max}$.

Since the overall scattering system is represented by a scattering matrix S, $\tau_{\max}$ is the largest eigenvalue of $R = S_{21}^H \cdot S_{21}$, which is a Hermitian matrix. We conjecture that fluctu-
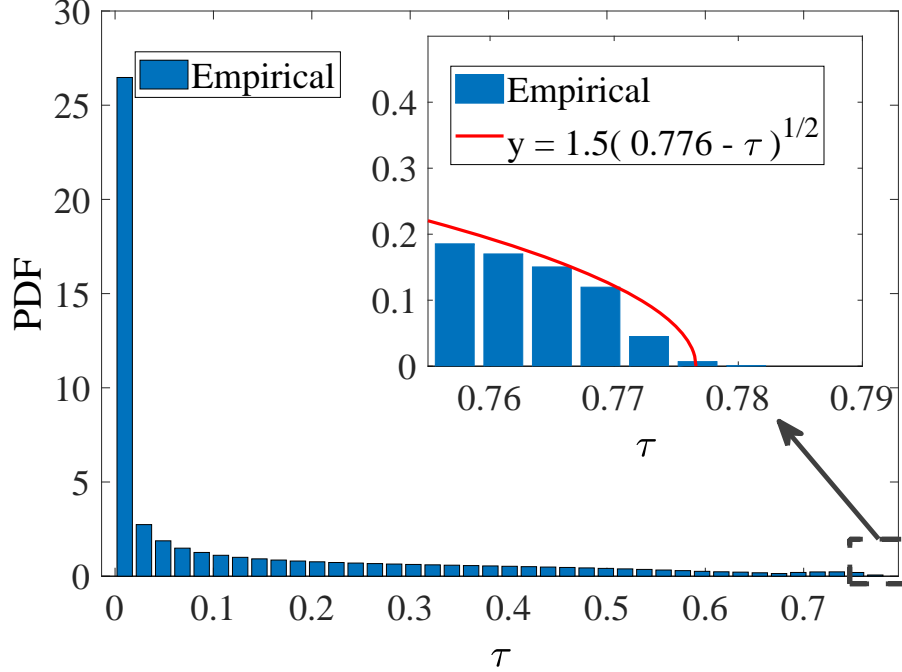
Figure 7.1: The accumulated distribution of the transmission coefficient over 10,000 random trials for absorbing random media model with $\rho_s = 0.4\Omega/\text{sq}$, $D_x = D_y = 11.22\lambda$, $l = 4.0\lambda$, $K_1 = 802$ and $N_c = 3660$.

ations in $\tau_{\max}$ adhere to the Tracy-Widom distribution, which is the probability distribution of the normalized largest eigenvalue of a random Hermitian matrix [89]. Specifically, if a Hermitian matrix Z is a Gaussian unitary ensemble (GUE), namely, $Z = (X + X^H)/2$ and X is a complex square matrix with independent identically distributed real and imaginary matrix elements that follow the normal distribution $\mathcal{N}(0, 1)$, then the probability function

$$F_{\text{TW}_2}(s) = \lim_{n \to \infty} \text{Prob}\Big((\lambda_{\max} - \sqrt{2n})(\sqrt{2})n^{1/6} \le s \Big), \tag{7.1}$$

is the cumulative distribution function (CDF) of the Tracy-Widom-2 probability distribution function (PDF) $f_{\text{TW}_2}(s)$. Here n is the dimension of the square matrix X and $\lambda_{\max}$ is the largest eigenvalue of Z. However, our Hermitian matrix $R = S_{21}^H \cdot S_{21}$ is not GUE, and its dimension is not very large. We therefore do not expect that the fluctuation of $\tau_{\max}$ is directly comparable to $f_{\text{TW}_2}(s)$; instead, we expect a shifted and scaled version of $\tau_{\max}$ to

satisfy the distribution. Particularly, we investigate the probability distribution of

$$s(\tau_{\max}) = \frac{\sigma_{\mathrm{TW}_2}}{\hat{\sigma}_{\tau\max}}(\tau_{\max} - \hat{\mu}_{\tau\max} + \mu_{\mathrm{TW}_2}), \tag{7.2}$$

in which μ_{TW_2} and σ_{TW_2} are the mean and standard deviation of the Tracy-Widom-2 distribution, respectively; their numerical values are $\mu_{\mathrm{TW}_2} = -1.771086807411$ and $\sigma_{\mathrm{TW}_2} = 0.901773138229843$; $\hat{\mu}_{\tau\max}$ and $\hat{\sigma}_{\tau\max}$ are the estimated mean and standard deviation of $\tau_{\max}$, respectively. We examine the behavior of $\tau_{\max}$ by obtaining S_{21} from $10,000$ random trails with parameters $\rho_s = 0.4\Omega/\mathrm{sq}$, $D_x = D_y =$ ranging from 3.86λ to 11.22λ (K_1 ranging from 98 to 802 correspondingly), $l = 4.0\lambda$ and N_c ranging from 480 to $3,660$ to keep the value of $\tau_{\max}$ steady around 0.8. The empirical distribution of $s(\tau_{\max})$ for $K_1 = 802$ shown in Figure 7.2a conforms to the Tracy-Widom-2 distribution very well. To further justify our conjecture, we investigate the distribution of $\tau_{\max}$ from S_{21} for different K_1 by properly changing the parameters D_x, D_y and N_c. For each K_1, $10,000$ trials are performed, and the corresponding distributions $s(\tau_{\max})$ are compared to the Tracy-Widom-2 distribution on a logarithmic scale shown in Figure 7.2b. All case exhibit good agreement. Furthermore, the skewness of each case for different K_1 is shown in Figure 7.2c; we see that as K_1 increases, the asymmetry of the empirical distribution is more outspoken, and the value of the skewness becomes closer to that of the Tracy-Widom-2 distribution.

In addition, we observe that the standard deviation of $\tau_{\max}$, denoted by $\sigma_{\max}$ scales as $O(K_1^{-2/3})$, which is shown in Figure 7.2d. The following relationship holds between $\sigma_{\tau\max}$, S_{21}'s dimension K_1 and the CDF $F(\tau)$ (PDF $f(\tau)$) of the transmission coefficients (the eigenvalues of $S_{21}^H \cdot S_{21}$):

$$F(\tau_{\max}) - F(\tau_{\max} - \sigma_{\tau\max}) = O\left(\frac{1}{K_1}\right). \tag{7.3}$$
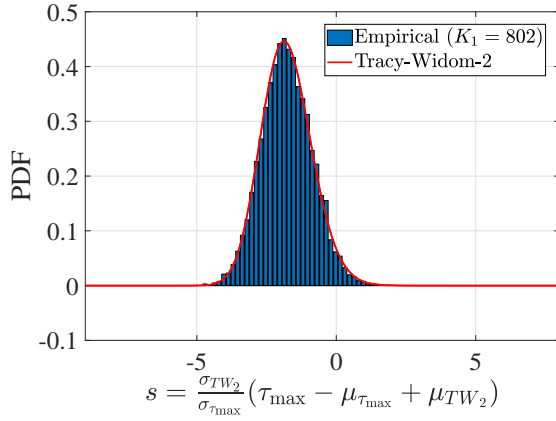
(a) The empirical distribution of $s(\tau_{\max})$ for $K_1 = 802$ and the Tracy-Widom-2 distribution.
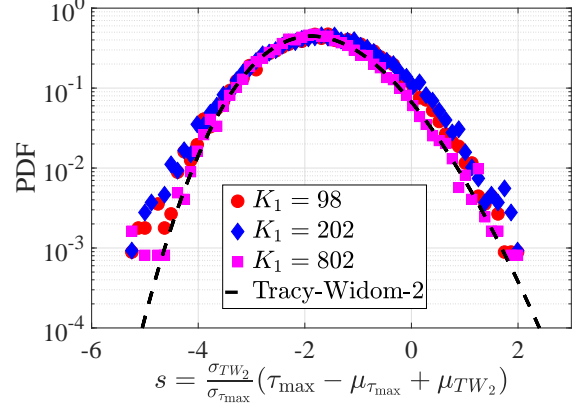
(b) The empirical distribution of $s(\tau_{\max})$ for different K_1 and the Tracy-Widom-2 distribution in logarithmic scale.
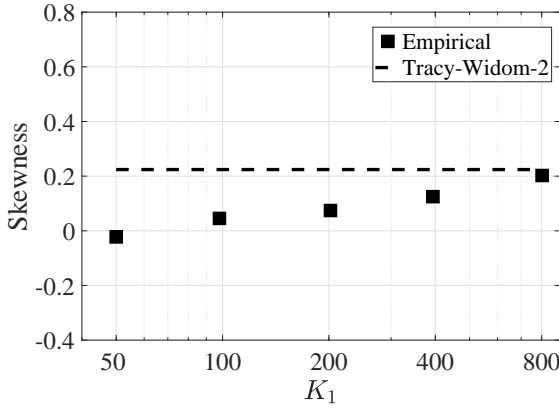
(c) The Skewness of the empirical distribution of $s(\tau_{\max})$ for different K_1.
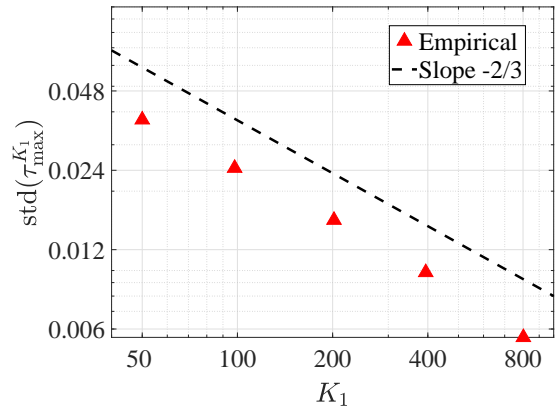
(d) The standard deviation of $\tau_{\max}$ for different K_1.

Figure 7.2: Statistical investigation on the fluctuation of $\tau_{\max}$ in *absorbing* random media. For each case of different S_{21} dimension K_1, the sheet resistance is fixed at $0.4\Omega/\text{sq}$, and all statistical estimations for each case are draw from $10,000$ trials.

This relationship can also be stated as

$$\sigma_{\tau_{\max}} \cdot f(\tau_{\max} - \sigma_{\tau_{\max}}) = O\left(\frac{1}{K_1}\right). \tag{7.4}$$

We therefore have

$$f\left(\tau_{\max} - O\left(K_1^{-2/3}\right)\right) = O\left(K_1^{-1/3}\right), \tag{7.5}$$

132

which implies

$$\lim_{\tau \to \tau_{\max-}} f(\tau) = O(\sqrt{\tau_{\max} - \tau}). \tag{7.6}$$

Eq. (7.6) suggests that the PDF of transmission coefficients of absorbing systems that describes the shape observed in Figure 7.1 may be of the form

$$f(\tau) = \frac{c\sqrt{\tau_{\max} - \tau}}{\tau}, \tag{7.7}$$

where c is an appropriate constant.

It is interesting to note that the empirical $\tau_{\max}$ of non-absorbing random media also exhibits fluctuations, despite the fact that the DMPK distribution guarantees $\tau_{\max} \equiv 1.0$. The reason is that the DMPK distribution assumes the number of eigen-modes (or propagating modes) K_1 approaches infinity; in reality K_1 is finite (though very large), resulting in $\delta = 1.0 - \tau_{\max}$ being not strictly zero. In our random media model, the finiteness of the number of eigen-modes is due to the enforced periodic condition.

We now investigate the fluctuation of $\tau_{\max}$ for non-absorbing random media. Specifically, we demonstrate that the random variable

$$s(\tau_{\max}) = \frac{1.0 - \tau_{\max}}{\hat{\sigma}_{\tau_{max}}}, \tag{7.8}$$

obeys the exponential distribution $f_{Exp(\lambda)}(s) = \lambda e^{-\lambda s}$ with $\lambda \equiv 1.0$. In Eq. (7.8), $\hat{\sigma}_{\tau_{\max}}$ is the estimated standard deviation of $\tau_{\max}$. This exponential distribution of $\tau_{\max}$ for non-absorbing media meets our expectation. Related numerical results are shown in Figure 7.3 in a manner similar to Figure 7.2. The corresponding parameters here are $D_x = D_y$ ranging from 3.78λ to 9.85λ (K_1 ranging from 96 to 690 correspondingly), $l = 4.0\lambda$ and N_c ranging from 480 to $4,150$. Figures 7.3(a-c) illustrate that the empirical distribution of $\tau_{\max}$ conforms to the exponential distribution $Exp(1.0)$. Furthermore, if the medium is
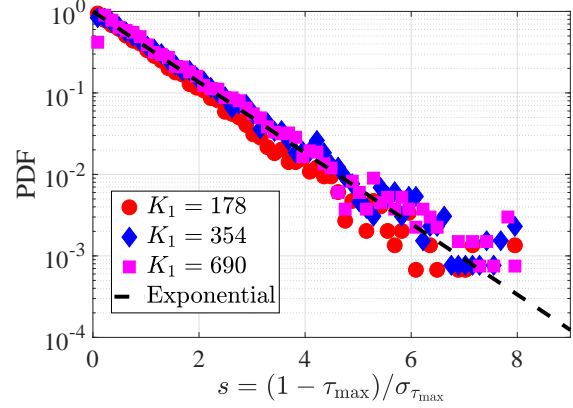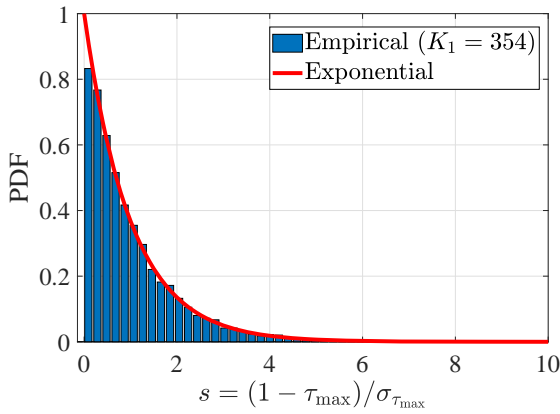
(a) The empirical distribution of $s(\tau_{\max})$ for $K_1 = 354$ and the exponential distribution.

(b) The empirical distribution of $s(\tau_{\max})$ for different K_1 and the exponential distribution in logarithmic scale.
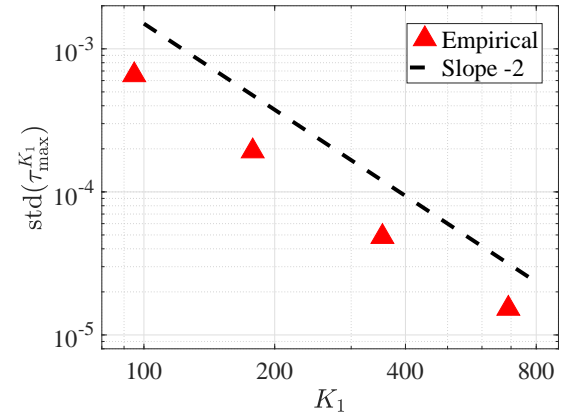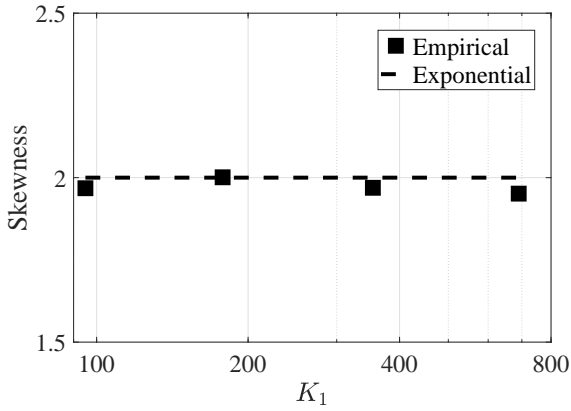
(c) The Skewness of the empirical distribution of $s(\tau_{\max})$ for different K_1.

(d) The standard deviation of $\tau_{\max}$ for different K_1.

Figure 7.3: Statistical investigation on the fluctuation of $\tau_{\max}$ in *non-absorbing* random media. All statistical estimations for each case are draw from 10,000 trials.

known to be non-absorbing, viz., the DMPK law is valid, we have

$$O\left(\frac{1}{K_1}\right) \propto \mathrm{Prob}(1 - \tau \leq \sigma_{\tau_{\max}}) = \int_{1-\sigma_{\tau_{\max}}}^{1} f_{\mathrm{DMPK}}(\tau)d\tau \approx \frac{\ell}{L}\sqrt{\sigma_{\tau_{\max}}}, \qquad (7.9)$$

which in essence means

$$\sigma_{\tau_{\max}} \propto O\left(\frac{1}{K_1^2}\right). \qquad (7.10)$$

Eq. (7.10) is perfectly justified by the numerical results shown in Figure 7.3d.

7.4 Transmission Maximization in Absorbing Random Media

Next, we study the efficacy of the transmission maximization methods of Section 3.4.2 applied to absorbing media. Those methods work by minimizing backscattering to maximize transmission, and are highly effective for non-absorbing media. However, for absorbing media, the amount of transmitted energy will not necessarily be enhanced by minimizing backscattered waves due to absorption. Here, we verify whether backscattering-minimizing transmission maximization methods continue to deliver for absorbing media. Particularly, we investigate the gain of the CG method as a function of the thickness of the
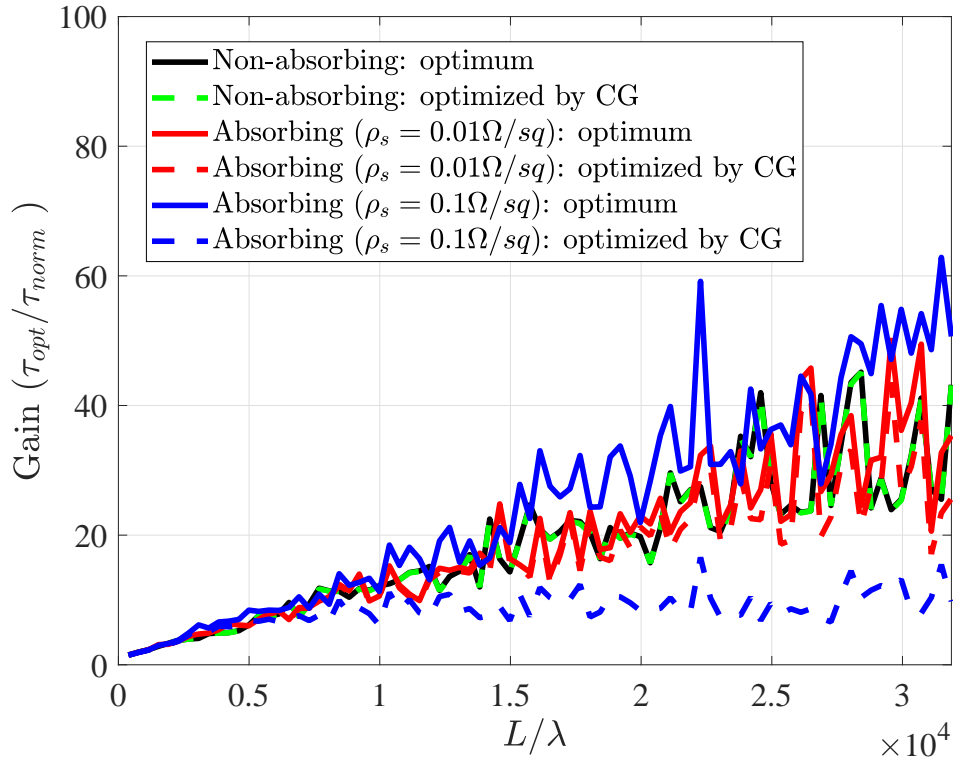
Figure 7.4: Comparing of the gain (=:$\tau_{\mathsf{opt}}/\tau_{\mathsf{norm}}$) between the one optimized by the backscatter-minimizing CG method and the optimum from the eigen-decomposition, as a function of the thickness L/λ for both absorbing and non-absorbing slabs. The sheet resistance $\rho(\Omega/\mathrm{sq})$ on the surface of the scatterers provide strong or weak absorption ($0.1\Omega/\mathrm{sq}$ vs. $0.01\Omega/\mathrm{sq}$).

slab under two scenarios —- weak absorption with $\rho_s = 0.01\Omega/\text{sq}$ and strong absorption with $\rho_s = 0.1\Omega/\text{sq}$; all other parameters of the media are the same for both cases. The gain is defined as the ratio of the transmission coefficient τ_{opt} optimized by the CG method (or the optimum/best one obtained from the eigen-decomposition of $S_{21}^H \cdot S_{21}$) over the transmission coefficient τ_{norm} for a normally incident plane wave. The results are shown in Figure 7.4. The efficacy of the CG method for absorbing media can be evaluated by examining the difference between the CG-optimized gain and the optimum eigen gain. From the figure we see that as the thickness of the slab increases, the overall absorption increases and therefore the difference of the gains obtained by the two methods increases; in contrast, such difference is negligible for non-absorbing media. However, for media with weak absorption ($\rho = 0.01\Omega/\text{sq}$), we note that the backscattering-minimizing CG method can still produce high gains close to the optimum.

7.5 Conclusion

By simulating absorbing random media modeled as multi-layered periodic structures loaded with metallic lossy particles, we find that the distribution of the transmission coefficients, namely the square of the singular values of the forward scattering matrix S_{21}, coincides with our predictions of a square-root decay and that the distribution vanishes around $\tau_{\text{max}} < 1.0$. Moreover, we confirm that S_{21} of absorbing media exhibits similarity to a random Hermitian matrix, and that the statistics of τ_{max} conform to a Tracy-Widom distribution as opposed to the exponential fluctuations observed in non-absorbing media. This distribution is universal regardless of the thickness, particle density, or absorbing characteristics of the medium. We also show that the backscattering-minimizing CG method is still effective for enhancing wave transmission through weakly absorbing random media.

CHAPTER 8

Conclusions

8.1 Summary

This thesis presents a model for characterizing light or EM wave propagation in 3D random media and develops several techniques to efficiently control the behavior of wavefronts passing through such media. First, a 3D MoM technique is used to model EM wave propagation in random media composed of multi-layer periodic slabs containing metallic particles ranging from dipoles to crosses and beyond. Even when the number of layers and particle density is high, our simulation shows the existence of so-called open channels, i.e. perfectly/highly transmitting wavefronts with transmission coefficients near unity, and demonstrates the validity of backscatter-analysis-based methods that use steepest descent, conjugate gradient and Lanczos-like algorithms for transmission maximization and focusing of the incident field.

Next, we present a family of methods that comprehensively tackle the wavefront shaping problem by leveraging eigen-decompositions, convex optimization, and bisection search algorithms. Specifically, eigen-decompositions are used to handle simple focusing problems when full phase-amplitude modulation is achievable while convex optimization and bisection search are invoked for focusing problems lacking closed form solutions. We furthermore apply these methods to 3D random media composed of multi-layer periodic slabs containing randomly positioned metallic particles that are thousands of wavelengths thick.

Since knowledge of the transmission matrix S_{21} of a random medium is a prerequisite for applying most of the proposed wavefront shaping schemes, we introduce three methods, namely alternating minimization, Phase-Lift and Phase-Cut, to retrieve the measurement matrix Q (which is closely related to S_{21}) through intensity-only field measurement. We also develop two more schemes, namely alternating minimization and proximal gradient, to retrieve S_{21} via backscattering analysis. The backscatter-analysis-based schemes extract information of S_{21} from the backscattered wavefront field using the notion of passive guide stars, viz., the presence of well-known scatterers behind the random medium.

While most of our algorithms target monochromatic applications, we also develop efficient focusing schemes for transient fields to accommodate applications requiring a pulsating illumination. By leveraging Fourier transform methods, the optimal wavefronts from a wide frequency range are added constructively at desired locations and pre-specified times, resulting in even tighter spatial foci than achievable using narrowband signals. Just like their frequency-domain counterparts, these time-domain wavefront shaping schemes schemes are capable of creating multiple foci under a variety of conditions of practical interest, and are compatible with both phase-amplitude and phase-only modulators. They also provide the option to create asynchronous or simultaneous foci.

Finally, the back scattering and transmitting properties of absorbing random media are investigated by examining the distribution of their transmission coefficients, viz., the squared singular values of their S_{21}. We find that fluctuations of the maximal transmission coefficients adhere to a universal Tracy-Widom probability distribution, regardless of the thickness, particle density, or absorbing characteristics of the media. We also find that for weakly absorbing media, the backscattering-minimizing CG method is still effective for enhancing wave transmission.

8.2 Further Work

First, although we have shown that our 3D random media model can fully capture the characteristics of EM and light interaction with random media despite the introduction of artificial periodic conditions, the impact of these periodic assumptions on statistics of the field not considered here definitely is worthy of further study. Moreover, for a given medium, the number of open channels, which could be affected by the thickness of the medium, determines the level of controllability of the transmitted wavefronts for focusing and other applications; therefore, a study aimed at quantifying the controllability of the transmitted wavefronts as a function of the thickness of the medium under consideration is called for. Last but not least, the development of efficient wavefront shaping techniques suitable for moderately or even strongly absorbing random media is called for.

8.3 Contributions

The following journal papers and conference papers/abstracts related to the work presented in this thesis are either published, submitted or currently being prepared.

8.3.1 Journal Papers

1. H. Guo, R. R. Nadakuditi and E. Michielssen, "Numerical Analysis and Efficient Reconstruction of Perfectly Transmitting Wavefronts in 3D Random Media with Periodic Condition", ready for submission.

2. H. Guo, R. R. Nadakuditi and E. Michielssen, "Tracy-Widom Distribution of Transmission Coefficients of 3D Absorbing Random Media", ready for submission.

3. H. Guo, E. Michielssen and R. R. Nadakuditi, "Advanced Multi-Foci Focusing Schemes in 3D Random Media", in preparation.

4. H. Guo, E. Michielssen and R. R. Nadakuditi, "Efficient Guide-star Enabled Reconstruction of Scattering Matrix of 3D Random Media", in preparation.

8.3.2 Conference Papers

1. H. Guo, R. R. Nadakuditi and E. Michielssen, "Numerical Analysis and Efficient Reconstruction of Perfectly Transmitting Wavefronts in 3D Periodic Media", USNC-URSI National Radio Science Meeting 2016, Fajardo, Puerto Rico.

2. H. Guo, R. R. Nadakuditi and E. Michielssen, "Tracy-Widom Distribution of Transmission Coefficients of 3-D Absorbing Random Media", USNC-URSI National Radio Science Meeting 2016, Fajardo, Puerto Rico.

3. H. Guo, E. Michielssen and R. R. Nadakuditi, "Efficient Guide-star Enabled Reconstruction of Scattering Matrices via Alternating Minimization and Proximal Gradient Methods", USNC-URSI National Radio Science Meeting 2017, San Diego, California, USA.

4. H. Guo, E. Michielssen and R. R. Nadakuditi, "Efficient Guide-star Enabled Reconstruction of Scattering Matrices via Alternating Minimization and Proximal Gradient Methods", USNC-URSI National Radio Science Meeting 2017, San Diego, California, USA.

5. H. Guo, E. Michielssen and R. R. Nadakuditi, "Accelerating the Transmission Matrix Retrieval via Low-Rank Compression and Fast Proximal Gradient Methods", USNC-URSI National Radio Science Meeting 2018, Boston, Massachusetts, USA.

6. H. Guo, E. Michielssen and R. R. Nadakuditi, "Efficient Focusing on Transient Field through Highly Diffusive Random Media", USNC-URSI National Radio Science Meeting 2018, Boston, Massachusetts, USA.

APPENDIX A

Methods

A.1   Solving Eq. (4.16) in MATLAB

Specifically, the solution to Eq. (4.16) can be computed in MATLAB using the CVX package [75] by invoking the following sequence of commands:

```
cvx_begin sdp

    variable A(K1,K1) hermitian semidefinite

    maximize trace(Q'*Q*A)

    subject to

    diag(A) == ones(K1,1)/K1;

cvx_end

Asdp = A; % return optimum in variable Asdp
```

For settings where $K1 > 100$, we recommend using the SDPT3 solver [76]. The solution to Eq. (4.16) can be computed in MATLAB using the SDPT3 package by invoking the following sequence of commands:

```
cost_function = Q'*Q;

e = ones(K1,1);

b = e/K1;

num_params = K1*(K1-1)/2;
```

```matlab
C{1} = cost_function;

A = cell(1,K1);

for j = 1:K1

    A{j} = sparse(j,j,1,K1,K1);

end

blk{1,1} = 's';

blk{1,2} = K1;

Avec = svec(blk(1,:),A,1);

[obj,X,y,Z] = sqlp(blk,Avec,C,b);

Asdp = cell2mat(X);   % return optimum in variable Asdp
```

BIBLIOGRAPHY

[1] T. Chaigne, O. Katz, A. C. Boccara, M. Fink, E. Bossy, and S. Gigan, "Controlling light in scattering media non-invasively using the photoacoustic transmission matrix," *Nature Photonics*, vol. 8, no. 1, pp. 58–64, 2014.

[2] R. Horstmeyer, H. Ruan, and C. Yang, "Guidestar-assisted wavefront-shaping methods for focusing light into biological tissue," *Nature photonics*, vol. 9, p. 563, 2015.

[3] L. Battan, *Radar Observation of the Atmosphere*. University of Chicago Press, 1973.

[4] I. Tolstoy and C. S. Clay, *Ocean acoustics*. McGraw-Hill New York, 1966, vol. 293.

[5] B. J. Berne and R. Pecora, *Dynamic light scattering: with applications to chemistry, biology, and physics*. Courier Corporation, 2000.

[6] B. Crosignani, *Statistical properties of scattered light*. Elsevier, 1975.

[7] A. Ishimaru, *Wave propagation and scattering in random media*. Academic press New York, 1978, vol. 2.

[8] ——, "Theory and application of wave propagation and scattering in random media," *Proceedings of the IEEE*, vol. 65, no. 7, pp. 1030–1061, 1977.

[9] J. Ryde, "The scattering of light by turbid media. part i," *Proceedings of the Royal Society of London. Series A, Containing Papers of a Mathematical and Physical Character*, vol. 131, no. 817, pp. 451–464, 1931.

[10] J. Ryde and B. Cooper, "The scattering of light by turbid media. part ii," *Proceedings of the Royal Society of London. Series A, Containing Papers of a Mathematical and Physical Character*, vol. 131, no. 817, pp. 464–475, 1931.

[11] L. L. Foldy, "The multiple scattering of waves. i. general theory of isotropic scattering by randomly distributed scatterers," *Physical Review*, vol. 67, no. 3-4, p. 107, 1945.

[12] M. Lax, "Multiple scattering of waves," *Reviews of Modern Physics*, vol. 23, no. 4, p. 287, 1951.

[13] ——, "Multiple scattering of waves. ii. the effective field in dense systems," *Physical Review*, vol. 85, no. 4, p. 621, 1952.

[14] H. S. Snyder and W. T. Scott, "Multiple scattering of fast charged particles," *Physical Review*, vol. 76, no. 2, p. 220, 1949.

[15] V. Twersky, "On propagation in random media of discrete scatterers," in *Proc. Am. Math. Soc*, vol. 16, 1964, pp. 84–116.

[16] ——, "Absorption and multiple scattering by biological suspensions," *JOSA*, vol. 60, no. 8, pp. 1084–1093, 1970.

[17] ——, "Interface effects in multiple scattering by large, low-refracting, absorbing particles," *JOSA*, vol. 60, no. 7, pp. 908–914, 1970.

[18] P. C. Waterman and R. Truell, "Multiple scattering of waves," *Journal of Mathematical Physics*, vol. 2, no. 4, pp. 512–537, 1961.

[19] A. Ishimaru, "Correlation functions of a wave in a random distribution of stationary and moving scatterers," *Radio Science*, vol. 10, no. 1, pp. 45–52, 1975.

[20] C. Beard, T. Kays, and V. Twersky, "Scattering by random distribution of spheres vs. concentration," *IEEE Transactions on Antennas and Propagation*, vol. 15, no. 1, pp. 99–118, 1967.

[21] U. Frisch, "Wave propagation in random media." Centre National de la Recherche Scientifique, Paris, Tech. Rep., 1970.

[22] N. Marcuvitz, "On the theory of plasma turbulence," *Journal of Mathematical Physics*, vol. 15, no. 6, pp. 870–879, 1974.

[23] V. I. Tatarskii, "The effects of the turbulent atmosphere on wave propagation," *Jerusalem: Israel Program for Scientific Translations, 1971*, 1971.

[24] M. Born, "Quantenmechanik der stoßvorgänge," *Zeitschrift für Physik A Hadrons and Nuclei*, vol. 38, no. 11, pp. 803–827, 1926.

[25] S. Chandrasekhar, *Radiative transfer*. Courier Corporation, 2013.

[26] V. V. Sobolev, "A treatise on radiative transfer." *Princeton, NJ, Van Nostrand [1963]*, vol. 1, 1963.

[27] R. W. Preisendorfer, *Radiative transfer on discrete spaces*. Elsevier, 2014, vol. 74.

[28] A. Schuster, "Radiation through a foggy atmosphere," *The astrophysical journal*, vol. 21, p. 1, 1905.

[29] L. Tsang and J. Kong, "Radiative transfer theory for active remote sensing of half-space random media," *Radio Science*, vol. 13, no. 5, pp. 763–773, 1978.

[30] L. Tsang, J. Kong, and R. Shin, "Radiative transfer theory for active remote sensing of a layer of nonspherical particles," *Radio Science*, vol. 19, no. 02, pp. 629–642, 1984.

[31] F. T. Ulaby, R. K. Moore, and A. K. Fung, *Microwave remote sensing active and passive*. LONDON, ADDISON-WESLEY PUBLISHING COMPANY. FIGS., 2015.

[32] M. Karam and A. Fung, "Electromagnetic scattering from a layer of finite length, randomly oriented, dielectric, circular cylinders over a rough interface with application to vegetation," *International Journal of Remote Sensing*, vol. 9, no. 6, pp. 1109–1134, 1988.

[33] C. W. Beenakker, "Random-matrix theory of quantum transport," *Reviews of modern physics*, vol. 69, no. 3, p. 731, 1997.

[34] T. Strudley, T. Zehender, C. Blejean, E. P. Bakkers, and O. L. Muskens, "Mesoscopic light transport by very strong collective multiple scattering in nanowire mats," *Nature Photonics*, vol. 7, no. 5, pp. 413–418, 2013.

[35] A. P. Mosk, A. Lagendijk, G. Lerosey, and M. Fink, "Controlling waves in space and time for imaging and focusing in complex media," *Nature photonics*, vol. 6, no. 5, pp. 283–292, 2012.

[36] V. A. Marčenko and L. A. Pastur, "Distribution of eigenvalues for some sets of random matrices," *Mathematics of the USSR-Sbornik*, vol. 1, no. 4, p. 457, 1967.

[37] A. Edelman and N. R. Rao, "Random matrix theory," *Acta Numerica*, vol. 14, pp. 233–297, 2005.

[38] O. Dorokhov, "Transmission coefficient and the localization length of an electron in n bound disordered chains," *JETP Lett*, vol. 36, no. 7, pp. 318–321, 1982.

[39] J. Pendry, A. MacKinnon, and A. Pretre, "Maximal fluctuationsa new phenomenon in disordered systems," *Physica A: Statistical Mechanics and its Applications*, vol. 168, no. 1, pp. 400–407, 1990.

[40] C. Barnes and J. Pendry, "Multiple scattering of waves in random media: a transfer matrix approach," in *Proceedings of the Royal Society of London A: Mathematical, Physical and Engineering Sciences*, vol. 435, no. 1893. The Royal Society, 1991, pp. 185–196.

[41] P. Mello, P. Pereyra, and N. Kumar, "Macroscopic approach to multichannel disordered conductors," *Annals of Physics*, vol. 181, no. 2, pp. 290–317, 1988.

[42] I. Vellekoop and A. Mosk, "Universal optimal transmission of light through disordered materials," *Physical review letters*, vol. 101, no. 12, p. 120601, 2008.

[43] ——, "Phase control algorithms for focusing light through turbid media," *Optics communications*, vol. 281, no. 11, pp. 3071–3080, 2008.

[44] S. Popoff, G. Lerosey, R. Carminati, M. Fink, A. Boccara, and S. Gigan, "Measuring the transmission matrix in optics: an approach to the study and control of light propagation in disordered media," *Physical review letters*, vol. 104, no. 10, p. 100601, 2010.

[45] T. W. Kohlgraf-Owens and A. Dogariu, "Transmission matrices of random media: means for spectral polarimetric measurements," *Optics letters*, vol. 35, no. 13, pp. 2236–2238, 2010.

[46] Z. Shi, J. Wang, and A. Z. Genack, "Measuring transmission eigenchannels of wave propagation through random media," in *Frontiers in Optics*. Optical Society of America, 2010, p. FWT4.

[47] M. Kim, Y. Choi, C. Yoon, W. Choi, J. Kim, Q.-H. Park, and W. Choi, "Maximal energy transport through disordered media with the implementation of transmission eigenchannels," *Nature photonics*, vol. 6, no. 9, pp. 581–585, 2012.

[48] E. G. van Putten, A. Lagendijk, and A. Mosk, "Optimal concentration of light in turbid materials," *JOSA B*, vol. 28, no. 5, pp. 1200–1203, 2011.

[49] J. Aulbach, B. Gjonaj, P. M. Johnson, A. P. Mosk, and A. Lagendijk, "Control of light transmission through opaque scattering media in space and time," *Physical review letters*, vol. 106, no. 10, p. 103901, 2011.

[50] M. Cui, "A high speed wavefront determination method based on spatial frequency modulations for focusing light through random scattering media," *Optics express*, vol. 19, no. 4, pp. 2989–2995, 2011.

[51] ——, "Parallel wavefront optimization method for focusing light through random scattering media," *Optics letters*, vol. 36, no. 6, pp. 870–872, 2011.

[52] C. Stockbridge, Y. Lu, J. Moore, S. Hoffman, R. Paxman, K. Toussaint, and T. Bifano, "Focusing through dynamic scattering media," *Optics express*, vol. 20, no. 14, pp. 15 086–15 092, 2012.

[53] W. Choi, A. P. Mosk, Q.-H. Park, and W. Choi, "Transmission eigenchannels in a disordered medium," *Physical Review B*, vol. 83, no. 13, p. 134207, 2011.

[54] C. Jin, "New methods and theory for increasing transmission of light through highly-scattering random media," Ph.D. dissertation, The University of Michigan, 2014.

[55] C. Jin, R. R. Nadakuditi, E. Michielssen, and S. C. Rand, "Iterative, backscatter-analysis algorithms for increasing transmission and focusing light through highly scattering random media," *JOSA A*, vol. 30, no. 8, pp. 1592–1602, 2013.

[56] G. Lazarev, A. Hermerschmidt, S. Krüger, and S. Osten, "Lcos spatial light modulators: trends and applications," *Optical Imaging and Metrology: Advanced Technologies*, pp. 1–29, 2012.

[57] D. B. Conkey, A. M. Caravaca-Aguirre, and R. Piestun, "High-speed scattering medium characterization with application to focusing light through turbid media," *Optics express*, vol. 20, no. 2, pp. 1733–1740, 2012.

[58] E. Van Putten, I. Vellekoop, and A. Mosk, "Spatial amplitude and phase modulation using commercial twisted nematic lcds," *Applied optics*, vol. 47, no. 12, pp. 2076–2081, 2008.

[59] J. Park, H. Yu, J.-H. Park, and Y. Park, "Lcd panel characterization by measuring full jones matrix of individual pixels using polarization-sensitive digital holographic microscopy," *Optics express*, vol. 22, no. 20, pp. 24 304–24 311, 2014.

[60] C. Jin, R. R. Nadakuditi, and E. Michielssen, "The transmission coefficient distribution of highly scattering sparse random media," *arXiv preprint arXiv:1503.03432*, 2015.

[61] C. Jin, R. R. Nadakuditi, E. Michielssen, and S. C. Rand, "Backscatter analysis based algorithms for increasing transmission through highly scattering random media using phase-only-modulated wavefronts," *JOSA A*, vol. 31, no. 8, pp. 1788–1800, 2014.

[62] C. Jin, R. R. Nadakuditi, E. Michielssen, and S. Rand, "An iterative, backscatter-analysis based algorithm for increasing transmission through a highly-backscattering random medium," in *Statistical Signal Processing Workshop (SSP), 2012 IEEE*. IEEE, 2012, pp. 97–100.

[63] C. Beenakker, "Applications of random matrix theory to condensed matter and optical physics," *arXiv preprint arXiv:0904.1432*, 2009.

[64] B. Stout, "Spherical harmonic lattice sums for gratings," 2012.

[65] S. Rao, D. Wilton, and A. Glisson, "Electromagnetic scattering by surfaces of arbitrary shape," *IEEE Trans. Antennas Propag.*, vol. 30, no. 3, pp. 409–418, 1982.

[66] R. J. Schmidt, "Xxxii. on the numerical solution of linear simultaneous equations by an iterative method," *The London, Edinburgh, and Dublin Philosophical Magazine and Journal of Science*, vol. 32, no. 214, pp. 369–383, 1941.

[67] D. Shanks, "Non-linear transformations of divergent and slowly convergent sequences," *Studies in Applied Mathematics*, vol. 34, no. 1-4, pp. 1–42, 1955.

[68] S. Singh, W. F. Richards, J. R. Zinecker, and D. R. Wilton, "Accelerating the convergence of series representing the free space periodic green's function," *IEEE Transactions on Antennas and Propagation*, vol. 38, no. 12, pp. 1958–1962, 1990.

[69] G. H. Golub and C. F. Van Loan, *Matrix computations*. JHU Press, 2012, vol. 3.

[70] S. Grilli, P. Ferraro, S. De Nicola, A. Finizio, G. Pierattini, and R. Meucci, "Whole optical wavefields reconstruction by digital holography," *Optics Express*, vol. 9, no. 6, pp. 294–302, 2001.

[71] M. Fink *et al.*, "Time-reversed acoustics," *Scientific American*, vol. 281, no. 5, pp. 91–97, 1999.

[72] S. Boyd and L. Vandenberghe, *Convex optimization*. Cambridge university press, 2004.

[73] Z.-Q. Luo, W.-K. Ma, A. M.-C. So, Y. Ye, and S. Zhang, "Semidefinite relaxation of quadratic optimization problems," *IEEE Signal Processing Magazine*, vol. 27, no. 3, pp. 20–34, 2010.

[74] L. Vandenberghe and S. Boyd, "Semidefinite programming," *SIAM review*, vol. 38, no. 1, pp. 49–95, 1996.

[75] M. Grant, S. Boyd, and Y. Ye, "Cvx: Matlab software for disciplined convex programming," 2008.

[76] K.-C. Toh, M. J. Todd, and R. H. Tütüncü, "Sdpt3a matlab software package for semidefinite programming, version 1.3," *Optimization methods and software*, vol. 11, no. 1-4, pp. 545–581, 1999.

[77] S. Schaible and T. Ibaraki, "Fractional programming," *European Journal of Operational Research*, vol. 12, no. 4, pp. 325–338, 1983.

[78] L. N. Trefethen and D. Bau III, *Numerical linear algebra*. Siam, 1997, vol. 50.

[79] M. L. Overton and R. S. Womersley, "On the sum of the largest eigenvalues of a symmetric matrix," *SIAM Journal on Matrix Analysis and Applications*, vol. 13, no. 1, pp. 41–45, 1992.

[80] R. W. Gerchberg, "A practical algorithm for the determination of the phase from image and diffraction plane pictures," *Optik*, vol. 35, pp. 237–246, 1972.

[81] J. R. Fienup, "Phase retrieval algorithms: a comparison," *Applied optics*, vol. 21, no. 15, pp. 2758–2769, 1982.

[82] P. Netrapalli, P. Jain, and S. Sanghavi, "Phase retrieval using alternating minimization," in *Advances in Neural Information Processing Systems*, 2013, pp. 2796–2804.

[83] Y. Wang, J. Yang, W. Yin, and Y. Zhang, "A new alternating minimization algorithm for total variation image reconstruction," *SIAM Journal on Imaging Sciences*, vol. 1, no. 3, pp. 248–272, 2008.

[84] S. W. Peters and R. W. Heath, "Interference alignment via alternating minimization," in *Acoustics, Speech and Signal Processing, 2009. ICASSP 2009. IEEE International Conference on*. IEEE, 2009, pp. 2445–2448.

[85] P. Jain, P. Netrapalli, and S. Sanghavi, "Low-rank matrix completion using alternating minimization," in *Proceedings of the forty-fifth annual ACM symposium on Theory of computing*. ACM, 2013, pp. 665–674.

[86] B. Recht, M. Fazel, and P. A. Parrilo, "Guaranteed minimum-rank solutions of linear matrix equations via nuclear norm minimization," *SIAM review*, vol. 52, no. 3, pp. 471–501, 2010.

[87] N. Parikh, S. Boyd *et al.*, "Proximal algorithms," *Foundations and Trends® in Optimization*, vol. 1, no. 3, pp. 127–239, 2014.

[88] J.-F. Cai, E. J. Candès, and Z. Shen, "A singular value thresholding algorithm for matrix completion," *SIAM Journal on Optimization*, vol. 20, no. 4, pp. 1956–1982, 2010.

[89] C. A. Tracy and H. Widom, "Level-spacing distributions and the airy kernel," *Communications in Mathematical Physics*, vol. 159, no. 1, pp. 151–174, 1994.

[90] ——, "Distribution functions for largest eigenvalues and their applications," *arXiv preprint math-ph/0210034*, 2002.